

THE FLORIDA STATE UNIVERSITY  
COLLEGE OF ARTS AND SCIENCES

A STUDY OF ANGULAR DEPENDENCE IN PARTON-PARTON  
SCATTERING FROM MASSIVE HADRON PAIR PRODUCTION

By

HERMAN BRENNER WHITE, JR.

A Dissertation submitted to the  
Department of Physics  
in partial fulfillment of the  
requirements for the degree of  
Doctor of Philosophy

Degree Awarded:

Summer Semester, 1991

With deepest gratitude to my parents,  
Herman B. and Susie M. White

and to my sister,  
Zepherine W. Finch

This research was supported in part by funds from the U. S. Department of Energy, under grant number DEFG05-87ER-40319. Permission is granted to copy this dissertation.

## ACKNOWLEDGEMENTS

High energy physics experiments require the collective and cooperative efforts of many people. A complete list of all the persons involved would be prohibitive in this document, so I express my gratitude to all those who contributed to the completion of the experiment, particularly the collaborators: Gianluigi Boca, Mary Ann Cummings, Michael Crisler, Christos Georgiopoulos, J. Harvey Goldman, H. Richard Gustafson, Sharon Hagopian, Vasken Hagopian, Kurtis F. Johnson, David Levinthal, Fred Lopez, Stephen Pordes, H. L. Sawyer, Jonathan Streets, Kathleen Streets, and Jim Volk.

I wish to sincerely thank Vasken Hagopian for his assiduous support during my work here at FSU, as well as serving as the major professor for this dissertation. I extend my gratitude to Sanford A. Safron, Kirby W. Kemper, David A. Levinthal, and Joseph F. Owens, III for serving on my committee. In addition I thank Christos Georgiopoulos, and Jonathan Streets, for many helpful discussions about the data reduction and analysis.

While in residence here I am appreciative for having had the opportunity to explore many new ideas through physics discussions and engaging dialogue with the FSU faculty, especially with Horst D. Wahl, Joseph F. Owens, David Levinthal, Vasken Hagopian, and John Albright.

I express my whole-hearted gratitude to Joseph E. Lannutti, The Supercomputer Computations Research Institute and its staff for the use of the SCRI facilities and help in the completion of this work. My gratitude is also unbounded for the staff of the FSU high energy physics group.

I wish to thank Saul Ploplys, who spent a portion of his summer from high school teaching with our Fermilab group, for his technical support and enthusiasm. I especially thank Maurizio Bertoldi of FSU for his technical help with the experiment and his expert assistance in the production of a number of figures in this document.

I am grateful to the Directorate of the Fermi National Accelerator Laboratory for the initial leave of absence from my duties at the laboratory to complete this work, and to the staff of Fermilab for their support.

Finally I thank my parents for emphasizing education, and I am grateful to all of my family and so many unnamed friends for their unwavering support .

Tallahassee

July, 1991

H. B. White, Jr.

## TABLE OF CONTENTS

<b>LIST OF TABLES .....</b>	<b>x</b>
<b>LIST OF FIGURES.....</b>	<b>xii</b>
<b>ABSTRACT .....</b>	<b>xvii</b>
 <b>CHAPTER</b>	
<b>1 INTRODUCTION .....</b>	<b>1</b>
§1.1 Elementary Particle Scattering.....	1
§1.2 The Experiment E-711 .....	4
§1.3 Guide To This Dissertation .....	6
<b>2 THEORETICAL &amp; EXPERIMENTAL PHYSICS OVERVIEW .....</b>	<b>8</b>
§2.1 Historical Perspective.....	8
§2.2 Quantum Chromodynamics and Partons .....	13
§2.3 Large Transverse Momentum Hadronic Interactions.....	22
§2.4 Hadronic Pair Production and Jets .....	24
§2.5 Experimental Physics Overview .....	31
<b>3 THE PROTON BEAM SYSTEM.....</b>	<b>39</b>
§3.1 The Accelerator System.....	39
§3.2 The Neutrino East Beamline .....	44
§3.3 The Beam Monitoring System .....	51
§3.3.1 Proton Beam Intensity .....	51
§3.3.2 Proton Beam Control.....	53

<b>4</b>	<b>THE EXPERIMENTAL APPARATUS.....</b>	<b>59</b>
§4.1	Introduction.....	59
§4.2	The Targeting System .....	62
§4.2.1	Luminosity Monitors .....	64
§4.3	The Spectrometer Magnets .....	67
§4.3.1	Magnet Sizes.....	67
§4.3.2	Field Uniformity and Momentum Kick .....	68
§4.4	The Multiwire Drift Chambers.....	70
§4.4.1	Dimensions and Alignment.....	71
§4.4.2	Cell Layout and Wire Specifications.....	72
§4.4.3	The Central Beam Region.....	76
§4.4.4	The Gas Mixture .....	76
§4.4.5	Drift Chamber Operating Conditions .....	77
§4.5	The Hodoscopes and Calorimeters .....	79
§4.5.1	The Hodoscopes.....	80
§4.5.2	The Calorimeters .....	82
§4.5.3	The Calorimeter Operating Conditions .....	88
§4.5.4	The Calorimeter Calibration.....	89
<b>5</b>	<b>TRIGGER AND DATA ACQUISITION.....</b>	<b>98</b>
§5.1	General Considerations.....	98
§5.2	The Event Trigger.....	99
§5.2.1	Charge and $p_T$ Signal.....	102
§5.2.2	Mass Trigger .....	103
§5.2.3	Particle Pair Triggers .....	105
§5.3	Data Acquisition.....	107
§5.3.1	Experiment Monitoring.....	107
§5.3.2	Data Readout Interrupts .....	108
§5.3.3	Data Storage .....	112
<b>6</b>	<b>DATA PROCESSING .....</b>	<b>114</b>
§6.1	Track Recognition and Reconstruction.....	114
§6.2	Track Momentum Calculation.....	118
§6.3	Data Summary File Event Selection .....	121

<b>7 THE DATA ANALYSIS.....</b>	<b>123</b>
§7.1 Introduction.....	123
§7.2 The Measured Variables .....	123
§7.3 The Integrated Luminosity .....	125
§7.4 Background Study.....	128
§7.5 Event Selection Criteria .....	128
§7.6 The Acceptance .....	140
§7.7 Differential Cross Section .....	143
<b>8 PHYSICS RESULTS AND DISCUSSION.....</b>	<b>144</b>
§8.1 Introduction.....	144
§8.2 The Angular Distributions.....	144
§8.2 The Atomic Weight Dependence .....	160
§8.3 The Charge State Dependence and QCD .....	166
<b>9 CONCLUSIONS.....</b>	<b>179</b>
<b>A DI-HADRON SCATTERING FORMALISM.....</b>	<b>182</b>
§A.1 The Di-Hadron Process.....	182
§A.2 The Angular Distribution .....	185
<b>B BEAM AND TARGET DIMENSIONS.....</b>	<b>190</b>
§B.1 The Horizontal Beam Focus.....	190
§B.2 The Vertical Beam Range .....	191
<b>C SELECTED DETECTOR ELECTRONIC CIRCUITS.....</b>	<b>195</b>
<b>REFERENCES .....</b>	<b>199</b>
<b>Vita.....</b>	<b>203</b>



## LIST OF TABLES

### TABLE

2.1	The Standard Model.....	11
2.2	First Order QCD Cross Sections .....	16
4.1	Technical Information on the Experimental Targets .....	64
4.2	Drift Chamber Active Region and Distance From Target.....	71
4.3	Drift Chamber Wire Spacings.....	75
4.4	Chamber Operating Voltages.....	78
4.5	Chamber Plane Efficiencies.....	79
4.6	HF and HB Hodoscope Dimensions.....	81
4.7	Calorimeter Module Dimensions.....	87
4.8	Muon Energy Deposition in the Calorimeter .....	90
4.9	Calorimeter Calibration Results.....	97
5.1	Calorimeter and Hodoscope Segmentation.....	101
5.2	Trigger Efficiencies .....	106
5.3	A - interrupt Event Record Information .....	110
5.4	B - interrupt Spill Record Information .....	111
6.1	Two Track Reconstruction Efficiencies.....	117
6.2	Event Selection percentages for the Data Summary Tapes .....	117
6.3	Momentum Resolution Error per Target.....	121

6.4	Event Selection summary for the Data Summary Files.....	122
7.1	Total Integrated Luminosity .....	127
8.1	Beryllium Target Angular Distributions .....	146
8.2	Aluminum Target Angular Distributions .....	147
8.3	Iron Target Angular Distributions .....	148
8.4	Tungsten Target Angular Distributions.....	149
8.5	Integrated Target Data Angular Distributions.....	154
8.6	Summary of the Functional Fits.....	158
8.7	Atomic Weight Dependence .....	163
8.8	Dijet Distribution Comparisons.....	169
8.9	Charge Dependence Chart.....	172
8.10	Subprocess Charge Ratios .....	174

## LIST OF FIGURES

### FIGURES

2.1	Feynman Diagrams for a variety of scattering processes.....	17
2.2	Illustrative diagrams of (a) Lepton- Nucleon Scattering and (b) Electron-Positron annihilation and hadron production.....	20
2.3	The hard scattering process in the parton model.....	21
2.4	Illustrative diagrams of (a) Transverse Momentum with respect to the Beam Axis , $\mathbf{Z}$ (b) P-N Scattering, Lab Frame. $\mathbf{Pa}$ , $\mathbf{Pb}$ are partons, $\theta_3$ , $\theta_4$ are outgoing scattering angles, and (c) Parton-Parton Center of Mass Scattering Frame.....	26
2.5	Angular distributions in $\bar{p}p$ collisions for the UA -1 and the UA -2 Experiments with a QCD prediction to the data .....	34
2.6	Angular distributions for $\pi^0 \pi^0$ production from the CCOR Experiment with QCD predictions to the data.....	37
2.7	Dijet angular distributions in $\bar{p}p$ collisions for the CDF Detector Experiment with QCD predictions to the data .....	38
3.1	Layout of the Fermilab Accelerator Areas and the Fixed Target Beamlines .....	40
3.2	Representative Acceleration and Extraction Cycles of the Fermilab Accelerator.....	42
3.3	Layout of the NE Beam line.....	46
3.4	Beam Envelope for the NE Beam Design Monte Carlo Results.....	50
3.5	Calibration of the NECIC ionization chamber with respect to scintillation counters at low beam intensity.....	52

3.6	Calibration of the NECH dipole magnet with respect to the 1mm wire spacing of the NEEWC wire chamber , 6.29 amps/mm. Position data at NEFWE is also shown .....	54
3.7	Target Scan Profiles from the Four Luminosity Stations using the NECH dipole for horizontal beam deflections calibrated at 6.29 amps/mm For these beam scans the horizontal beam size is approximately the target size.....	56
3.8	Target Scan Profiles from the Four Luminosity Stations using the NEBV dipole for vertical beam deflections at the target .....	57
4.1	Layout of the Experiment, (a) Elevation (Non-Bend View), (b) Plan View (x-Bend Plane).....	60
4.2	The E-711 Target Station looking downstream along the beam axis. ....	63
4.3	The Luminosity Monitoring System. Four sets of Triple coincidence scintillation counters surround the Target Station. The upstream face and coils of the BM109 Magnet are also shown.....	65
4.4	Measurement of the Y- component of the magnetic field strength along the z-axis .....	69
4.5	Portion of the cross section of the drift chambers. DC1 and DC2 used configuration (a), and DC5, DC3, and DC4 used configuration (b). ....	73
4.6	Schematic view of the Experiment, showing details of the (a) Drift Chambers, (b) Hodoscope, and (c) Calorimeters .....	85
4.7	Front and side views of the calorimeter system. ....	86
4.8	Layout of the Calibration Beam Setup, (a) Elevation (Bend View), (b) Plan View.....	92
4.9	The total energy distribution measured by the calorimeter using the data listed in Table 4.9. The curve shown is a gaussian fit to the data .....	96
5.1	Schematic logic for one of the 24 identical trigger segments and formation of the final triggers .....	104
5.2	Event Display showing the particle tracks, magnetic bending, hodoscope signals and energy deposition in the calorimeters.....	109

5.3	Data Storage Record Structure on the data Tapes .....	113
6.1	Illustration of the track momentum parameters with the positions of the target and bending plane. The slopes are the variables labeled <b>m</b> . The subscripts <b>u</b> and <b>d</b> stand for upstream and downstream..	119
7.1	The track y-vertex position distribution centered around the nominal targeting location. The curve is a gaussian distribution fit to the data.....	130
7.2	The distribution of hits for tracks of unlike sign charged dihadrons that intercept the front face of the calorimeter. ....	132
7.3	The distribution for identified tracks comparing the track momentum and corresponding energy deposition in the calorimeter.....	134
7.4	Event selection by hadron pair mass for the three different charge states.....	136
7.5	A distribution of events testing for the electron simulated hadron showers using the ratio of energy measured in the electromagnetic calorimeter, to the energy measured in the hadronic calorimeter. ....	138
7.6	A graphical representation of the acceptance correction for one table at a $p_T$ limit of 2.0 GeV/c <sup>2</sup> , in the mass bin of 9.0-10.0 GeV/c <sup>2</sup> , with a cosine of the scattering angle and the rapidity bin size of 0.05. This acceptance correction table was used for unlike sign dihadron events.....	142
8.1	The <b>beryllium</b> target data dihadron angular distributions as a function of $\cos\theta^*$ for fixed mass bins. The curves shown are a functional fit to the normalized data. The errors indicated are statistical errors only.....	150
8.2	The <b>aluminum</b> target data dihadron angular distributions as a function of $\cos\theta^*$ for fixed mass bins. The curves shown are a functional fit to the normalized data. The errors indicated are statistical errors only.....	151
8.3	The <b>iron</b> target data dihadron angular distributions as a function of $\cos\theta^*$ for fixed mass bins. The curves shown are a functional fit to the normalized data. The errors indicated are statistical errors only.....	152

8.4	The <b>tungsten</b> target data dihadron angular distributions as a function of $\cos\theta^*$ for fixed mass bins. The curves shown are a functional fit to the normalized data. The errors indicated are statistical errors only.....	153
8.5	The dihadron angular distributions as a function of $\cos\theta^*$ for fixed mass bins using the combined data of the four targets. The curves shown are a functional fit to the normalized data. The errors indicated are statistical errors only.....	155
8.6	The functional fit to the data, parameter <b>a</b> is plotted verses the target atomic number. The higher mass state data and the same functional fit to the QCD Monte Carlo results have been shifted to the right for clarity.....	159
8.7	A representative example of the atomic weight dependence parameter $\alpha$ determined from a linear fit to the scattering cross section as a function of the atomic weight. The data above corresponds to the (+ +) charge state in the mass range $7.0 < M < 7.5$ GeV/c <sup>2</sup> . The value of all the slopes are listed in Table 8.7.....	161
8.8	The atomic weight dependence parameter $\alpha$ is plotted verses the parton-parton scattering angle for the three charge states in the mass range $7.0 < M < 7.5$ GeV/c <sup>2</sup> . For reference, the value of $\alpha = 1.0$ is indicated by the shaded area with a width equal to the error in the global average of all the data values. ....	164
8.9	The atomic weight dependence parameter $\alpha$ is plotted verses the parton-parton scattering angle for the three charge states in the mass range $7.5 < M$ GeV/c <sup>2</sup> . For reference, the value of $\alpha = 1.0$ is indicated by the shaded area with a width equal to the error in the global average of all the data values. ....	165
8.10	A comparison of the E711 data to dijet data from, (a) UA-1 , UA-2 and CDF experiments and (b) CCOR neutral di-pion experiment. The E711 data in (a) corresponds to the (+ -) charge state in the mass range $7.0 < M < 7.5$ GeV/c <sup>2</sup> . The curves correspond to a functional fit to the normalized cross sections of the form (8.1) in the range of the scattering angle shown.....	170
8.11	The dihadron angular distributions as a function of the charge state for E711, and the neutral dipion data from the CCOR experiment. The curves correspond to a functional fit to the normalized cross sections of the form (8.1) . ....	171

8.12	The ratio of the angular distributions as a function of the parton-parton scattering angle, and charge state. Figure (a) corresponds to the mass range $7.0 < M < 7.5 \text{ GeV}/c^2$ , while (b) covers the mass range data $M > 7.5 \text{ GeV}/c^2$ .....	177
8.13	The angular distributions plotted as a function of the variable $\chi$ , and charge state. Figure (a) corresponds to the mass range $7.0 < M < 7.5 \text{ GeV}/c^2$ , while (b) covers the mass range data $M > 7.5 \text{ GeV}/c^2$ .....	178
B.1	Vertical Plane Beam Geometry for the angular deflection from the Vertical bending Magnet NEBV to the E-711 target.....	194
C.1	A single channel for the pre-amplifier circuit and associated circuit.....	196
C.2	Circuit Diagram for the 16 channel chamber amplifier card reproduced from, NANOMETRIC SYSTEMS drawing number N-277-C-01.....	197
C.3	Schematic of the Phototube bases. The R2154 base is shown in (a) and the R239 base is shown in (b). Transistors are: MPS-U10; Diodes are: IN914B; Resistors are: 1/2 W 5% carbon composition.....	198

## ABSTRACT

The angular distribution of hadron pairs produced in the interaction of 800 GeV/c protons on targets of aluminium, beryllium, iron and tungsten have been measured, inferring the underlying dynamics of parton-parton scattering in these interactions. The transverse momentum hadron pairs with  $p_T < 2.0$  GeV/c are studied in three charge states,  $(++)$ ,  $(+-)$ ,  $(--)$  covering the dihadron mass range of 7 to 15 GeV/c<sup>2</sup> and scattering angles up to  $\cos \theta^* = 0.50$ . While the parton-parton angular distributions are shown to be independent of the target type, a small dependence on the charge state of the distributions is observed. These results are found to be generally consistent with the results of leading log QCD calculations. Unlike-sign charge state distributions for this experiment are found to deviate from low x dijet results as expected, and are found to be consistent with neutral dipion production results.

The cross section as a function of the parton-parton scattering angle for the three charge states is shown to vary linearly with the value of the atomic weight. The ratio of the cross sections for different charge states as a function of the parton-parton scattering angle is also found to compare favorably with the predictions of leading log QCD calculations.



# CHAPTER 1

## INTRODUCTION

### §1.1 Elementary Particle Scattering

It is the study of nature that ultimately leads physicists to investigate the basic constituents of matter. We believe that the smallest constituents interact at a fundamental level and that the interaction is governed by the fundamental forces of nature. These building blocks of matter, which we call elementary particles, mediate their interaction by exchanging particles within the constraints of the fundamental forces. We have classified these forces into four types: the gravitational, a long range force; the weak force which is exhibited in radioactive decay; the electromagnetic force which is mediated by photon exchange; and the strong nuclear force. A distinguishing characteristic of these forces is that they act over widely varying distances, gravity being the weakest along with electromagnetism acting over the longest range, while the strong force is the strongest, characterized by the interaction among hadrons and their composites. It has been discovered that the electromagnetic and the weak forces can be combined into the same type of force known as the electro-weak force, which is mediated by the intermediate vector bosons and the photon. To understand these forces and the rules by which the matter interacts requires a knowledge of the composition of matter and the structure that is formed. Thus the structure of matter is divided into

smaller and smaller parts until we reach what is referred to as the fundamental level. The smallest parts are known as elementary or fundamental particles, and the probing of materials with these energetic projectiles provide information about some of the properties of these particles as well as the materials. This is the process of particle scattering. By observing how particles scatter in collision with material and other particles, we can draw conclusions about some of their properties and apply theoretical models to predict other properties.

In the early part of the 20th century, J. J. Thomson<sup>1</sup> proposed an atomic theory of matter that would explain the scattering of charged particles by thin foils of material. Credible experimental evidence, such as the photoelectric effect in metals, ionization in gases, and experiments with x-rays supported the idea that electrons existed in all atoms. Thomson's atomic model consisted of a uniform sphere of positive charge with a radius of one atomic unit, in which the electrons would be embedded. This model was used to predict the large angle scattering of alpha particles of known energy from thin gold foils. The prediction of the model indicated that the number of particles scattered through large angles was extremely small, while the work of Geiger and Marsden<sup>2</sup> showed that about one particle in  $10^4$  was scattered through  $90^\circ$  or more, a significant difference from the prediction.

As a result of this excess large-angle scattering of alpha particles, Rutherford<sup>3</sup> proposed the nuclear model of the atom in which the positive charge was located at the center of the atom. This large angle scattering suggested massive point like constituents for the atom.

The energy available for probing deeper into the structure of matter has increased because of the invention of particle accelerators. With this higher energy, it has been observed that the nucleus proposed by Rutherford is not a point, but is made up of smaller particles which we call protons and neutrons. At even higher energies<sup>4</sup>, it was found that protons and neutrons are not fundamental either, but appear to have substructure made of what we call partons. The high incident energy makes it possible to delve deeply into the structure of the nucleon.

By colliding large numbers of particles with target materials, it is possible to measure many quantities. Typical measured quantities are the scattering cross section, and the angular distribution. Measuring the number of particles scattered at different angles will produce the angular distribution, and summing the total number measured at all angles compared to the incoming rate of particles will lead to the size of the target (i.e. the cross section). Of course many other reactions can occur in a simple scattering of two particles, which can make the results of experiments difficult to interpret. On the other hand, the ability to compare individual attributes of slightly different experiments can provide important information about the particle properties. Thus, from the time of Thomson in 1910 (and perhaps before), to the present 1991, we still successfully use the method of particle scattering to measure various quantities and compare with theoretical ideas.

## **§1.2 The Experiment E-711**

The experiment, known as Experiment 711 (E-711) was designed to measure the angular dependence, charge dependence and atomic weight dependence of massive di-hadron production in collisions of 800 GeV protons with a variety of stationary nuclear targets. It is generally accepted that hadronic matter is composed of sub-constituents known as partons (quarks and gluons). The deep inelastic scattering of hadronic matter, resulting in high momentum transfer can lead to information that is helpful in determining some of the basic properties of these partons. The constituent scattering experiment was proposed to the Fermi National Accelerator Laboratory (FERMILAB) in late 1982 and approved July 1, 1983. The procedure for proposing experiments usually consists of a written proposal, and a presentation to the laboratory management and an external advisory committee. At the proposal stage, all of the physicists in the group made contributions to various parts of the design of the apparatus and the physics goals of the experiment. The experimental work described in this dissertation results from the collective efforts and contributions of these physicists. Our collaboration ultimately consisted of physicists from Fermilab (3 persons, and the author's exclusive institutional affiliation at the time), The University of California at Davis (1 person), The University of Michigan (2 persons), and The Florida State University (8 persons). With the approved status of our experiment, we built the detector system, installed all of the initial apparatus, and began calibrating the detector. At the conclusion of the calibration process, we

began to take our first data in limited experimental runs during 1985 and 1987, and concluded our data collection in February 1988.

E-711 took data that have been used to investigate parton-parton scattering properties by studying the production of hadrons at high transverse momentum ( $p_T$ ), that is at  $p_T > 2$  GeV/c. At high- $p_T$ , the usual production mechanism and some interaction properties prevalent at low- $p_T$  are found to have negligible cross sections<sup>5</sup>. When an experiment triggers on single high- $p_T$  particles, the events generated exhibit certain properties:

1. If the transverse momentum of the trigger particle is sufficiently high (i.e.  $p_T > 7$  GeV/c), a "jet" of spatially collinear hadrons is usually observed recoiling from the trigger particle.
2. The fraction of the trigger side jet momentum ( $z_{\text{trig}}$ ) taken by the trigger particle typically ranges from 75% to 90%.

Events selected by requiring the detection of a single high- $p_T$  hadron (as opposed to a jet trigger) leads to the use of a trigger hadron momentum as an approximation of the scattered parton momentum due to the large momentum fraction,  $z_{\text{trig}}$ . On the other hand exploiting this feature in measuring the parton-parton scattering amplitudes for single particle measurements fail, because of the uncertainty due to the Fermi motion (the intrinsic transverse momentum) and the tendency for the initial state to be moving in the trigger particle direction. These problem are greatly reduced by selecting symmetrically triggered events. In the case of the di-hadron system, two particles at a time are identified so that their large

transverse momenta approximately balance, enabling the study of the parton-parton scattering system. In this sense the mass of the di-hadron system is an approximation of the center of mass parton-parton scattering energy, and the angle of the hadron direction relative to the proton beam line is considered the parton-parton scattering angle.

Thus by studying the angular dependence of this di-hadron system, one can indirectly study angular dependent properties of the parton-parton system. Many of these properties are studied in colliding beams experiments which can provide the highest attainable center of mass scattering energy available. On the other hand this experiment, known as a fixed target experiment, was designed to include a heretofore unique measurement of the different charge states of the particle pair, (i.e.  $++$ ,  $+-$ ,  $--$ ), and a feature that decoupled the trigger on high- $p_T$  particles from the reconstruction of the track momentum. In addition the experiment took advantage of the much higher luminosity available with fixed target experiments.

### **§1.3 Guide To This Dissertation**

This chapter gives a general overview of scattering and an introduction to the experiment. Chapter 2 offers a review of historical and theoretical background in hadronic interactions at high transverse momentum, the theory of quantum chromodynamics, and hadronic pair production. In chapter 3 the proton beam is described and the methods used to control the beam, since beam targeting was crucial to this experiment. The technical description of the experimental apparatus is

discussed in chapter 4, namely the targeting system and those elements downstream of the target system. Chapters 5 and 6 offers information on the data acquisition and data processing, with the analysis of the data presented in chapter 7. The results of this study and conclusions follow in the last two chapters.

## CHAPTER 2

### THEORETICAL & EXPERIMENTAL PHYSICS OVERVIEW

#### §2.1 Historical Perspective

In the late 1960's attention was drawn to the production of particles resulting from the inelastic collision of hadrons. (The term hadron refers to particles that are subject to the strong interactions). These particles were interpreted as the products of the hard scattering of elementary constituents within the hadrons. Evidence for the existence of point-like scattering centers within the proton had been found in deeply inelastic electron-proton scattering experiments<sup>6</sup>. But in addition to the point-like constituent explanation, was the dependence of the hadron production on transverse momentum in hadron-hadron collisions. The hadrons produced at large angles were reminiscent of large angle alpha particle scattering in Rutherford scattering experiments. So it was natural perhaps to draw parallel conclusions between large angle Rutherford scattering leading to atomic structure, and large transverse momentum particle production in proton-nucleon collisions and electron-proton scattering, leading to nucleon structure. Therefore based partly on the general properties of the scaling of multiplicities with center-of-mass energy in hadronic interactions, Richard P. Feynman proposed the parton



model for hadrons<sup>7</sup>, in which the hadron was viewed as a composite object composed of independent point-like scattering centers.

Gell-Mann<sup>8</sup> and Zweig<sup>9</sup> in the early 1960's proposed quarks as the constituents of hadrons. Hadrons are composed of two classes of particles: mesons, which have integer spin, and baryons which have half integer spin. The quarks were originally proposed as the generators of a symmetry group known as SU(3), and served as a classification scheme for the many particles discovered before that time. Three quark "flavors" accounted for the spectrum of observed particle ground and excited states, and in fact the theory was successful in predicting the existence of a triple strangeness particle, which was subsequently discovered in a bubble chamber experiment in 1964 and named the omega minus baryon. (The quark "flavor" specifies the quantum number which is conserved in its strong interactions). Initially there were three flavors of quarks, the u, d, and s (designated "up", "down", "strange"), which could be combined to form the three-quark baryon states and the quark-antiquark meson states. Later on three additional quarks were postulated; c, t and b ("charm", "top", "bottom"). Since the quarks could not be effectively isolated (or at least have not been experimentally observed individually) particle structure has been investigated only on the basis of the existence of particle bound states. With the addition of a new quantum number termed "color"<sup>10</sup>, which can have three possible values, six flavors of quarks (u,d,c,s,t,b) are required and sufficient to account for the measured spectrum of these bound states. It is also known that all of the observed bound states to date, can be accounted for by just five flavors of quarks, excluding the "t" quark.

Many models present mechanisms that describe how the elementary particles will interact. The basic particles are summarized in a symmetry grouping, (  $SU(3) \otimes SU(2) \otimes U(1)$  ), called the Standard Model, including matter particles and the particles that mediate the basic forces of nature. This information is summarized in Table 2.1. It should be noted however, that as of this writing, evidence has not been observed for two of these particles, "t", the top quark, and "H<sup>0</sup>", the Higgs particle.

In the early part of the 1970's the results of an experiment<sup>11</sup> at the European Laboratory for Particle Physics (CERN), lead to a reassessment of single hadron production in proton-proton collisions. A prevalent model at the time was a thermodynamic or statistical interpretation of particle production referred to as a fireball model.<sup>12</sup> In this model some of the kinetic energy of the colliding hadrons is converted into a fireball or spatially localized high energy plasma of hadrons from which secondary particles are expected to be produced isotropically as the plasma cools. This model described some aspects of the interaction very well, such as the exponential distribution of the energies at low transverse momentum, (i.e. below 800 MeV/c). But it did not explain the fact that most of the energy went into the longitudinal degrees of freedom. The CERN experiment mentioned before, however, produced measurements of the cross section for neutral  $\pi$  mesons that dropped off far less steeply than predicted by contemporary models. So the existence of partons in hadronic collisions was accepted but the nature of the partons still needed to be studied.

Table 2.1  
The Standard Model \*

The Matter Particles (Fermions and their antiparticles)				
				Interaction Type
Leptons	$\begin{pmatrix} \nu_e \\ e^- \end{pmatrix}$	$\begin{pmatrix} \nu_\mu \\ \mu^- \end{pmatrix}$	$\begin{pmatrix} \nu_\tau \\ \tau^- \end{pmatrix}$	$\leftarrow$ Weak
				$\left\{ \begin{array}{l} \text{Weak} \\ \text{Electromagnetic} \end{array} \right.$
Quarks (3 Colors)	$\begin{pmatrix} u \\ d \end{pmatrix}$	$\begin{pmatrix} c \\ s \end{pmatrix}$	$\begin{pmatrix} t \\ b \end{pmatrix}$	$\left\{ \begin{array}{l} \text{Strong} \\ \text{Weak} \\ \text{Electromagnetic} \end{array} \right.$

The Force Particles (Bosons)		
$g_i$	Mediates the Strong Interaction	(i=1,8 colors)
$\gamma$	Mediates the Electromagnetic Interaction	
$W^\pm, Z^0, \gamma$	Mediates the Electro-Weak Interaction	
$H^0$	Unobserved particle which gives mass to the W and Z bosons and the fermions	

\*Elementary Particles (circa 1990)

Another possible configuration for the parton was a bound state of two quarks. The model known as the Constituent Interchange Model proposed that the scattering occur between a single quark and a di-quark bound state<sup>13</sup>. This model agreed with the observed result that the hadron production cross section varies inversely with the eighth power of the transverse momentum for fixed values of  $x_T = 2 p_T / \sqrt{s}$  and scattering angle  $\theta$ . On the other hand, this model implied that the production of positive pions at transverse momentum greater than 2 GeV/c would exceed the production of negative pions by a factor of three, in collision of positive pions with protons. This difference was not observed in subsequent experimental results.<sup>14</sup> By 1980 the CIM model had been shown not to agree with one particle inclusive reactions.

In 1970 the GIM (Glashow, Iliopolus, and Maiani) mechanism<sup>15</sup> was proposed which incorporated, in addition to the u, d, and s quarks, a new quark first suggested by Bjorken, Glashow and others. The motivation for the model beside the symmetry between the 4 leptons and the 4 quarks of the SU(4) classification scheme for hadrons, was an attempt to explain the difference between predicted and observed decay rates of neutral K-mesons. The "November Revolution" in 1974 significantly enhanced the acceptability of the quark model. In two separate experiments, one at the Brookhaven National Laboratory and the other at the Stanford Linear Accelerator Center (SLAC), a new particle was observed and named the  $J/\psi$  meson. The  $J/\psi$  was found to have a lifetime characteristic of electromagnetic decays, and found to be composed of constituents carrying a new quantum number (called "charm", or the c quark) which was

conserved in the strong interactions and was previously incorporated in the GIM model. This particle was soon accepted to be composed of a bound state of a charm and an anti-charm quark, ( $c\bar{c}$ ). In 1977 at Fermilab, another meson, the  $\Upsilon$ , was discovered which was thought to be composed of a bound state of "bottom" quarks ( $b\bar{b}$ ). Even though the "top" ( $t$ ) quark has not been observed yet, these discoveries, continue to provide evidence that the observations seem consistent with the standard theoretical model.

The constituent scattering models, successfully describe some aspects of hadron scattering, but differ in their ability to predict some properties of the processes that occur in the collisions. None-the-less the prevailing conclusion is that the physics observations tend to be consistent with models that involve the scattering of point-like particles at high energies.

## **§2.2 Quantum Chromodynamics and Partons**

The success of  $e^+ e^-$  and deep inelastic experiments that confirmed the existence of point-like scattering constituents in hadrons led Berman, Bjorken, and Kogut<sup>16</sup> to formulate a model for hadron production (with  $p_T$  much greater than 1 GeV/c) at high energies. This model also predicted multiple cores of hadrons produced from hadronization of the interacting quarks. They also suggested parton interaction based on spin 1 gluon exchange. During the late 1970's, Feynman and Field proposed a hard quark-quark scattering model, which provided explanations of the dependence of inclusive single hadron cross sections on transverse momentum and center-of-mass energy.<sup>17</sup> In this model individual

constituents of each colliding hadron interact, scatter and fragment to form the final state hadrons. The hypothesis of this model is that each process is considered to occur independently. So the attempt was made to mathematically describe and investigate each distinct part of the interaction. Moreover the fundamental interactions within the hadron scattering process are thought to be consistent with particles formed with large transverse momentum (high- $p_T$ ).

This high- $p_T$  scattering is described by the theory of quantum chromodynamics (QCD)<sup>18,19</sup>. In QCD, the quarks interact through the strong interaction mediated by the exchange of a gluon. Both the quarks (3 colors) and the gluons (8 colors) possess a color quantum number, and the combination of these particles must result in color singlet bound states. Baryons therefore form distinct (three colors) colorless states, and mesons form color-anticolor singlets. Since the subparticles cannot be dynamically isolated from one another, the QCD parton model must provide a description of the internal processes which are in accord with the dynamics of the hadron scattering. The parton model consists of the following major and distinct parts in considering the hard scattering process.

a) The interacting hadrons are described by structure (or distribution) functions  $G_{q/h}$ , which gives the probability density for finding a particular parton ( $q$ ) with a particular momentum fraction within the hadron ( $h$ ) between  $x$  and  $x + dx$ . The structure functions for nucleons can be derived from measurements of deep inelastic lepton-nucleon scattering experiments<sup>20</sup>. The lepton-nucleon scattering experiments play an

important role in the exploration of QCD. In addition to providing evidence for the existence of quarks, these experiments also indicated that only about 50% of the total energy observed was carried by the charged constituents. The rest of the energy was attributed to the "glue" that binds the partons strongly together.

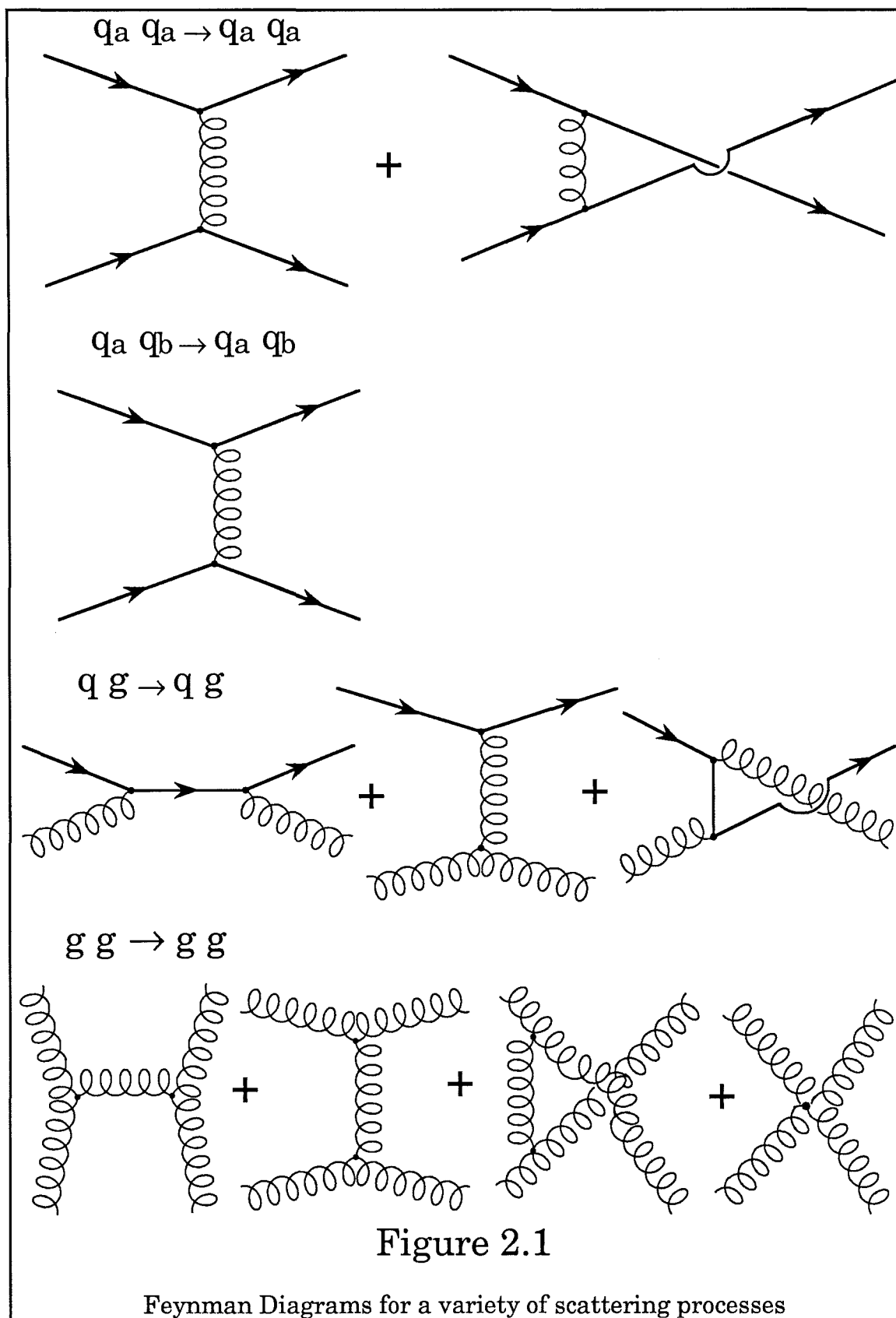
b) One constituent within each of the target and beam particles interacts in the hard collision with some differential cross section that can be calculated using perturbative QCD<sup>21,22</sup>. A variety of subprocesses important to high- $p_T$  hadron production are tabulated in Table 2.2, and Feynman diagrams corresponding to these processes are shown in Figure 2.1. The subprocesses for distinguishable quarks, nondistinguishable quarks, quark-gluon and gluon-gluon interactions are listed. There are also four similar processes that involve antiparticles in these reactions. The symbols  $\hat{s}$ ,  $\hat{t}$ , and  $\hat{u}$  are called the Mandelstam variables, where the " $\hat{\phantom{x}}$ " indicates the parton instead of the hadron properties. These variables will be defined in the next section of this chapter. In Figure 2.1, the straight lines correspond to the quarks and the looped strings represent the gluons.

## Table 2.2

First Order QCD Cross Sections <sup>23</sup>

Subprocess	Cross Section ( $d\sigma/d\hat{t}$ )
$q_a q_b \rightarrow q_a q_b$	$\frac{\pi\alpha_s^2}{\hat{s}^2} \left( \frac{4}{9} \frac{\hat{s}^2 + \hat{u}^2}{\hat{t}^2} \right)$
$q_a q_a \rightarrow q_a q_a$	$\frac{\pi\alpha_s^2}{\hat{s}^2} \left[ \frac{4}{9} \left( \frac{\hat{s}^2 + \hat{u}^2}{\hat{t}^2} + \frac{\hat{s}^2 + \hat{t}^2}{\hat{u}^2} \right) - \frac{8}{27} \hat{s}^2 \right]$
$q g \rightarrow q g$	$\frac{\pi\alpha_s^2}{\hat{s}^2} \left[ -\frac{4}{9} \left( \frac{\hat{s}}{\hat{u}} + \frac{\hat{u}}{\hat{s}} \right) + \frac{\hat{s}^2 + \hat{u}^2}{\hat{t}^2} \right]$
$g g \rightarrow g g$	$\frac{\pi\alpha_s^2}{\hat{s}^2} \left[ \frac{9}{2} \left( 3 - \frac{\hat{t}\hat{u}}{\hat{s}^2} - \frac{\hat{s}\hat{u}}{\hat{t}^2} - \frac{\hat{s}\hat{t}}{\hat{u}^2} \right) \right]$





c) Following the hard scattering, each parton that participated in the collision is thought to fragment, such that the scattered partons produce a "jet" (same as the name "cores" mentioned earlier) of observable hadrons. The word "jet" means that these groups of particles are thought to move essentially in the same direction of the original parton. The momentum of the jet and the partons are nearly equal, and the probability density for observing a hadron ( $\mathbf{h}$ ) with some momentum fraction of the parent parton ( $\mathbf{q}$ ) can be described by what is known as a fragmentation function,  $D_{h/q}$ , which can be determined from experimental measurements.

The processes for lepton-nucleon scattering and hadron production through electron-positron annihilation are shown in Figure 2.2. In the first process the lepton, (for this case a neutrino) probes the nucleon providing a measurement of the cross section for the hadron produced in the final state, which are used in the calculation of a distribution function for the nucleon. In the second process, an electron and positron annihilate into a quark anti-quark pair with the quark fragmenting into a hadron, from which the fragmentation functions are determined. The "glue" mentioned earlier that holds the quarks together, consists of gluons, and evidence for their existence was first observed in electron-positron annihilation experiments. The bulk of the events observed are two jet events<sup>24</sup> first seen in 1977 at the 8 GeV SPEAR (Stanford) accelerator facility. It had been predicted that at high momentum transfers and high

center of mass energies, quarks can radiate an energetic gluon at a large angle with respect to the direction of the two jets, which leads to an isolated third jet<sup>25</sup>. When a higher energy 30 GeV electron-positron collider facility (PETRA) was made operational in 1979, about 10% of the jet events observed showed a three jet behavior in the presence of a majority of expected two-jet events.<sup>26,27,28,29</sup> All of the salient features were consistent with the predictions for hard gluon emission. Hadron pair production and jets will be discussed in a later section of this chapter.

The hard scattering process<sup>30</sup> as illustrated in Figure 2.3 presents schematically, the collision of two hadrons **A** and **B** with distribution functions  $G_{a/A}$  and  $G_{b/B}$ , and the subsequent interaction through a cross section  $d\sigma/d\hat{t}$  of the individual associated partons **a** and **b** producing the final scattered partons **c** and **d**. The scattered partons fragment, specified by the functions  $D_{H_1}$  and  $D_{H_2}$  into the final hadrons **H<sub>1</sub>** and **H<sub>2</sub>**.

When these major parts, (the fragmentation functions; the structure functions; the cross sections and the appropriate coupling constants) are combined together, a cross section can be calculated for the production of hadrons<sup>31</sup>, from the hard scattering of hadronic constituents.

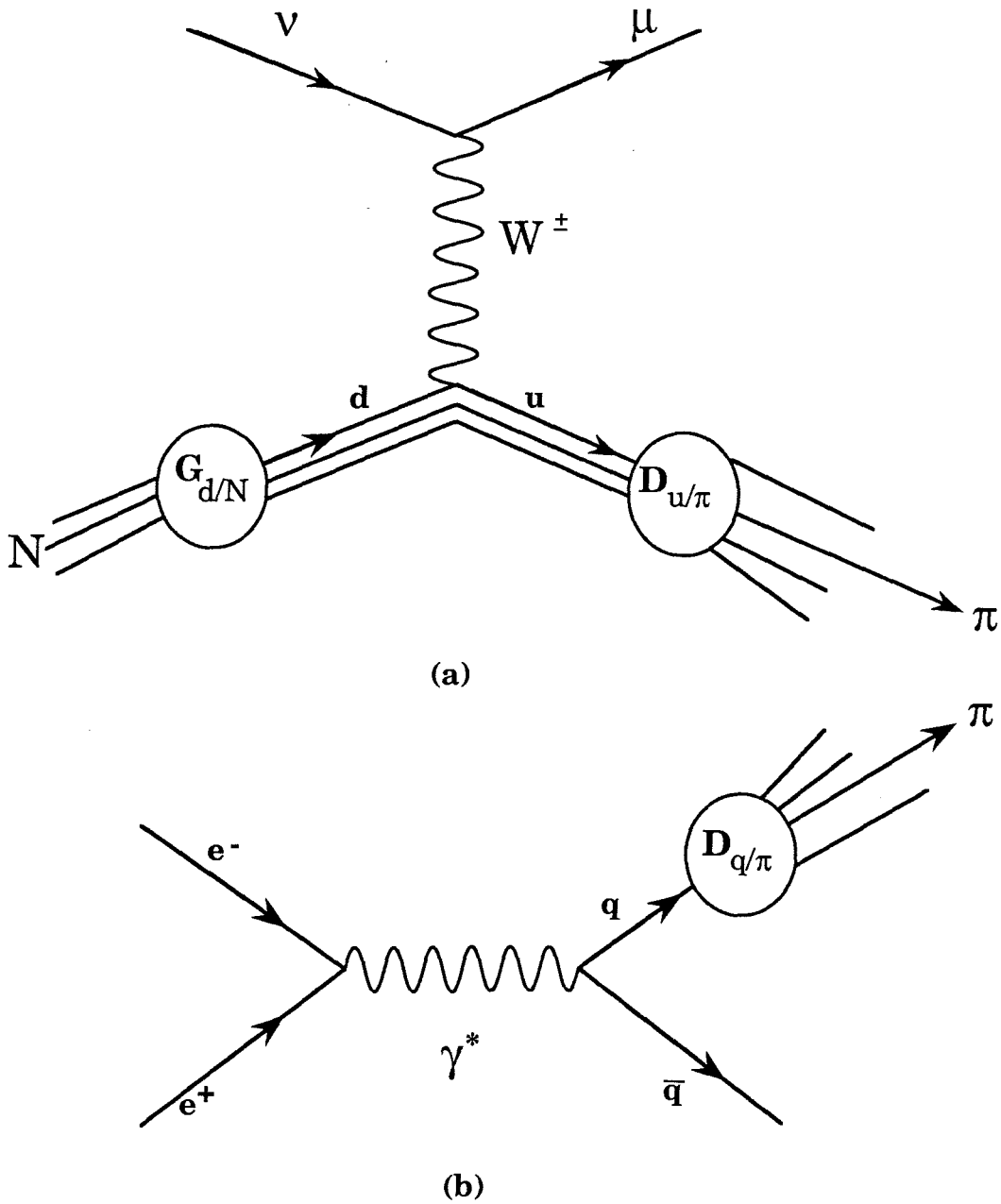


Figure 2.2

Illustrative diagrams of : (a) Lepton-Nucleon Scattering and  
 (b) Electron-Positron annihilation and hadron production

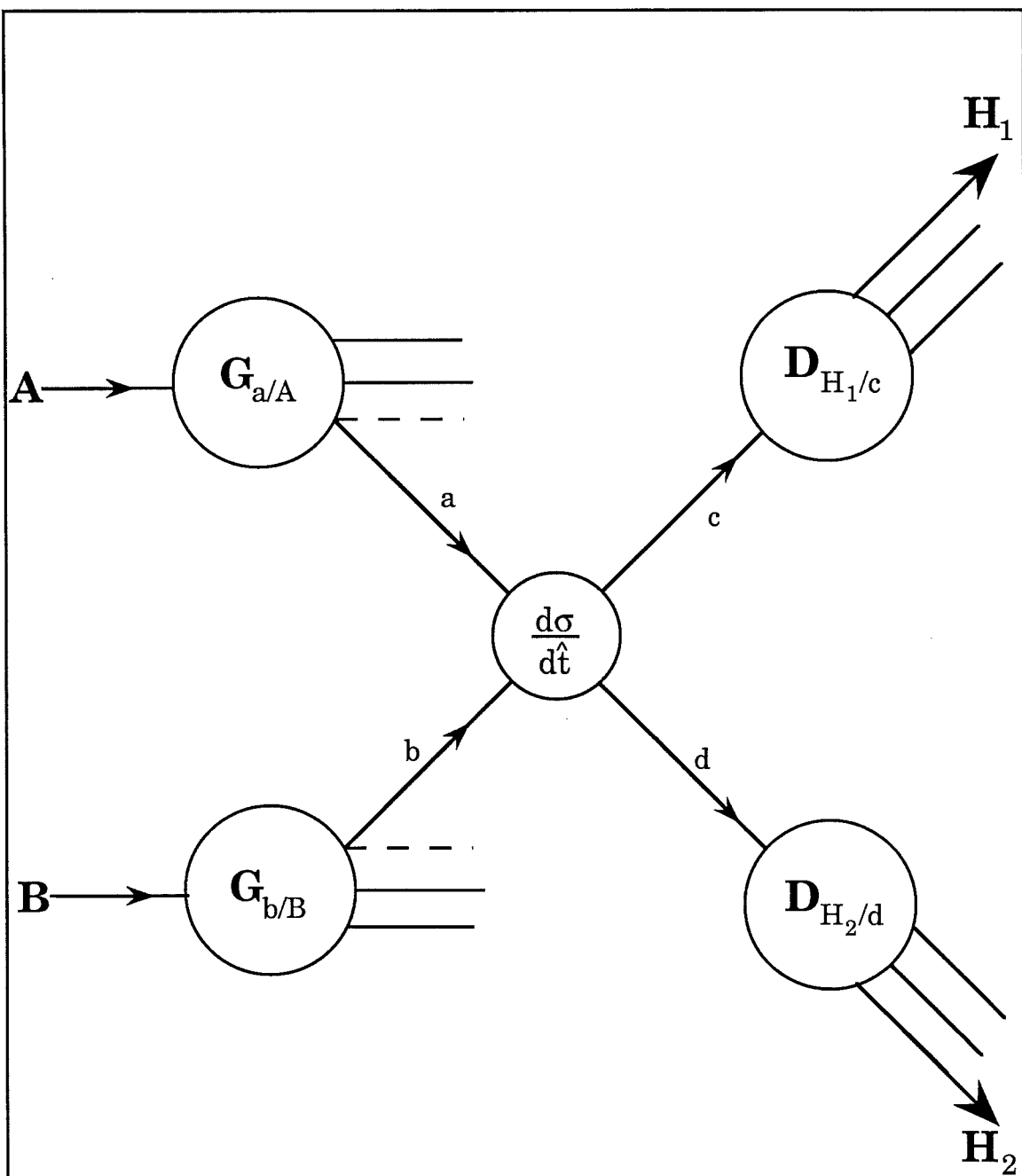


Figure 2.3

The hard scattering process in the parton model

### **§2.3 Large Transverse Momentum Hadronic Interactions**

Since high- $p_T$  hadron scattering involves many different subprocesses,  $Q^2$  can be defined by different kinematic variables. In fact  $Q^2$  is any dimensionally correct collection of variables which characterizes the momentum transfer in the hard scattering. One definition proposed by Feynman, Field, and Fox<sup>32</sup>, for  $Q^2$  is:

$$Q^2 = \frac{2 \hat{s} \hat{t} \hat{u}}{\hat{s}^2 + \hat{t}^2 + \hat{u}^2} \quad (2.1)$$

where  $\hat{s}$ ,  $\hat{t}$ , and  $\hat{u}$  are the Mandelstam variables. These variables are defined in terms of the incoming (a,b) and outgoing (c,d) partons as:

$$\begin{aligned} \hat{s} &= (p_a + p_b)^2 \\ \hat{t} &= (p_a - p_c)^2 \\ \hat{u} &= (p_a - p_d)^2 \end{aligned} \quad (2.2)$$

Another possible definition of  $Q^2$  is :

$$Q^2 = \frac{\hat{t} \hat{u}}{\hat{s}} \quad (2.3)$$

which is equivalent to  $p_T^2$  or the square of the momentum transfer of each scattered parton. This is the value of  $Q^2$  assumed in this analysis. The advantage of this selection is that it is more directly connected to experiments, since the scattered partons fragment into leading hadrons whose transverse momenta can be measured.

At higher and higher energies, one expects to observe higher momentum transfers between the constituents of the beam particles and the target particles. Normally one parton in each of the colliding hadrons is involved in the scattering. The disintegration of the colliding hadrons, the interaction of the fundamental constituents, and the fragmentation to the final state hadrons are combined together in the leading log collinear kinematics to produce the inclusive cross section for producing a high transverse momentum hadron:

$$\begin{aligned}
 E_C \frac{d^3\sigma}{dp_c} (A + B \rightarrow C + X) \\
 = \frac{1}{\pi} \sum_{abc} \int dx_a \int dx_b \int dz_c G_{a/A}(x_a, Q^2) G_{b/B}(x_b, Q^2) D_{C/c}(z_c, Q^2) \\
 \frac{\hat{s}}{z_c^2} \frac{d\sigma}{d\hat{t}} (ab \rightarrow c) \delta(\hat{s} + \hat{t} + \hat{u})
 \end{aligned} \tag{2.4}$$

The differential cross section can be written in terms of the matrix element  $|\mathcal{M}|^2$  as:

$$\frac{d\sigma}{d\hat{t}} = \pi \alpha_s(Q^2) \frac{|\mathcal{M}|^2}{\hat{s}^2} \tag{2.5}$$

The matrix elements are calculated using QCD, and are shown as part of the cross sections previously presented in Table 2.2.

The functions  $G(x)$  and  $D(z)$  have a dependence on  $Q^2$  which is specified by QCD<sup>33</sup>. The higher energy particle scattering and the higher momentum transfers, means smaller impact parameters and smaller

coupling constants. The QCD coupling constant depends on the value of  $Q^2$  according to the following formula:<sup>34</sup>

$$\alpha_s(Q^2) = \frac{12\pi}{(33 - 2n_f) \ln(Q^2/\Lambda^2)} \quad (2.6)$$

where  $n_f$  denotes the number of quark flavors, and  $\Lambda$  is a scale parameter determined from fits to structure function measurements.

## **§2.4 Hadronic Pair Production and Jets**

High- $p_T$  hadron production is believed to be due to wide angle scattering of the hadronic constituents. It has been experimentally observed that when events are selected by the presence of a single high- $p_T$  particle (i.e. single particle trigger), various properties of the interaction becomes evident.<sup>5</sup> Namely, the trigger particle is associated with collinear, correlated hadrons (i.e. jets); the observation of a recoiling jet from the trigger particle; and a large fraction of the trigger side jet momentum is carried by the trigger particle. When events are selected based upon a single high- $p_T$  hadron, instead of a jet, then the trigger hadron momentum might be used as an approximation to the scattered parton momentum. However, measuring only one initial parton in high- $p_T$  production may not fully measure the parton-parton scattering amplitudes. The tendency of the initial target particle to move in the same direction as the trigger particle after the interaction, the absence of information on the recoil system kinematics, and uncertainties due to intrinsic particle motion (i.e. Fermi motion), introduces complications in the interpretation of single particle measurements.<sup>35</sup> This is also true for



jets as well, but endemic to single arm measurements. By taking symmetrically triggered events, many of these problems are reduced.<sup>36</sup>

One simple symmetric trigger would be selecting two high- $p_T$  hadron events with roughly equal and opposite transverse momentum, recoiling from each other at about  $x_F = 0$ , where  $x_F$  is the fraction of hadron momentum difference to the center of mass energy,  $\sqrt{s}$ . In the case where  $z_1 = z_2 = 1$  then:

$$x_F = 2 (P_{z_1} - P_{z_2}) / \sqrt{s} = x_1 - x_2 \quad (2.7)$$

$P_z$  is the hadron momentum component along the beam direction.

$x$  is the ratio of the parton momentum to the proton momentum.

This symmetric trigger allows one to study the kinematics of the scattered constituents more completely than the single particle trigger. For this case, in the limit that their transverse momenta balance, the di-hadron invariant mass is then an approximation of the center of mass energy  $\sqrt{s}$  of the parton-parton scattering system and the angle of the di-hadron axis relative to the beam line, is an approximation to the parton-parton scattering angle. Doing the experiment at  $x_F \approx 0$  insures that both target and beam partons are in the valence region (i.e. the region of the parton distribution where the momentum fraction  $x > 0.3$ ). In this region one expects that the interactions taking place are due to the partons that carry a larger fraction of the momentum of the nucleon. At lower  $x$ , interactions due to sea quarks and gluons would dominate. Thus measuring the angular dependence of the dihadron axis at  $x_F = 0$  permits study of the angular dependence of the parton-parton interaction.

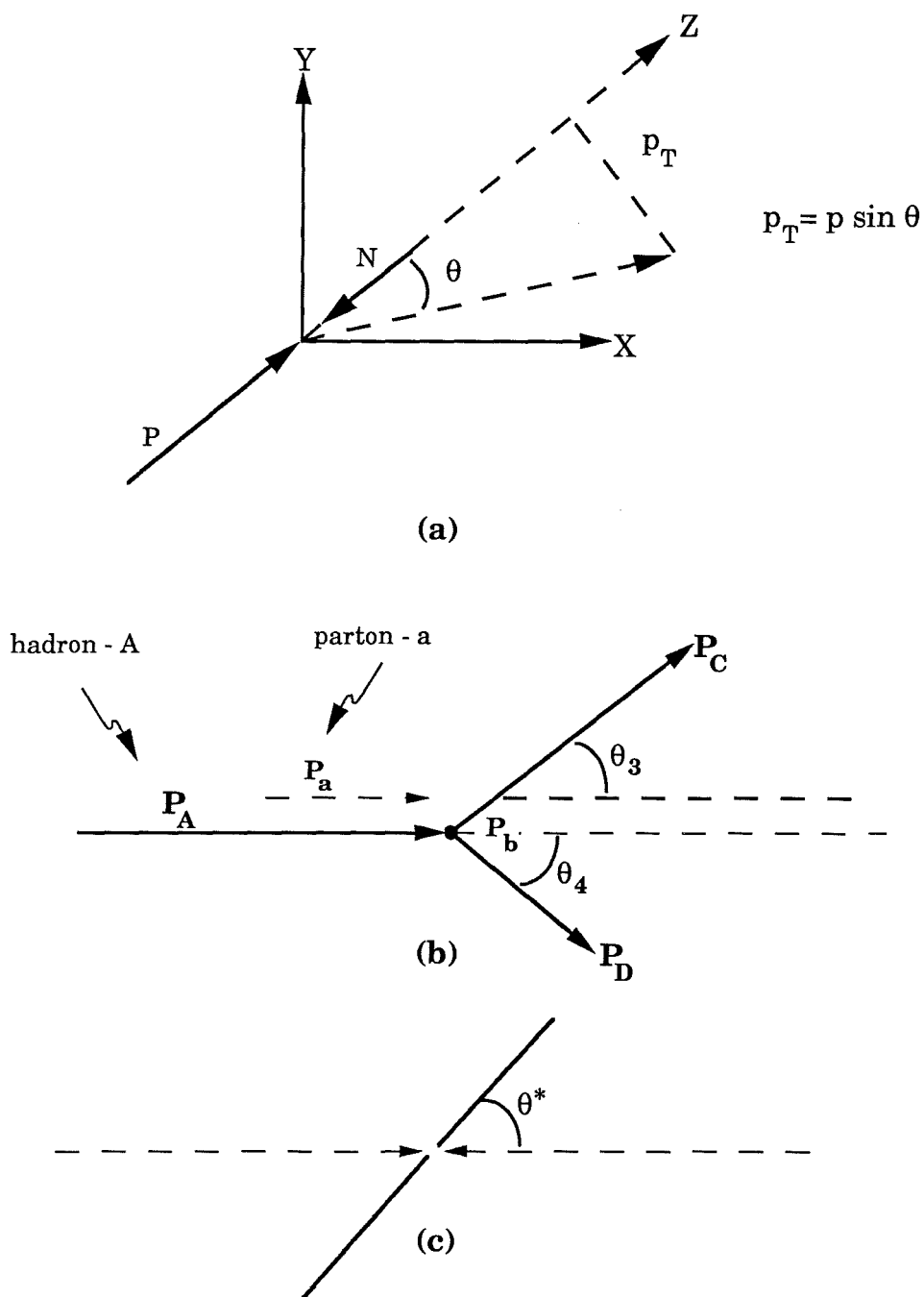


Figure 2.4

Illustrative diagrams of : (a) Transverse Momentum with respect to the Beam Axis ,  $Z$  (b) P-N Scattering, Lab Frame.  $P_a, P_b$  are partons,  $\theta_3, \theta_4$  are outgoing scattering angles, and (c) Parton-Parton Center of Mass Scattering Frame

FIGURES 2.4a and 2.4b illustrate the coordinate system for the particle-particle collision. Relations can be derived that associates parton-parton variables with quantities measured in the laboratory. In the Proton-Nucleus center of momentum frame, the momentum, transverse to the beam direction, is given by:

$$p_T = p \sin(\theta) \quad (2.8)$$

where  $\theta$  is the transverse angle to the beam. Figure 2.4c shows the parton-parton center of mass scattering angle  $\theta^*$ , (the polar angle between the di-hadron axis and the beam direction). With respect to the hadron momenta, the Mandelstam variables can be rewritten using  $\theta$ , and the parton-parton center of mass scattering angle ( $\theta^*$ ) as :

$$\begin{aligned} \hat{s} &= (p_a + p_b)^2 = x_a x_b s = \frac{1}{2} x_T s \left( x_a \tan \frac{\theta}{2} + x_b \cot \frac{\theta}{2} \right) \\ \hat{t} &= (p_a - p_c)^2 = -\frac{1}{2} x_T s x_a \tan \frac{\theta}{2} = -\frac{\hat{s}}{2} (1 - \cos \theta^*) \\ \hat{u} &= (p_b - p_c)^2 = -\frac{1}{2} x_T s x_b \cot \frac{\theta}{2} = -\frac{\hat{s}}{2} (1 + \cos \theta^*) \end{aligned} \quad (2.9)$$

With the initial parton transverse momentum, and all masses equal zero (for illustration), the initial parton momentum fractions can be written:

$$x_a = 2 p_a / \sqrt{s} \quad , \quad x_b = 2 p_b / \sqrt{s} \quad , \quad (2.10)$$

while the scaled transverse momentum of the outgoing parton is :

$$x_T = 2 p_T / \sqrt{s} \quad (2.11)$$

Using Eq. 2.9 in the parton-parton rest frame with  $p_T = \frac{\sqrt{\hat{s}}}{2} \sin \theta^*$ , leads to

$$\hat{t} \hat{u} = \frac{\hat{s}^2}{4} \sin^2 \theta^* = \hat{s} p_T^2, \quad (2.12)$$

and this equation gives a correlation between the transverse momentum measured and the parton-parton scattering angle. Furthermore, additional correlations can be given as follows<sup>37</sup>:

$$\text{From Eq. (2.12)} \quad \sin^2 \theta^* = 4 \frac{\hat{t} \hat{u}}{\hat{s}^2}$$

$$\text{where} \quad \left. \begin{aligned} \hat{s} &= x_a x_b s \\ \hat{t} &= \frac{z_c}{x_a} \hat{t} \\ \hat{u} &= \frac{z_d}{x_b} \hat{u} \end{aligned} \right\} \quad \text{and} \quad \begin{cases} t = (P_{\text{Beam}} - P_{H_1})^2 \\ u = (P_{\text{Beam}} - P_{H_2})^2 \end{cases} \quad (2.13)$$

The variable  $z_q$  is the momentum fraction of the outgoing partons, and  $P_{\text{Beam}}$  and  $P_{H_q}$  are the beam momentum and the hadron momentum measured in the laboratory. The square of the invariant mass of the dihadron system is

$$M^2 = (P_1 + P_2)^2 \quad (2.14)$$

then  $M^2 = z_c z_d \hat{s} = z_c z_d x_a x_b s$

$$\text{so that} \quad \sin^2 \theta^* = 4 \frac{t u}{s^2} \frac{x_a x_b}{z_c z_d (x_a x_b)^2} = 4 \frac{t u}{s M^2}, \quad (2.15)$$

where all quantities can be measured in the laboratory:

$$\begin{aligned}
& \text{i.e.} \quad s = \text{total energy} \\
& \quad t = (P_{\text{Beam}} - P_{H_1})^2 \\
& \quad u = (P_{\text{Beam}} - P_{H_2})^2
\end{aligned}$$

From the inclusive scattering cross section for hadron pair production into two partons, with variables which are measured in the center-of-mass of the hadron-hadron system, the differential cross section in the leading log approximation can be written as :

$$\begin{aligned}
& \left. \frac{d^4 \sigma}{dM^2 dY d\eta d\cos \theta^*} \right|_{Y=\eta=0} = \\
& \sum_{abcd} \int dx_a dx_b \frac{2 x_a}{\sin \theta^*} G_{a/A}(x_a, Q^2) G_{b/B}(x_b, Q^2) \frac{d\sigma}{d\hat{t}}(a + b \rightarrow c + d) \\
& \quad D_{C/c}(z_c, Q^2) D_{D/d}(z_d, Q^2) \quad (2.16)
\end{aligned}$$

where  $Y$  is the rapidity defined as :

$$Y = \frac{1}{2} \ln \left( \frac{E + P_\ell}{E - P_\ell} \right) \quad (2.17)$$

with  $E$  and  $P_\ell$ , the energy and longitudinal momentum component with respect to the beam axis of the parton-parton system. The quantity  $\eta$  is the outgoing hadron momentum imbalance. For hadrons produced back-to-back and with equal and opposite transverse momentum, the value of  $\eta$  is zero. This measurement can therefore provide direct information on the angular dependence of the parton-parton cross section.

As mentioned before, a complication in the interpretation of some of the measurements of high- $p_T$  scattering may be due to the contribution to

the transverse momentum from the internal motion of the partons within the colliding hadrons, ( $k_T$ ). This is thought to be an analogue of the Fermi motion of nucleons in a nucleus, and would result in a smearing out of the  $p_T$  spectrum. Other sources of smearing may originate from gluons emitted by the partons before the hard scattering in addition to the  $k_T$  associated with the fragmentation in the final state hadrons. To incorporate these  $k_T$  smearing effects in the calculations, it is assumed that a function of the intrinsic transverse momentum  $f(\vec{k}_T)$  can be factored from the longitudinal distribution functions. Therefore in Eq. (2.16) for example, the probability distribution for parton **a** is replaced such that:

$$dx_a G_{a/A}(x_a, Q^2) \rightarrow dx_a d^2k_{T_a} f(\vec{k}_{T_a}) G_{a/A}(x_a, Q^2)$$

$$\text{where } f(\vec{k}_{T_a}) = \frac{e^{-k_{T_a}^2 / \langle k_{T_a}^2 \rangle}}{\pi \langle k_{T_a}^2 \rangle} \text{ and the average intrinsic transverse}$$

momentum  $\langle k_T \rangle$  of the parton depends on  $R$ , the radius of the hadron, and should fulfill the uncertainty relation,

$$\langle k_T \rangle \cdot R > \hbar \quad .$$

In reality the  $\langle k_T \rangle$  of partons may include a dynamical part, and is estimated from the four jet structure of hard hadronic collisions.

The hard scattering process between two hadrons involves the interaction between the associated quarks and the production of scattered quarks fragment into final state hadrons whose properties can be measured. As was mentioned before, the fragmentation process produces

a number of particles that are formed in collinear groups called jets, that essentially follow the same direction as the original parton. In these hard collisions one expects large angle scattering and typically a four jet structure. There are usually two high- $p_T$  jets with roughly equal and opposite (back-to-back) transverse momenta,<sup>38</sup> plus two low- $p_T$  jets resulting from fragmentation of the rest of the beam and target partons. A small percentage of the events will result in a single leading high- $p_T$  hadron possessing a large fraction of the jet's transverse momentum, and therefore most of the momentum of the parent quark. It is viewed that this "leading particle" in fact may contain the original scattered quark as one of its constituent parts. Further formulation, a discussion of hadron scattering and the invariant cross section for inclusive two parton production is presented in Appendix A.

## **§2.5 Experimental Physics Overview**

A number of previous experiments have investigated hadronic production at high- $p_T$  in various energy ranges. These experiments include: the Fermilab E-454 collaboration, a dihadron production experiment at energies of 200 to 400 GeV; the CERN-Columbia-Oxford-Rockefeller Collaboration (CCOR group) at the CERN Intersecting Storage Ring (ISR), investigating the massive  $\pi^0 \pi^0$  production; the UA-1 and the UA-2 CERN proton anti-proton ( $\bar{p}p$ ) collider experiments; the Fermilab E-605 group hadron scattering experiment at an energy of 400 GeV; and the Fermilab CDF ( $\bar{p}p$ ) collider experiment.

The E-454 experiment collected data, using beryllium and tungsten targets, where two high- $p_T$  hadrons were produced in the proton-nucleon center-of-mass momentum system at an angle of approximately  $90^\circ$  to the beam axis.<sup>39</sup> This experiment utilized a two arm spectrometer to measure dihadron correlations at high- $p_T$ . They reported a strong correlation indicating that hadron pair production results primarily from the scattering of hadronic sub-constituents.<sup>40</sup> This experiment is similar to our E-711 experiment but at a much lower beam energy and lower luminosity.

Although unique in many ways E-711 shared some comparable features with experiment E-605 at Fermilab which studied the interaction of 400 GeV/c protons with Beryllium, Copper, and Tungsten, observing hadrons produced at high- $p_T$ . The data covered a region from 5.2 to 8.0 GeV/c in transverse momentum and  $73^\circ$  to  $102^\circ$  in  $\theta$ .<sup>41</sup> They report a hadronic production cross section dependence on  $p_T$ , and an inclusive hadronic production cross section dependence on production angle.<sup>42</sup> The E-605 results use a single particle high- $p_T$  trigger and therefore could not fully measure the quark-quark scattering amplitudes, due to Fermi motion, and the absence of information on the recoil kinematics, etc. In the experiment E-711, we used a symmetric trigger (explained in a later section), and therefore could extend the measurements of the quark-quark scattering amplitudes. Also E-711 was designed to go beyond the acceptance range of the E-605 detector ( $|\cos \theta^*| < 0.25$ ) and improve the momentum resolution, while collecting the data at 800 GeV beam energy.<sup>43</sup> E-711 was unique in that the experiment was able to collect data



data on different charge states ( $++$ ,  $--$ ,  $+-$ ) and the experiment was designed to decouple the trigger on high- $p_T$  particles from the reconstruction of the track momenta, by triggering on the particle in the vertical plane and bending only in the horizontal plane.

The CERN UA-1<sup>44</sup> and UA-2<sup>45</sup> collaborations using the ( $\bar{p}p$ ) collider, reported results on the angular distributions of parton-parton scattering averaged over all contributing subprocesses at  $\sqrt{s} = 546$  GeV and  $\sqrt{s} = 630$  GeV. Here the  $\theta^*$  scattering angle is the angle between the di-jet axis and the hadron-hadron axis. The data from both experimental groups is shown in Figure 2.5<sup>46</sup>, along with a prediction to the data from a QCD calculation using a leading logarithm approximation evaluated at a scale  $Q^2 = p_T^2$ . The Monte Carlo calculation uses the Duke-Owens Set 1 distribution functions.<sup>47</sup> This theoretical result is consistent with the di-jet data, and a similar theoretical comparison will be utilized for our present data at  $\sqrt{s} = 38.77$  GeV.

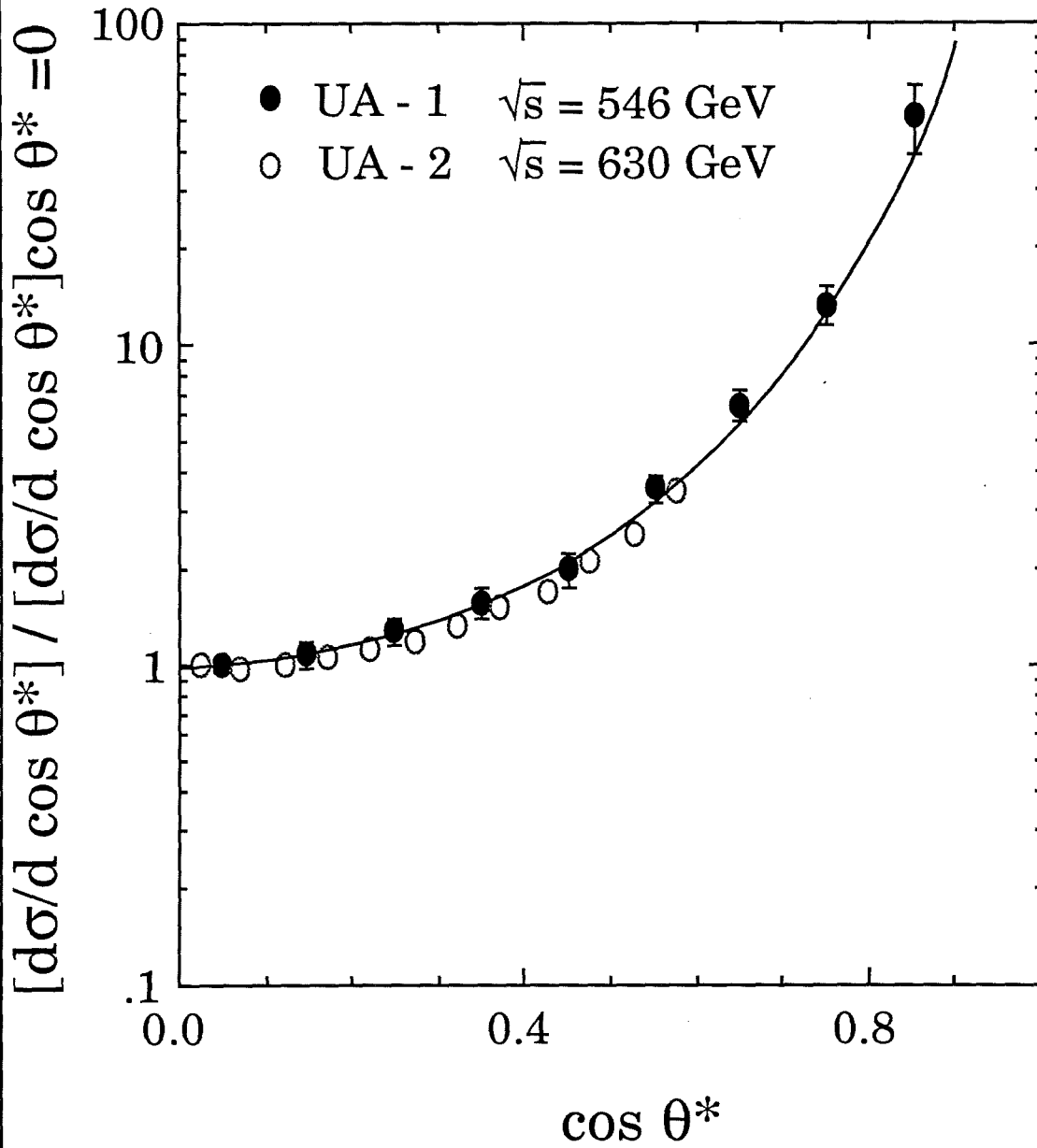


FIGURE 2.5

Angular distributions in  $\bar{p} p$  collisions for the UA -1 and the UA -2 Experiments with a QCD prediction to the data

Ref: 46

The CCOR collaboration at the CERN ISR, collected data in a center-of-mass energy region similar to this experiment. The ISR measurement on massive dihadrons consists of  $\pi^0 \pi^0 \pm X$  data collected with lead glass arrays.<sup>48</sup> The polar angle  $\theta^*$  was defined to be the angle of the dihadron axis with the axis of the beam, in the frame where the dihadron system has no net longitudinal momentum, transforming only along the beam axis in the p-p center-of-mass frame. They measured the angular dependence of the hard scattering subprocess at fixed mass with  $|\cos \theta^*|$  in the angular region between 0 and 0.5, and in the mass range of 8 to 16 GeV. The data indicates that the leading particle carries most of the momentum due to the scattered partons, and the angular distribution is found to be independent of the mass of the di-pion system and the proton-proton collision energy. In comparison to CCOR, we have attempted to increase the acceptance and exploit the higher luminosity available with our fixed target experiment.

The analysis reported by CCOR uses the leading  $\pi^0$  as the direction of the parton (jet) and fits the  $\cos \theta^*$  dependence to the form:

$$\frac{d^2\sigma}{dM d\cos \theta^*} = \frac{1}{2} N_A \left[ \frac{1}{(1 + \cos \theta^*)^a} + \frac{1}{(1 - \cos \theta^*)^a} \right], \quad (2.18)$$

where the parameter  $a$  was found to be  $2.97 \pm 0.05$ <sup>49</sup>. This fitting form will also be utilized for comparison to the present data which is based on the charged final state instead of the neutral dihadrons. Figure 2.6<sup>50</sup> presents

presents data from the CCOR group at  $\sqrt{s} = 62.4$  GeV and in two different mass bins. The curves shown in this figure come from a QCD calculation cited in the reference.

The di-jet angular distribution from the  $(\bar{p}p)$  collisions at center of mass energy  $\sqrt{s} = 1.8$  TeV, from the Fermilab CDF collaboration is shown in Figure 2.7.<sup>51</sup> They report favourable agreement with QCD predictions, with the definition of the momentum transfer,  $Q^2$ , varying in a range from  $4 p_T^2$  to  $p_T^2 / 4$ . The present analysis uses a value of  $Q^2 = p_T^2$ .

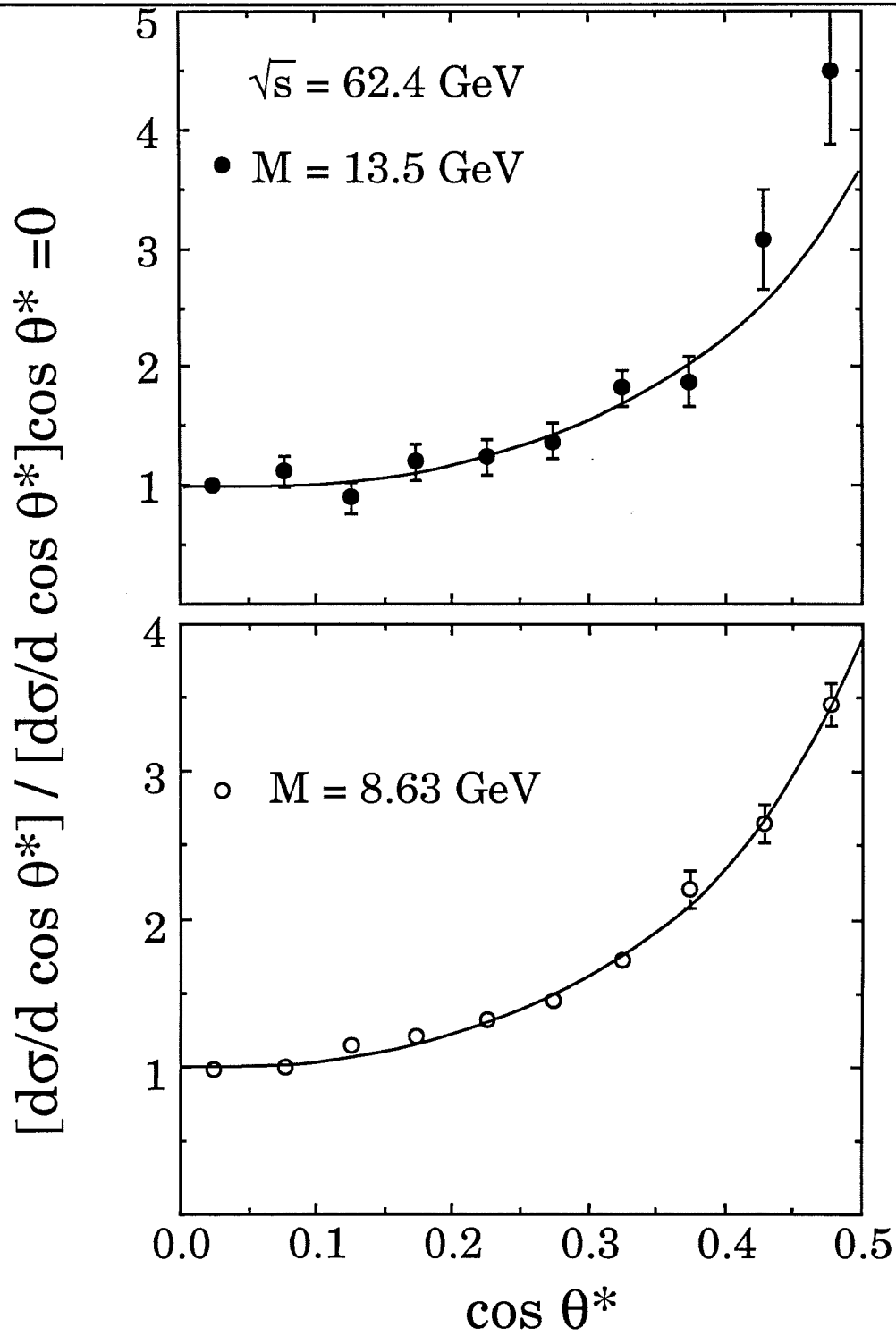


FIGURE 2.6

Angular distributions for  $\pi^0 \pi^0$  production from the CCOR Experiment with QCD predictions to the data

Ref: 50

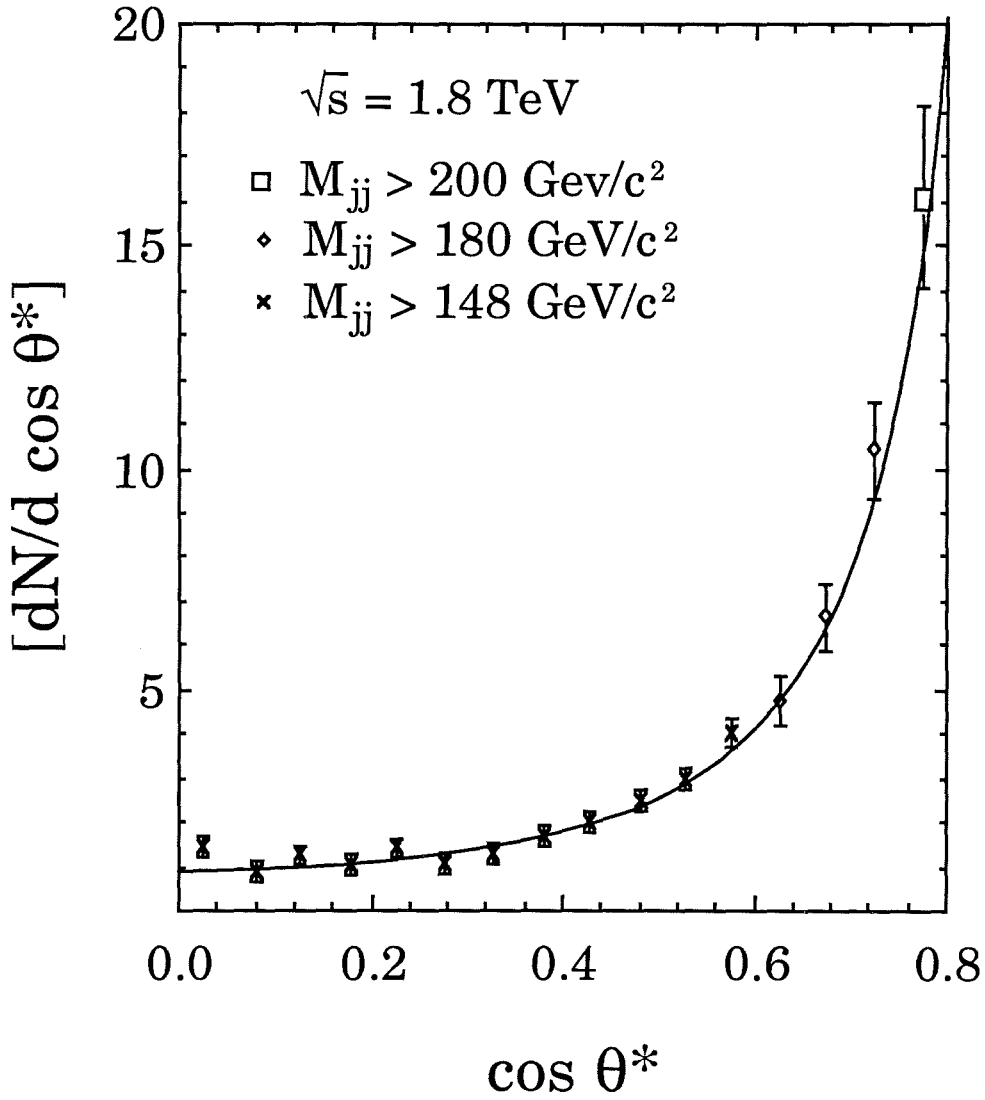


FIGURE 2.7

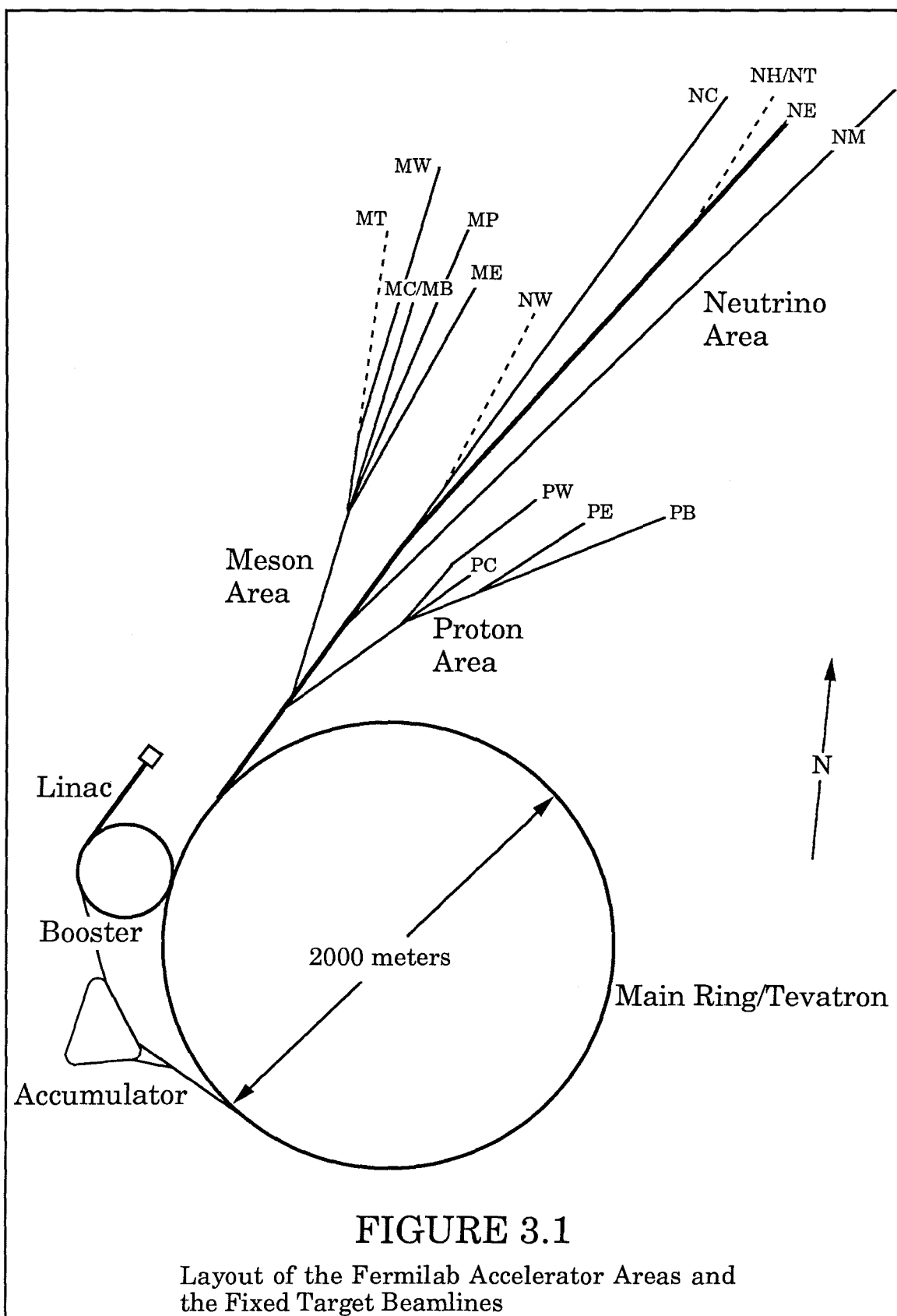
Dijet angular distributions in  $\bar{p}p$  collisions  
for the CDF Detector Experiment with  
QCD predictions to the data

## CHAPTER 3

### THE PROTON BEAM SYSTEM

#### **§3.1 The Accelerator System**

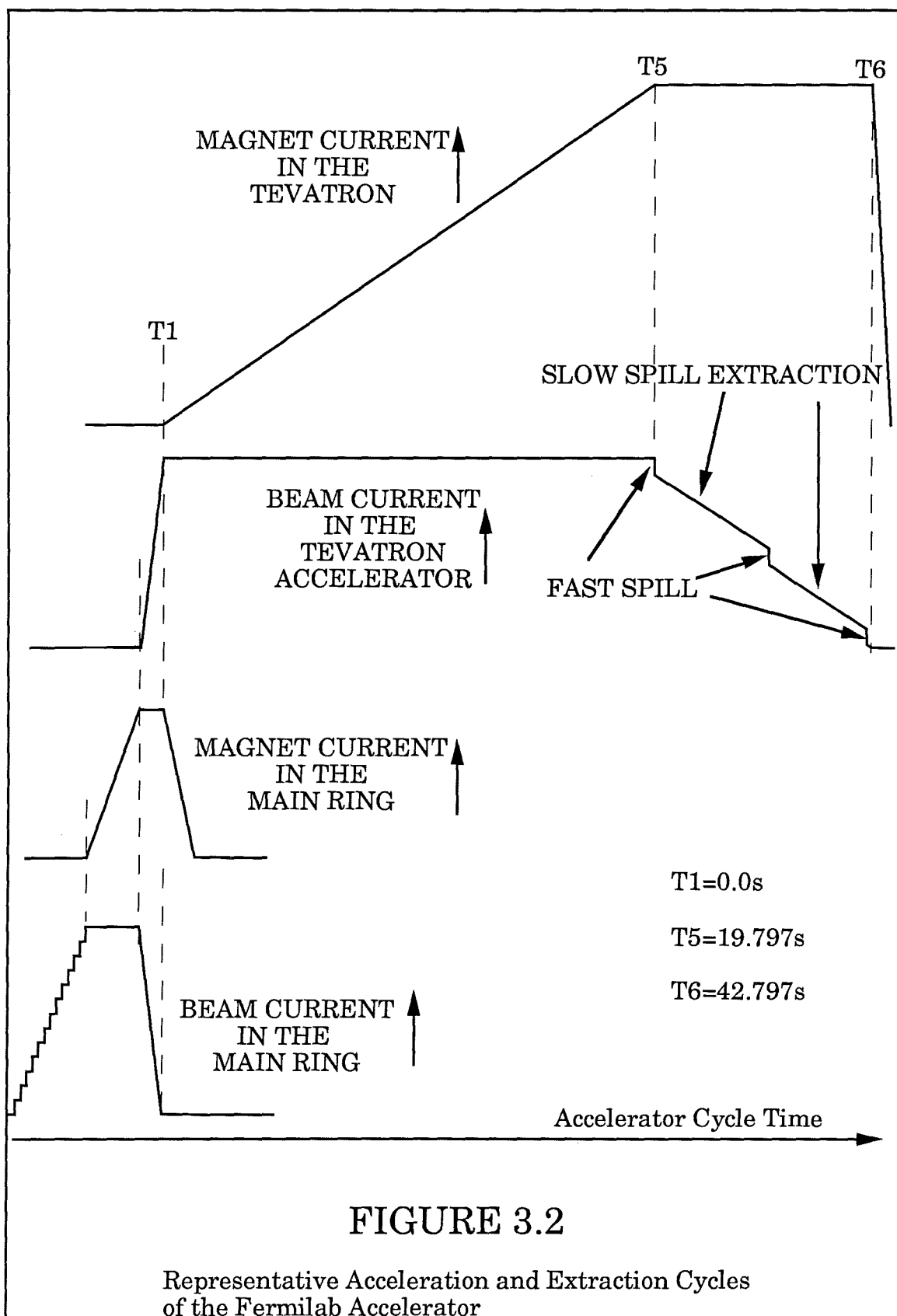
High energy protons for this experiment were produced by the clustered accelerator system of the Fermi National Accelerator Laboratory. This system consist of five different acceleration stages facilitated by five different accelerators. The protons are initially produced from hydrogen gas as the ion source and accelerated to an energy of 750 KeV (kilo electron volts) by a Cockcroft - Walton electrostatic generator. This process produces a beam of particles that are injected into a connecting linear machine known as a Linac or linear accelerator, which directs the particles along its length through drift tubes separated by accelerating gaps. Exiting this machine the beam has attained an energy of 200 MeV concluding the linear acceleration cycle. The next three stages all produce energy gain through cyclic acceleration. An overview of part of the Fermilab accelerator area is shown in Figure 3.1 with our experiment in the NE beamline.





The beam path is confined to a circular geometry with a fixed region for acceleration, which gives the particles a nearly uniform increase in energy each time they pass repeatedly through the electric field in this region. The smaller ring is the 8 GeV synchrotron called the Booster, which provides particles for the Main Ring synchrotron. Although the Main Ring has a capability of accelerating protons to 512 GeV using conventional iron core magnets, the typical operating energy is 150 GeV, the energy that is used for injection into the final stage of particle acceleration, which is the string of superconducting magnets which makes up the Tevatron accelerator. The Tevatron machine was designed to extract a beam of protons at an energy of 1000 GeV, but for this experiment the protons were accelerated to the nominal operating energy of 800 GeV.

Most fixed target experiments are, in general, insensitive to the initial stages of acceleration of the proton beam. This experiment required a large particle flux, with severe constraints on the beam shape at the experimental target. Because of the high interaction rate some attention was therefore given to the time structure of the accelerated beam. Representative acceleration and extraction cycles are shown in Figure 3.2, with times indicated with respect to the accelerator reference time T1. The Booster is matched to the Main Ring synchrotron at 1/13th its size and therefore produces 13 booster batches for the Main Ring as shown by the 13 steps shown in the lower portion of Figure 3.2.



As the particles pass through the radiofrequency accelerating cavities of both the Main Ring and the Tevatron cycles, they tend to bunch up into what are called "buckets", which are about 18 nanoseconds apart, and about 2 nanoseconds in duration. A number of protons are in each bucket, and the uniformity of this distribution determines the beam intensity per unit time and is important because of the high rate of this experiment. During the slow extraction times (between T5 and T6), this beam structure was monitored by the experiment over the full 20 seconds of the beam spill. Protons in the Tevatron were accelerated to an operational momentum of 800 GeV/c, with a maximum intensity of  $2 \times 10^{13}$  protons per pulse and a 60 sec repetition rate. Some other modes of extraction often produce large fluxes of particles in much shorter extraction times (called fast spills). During part of our experimental operations, fast spill was produced at the beginning, the middle, and the end of the acceleration extraction cycles. Any overlap of these extraction modes with the slow spill for this experiment can cause the instantaneous rate of the beam interactions to be prohibitively high and possibly damage some components of the E711 detector. An adjustment in the timing cycles for the magnet current in the transport system results in aborting the fast spill beam to the NE line and transporting the slow spill. This technique was effective in segregating the two spill structures.

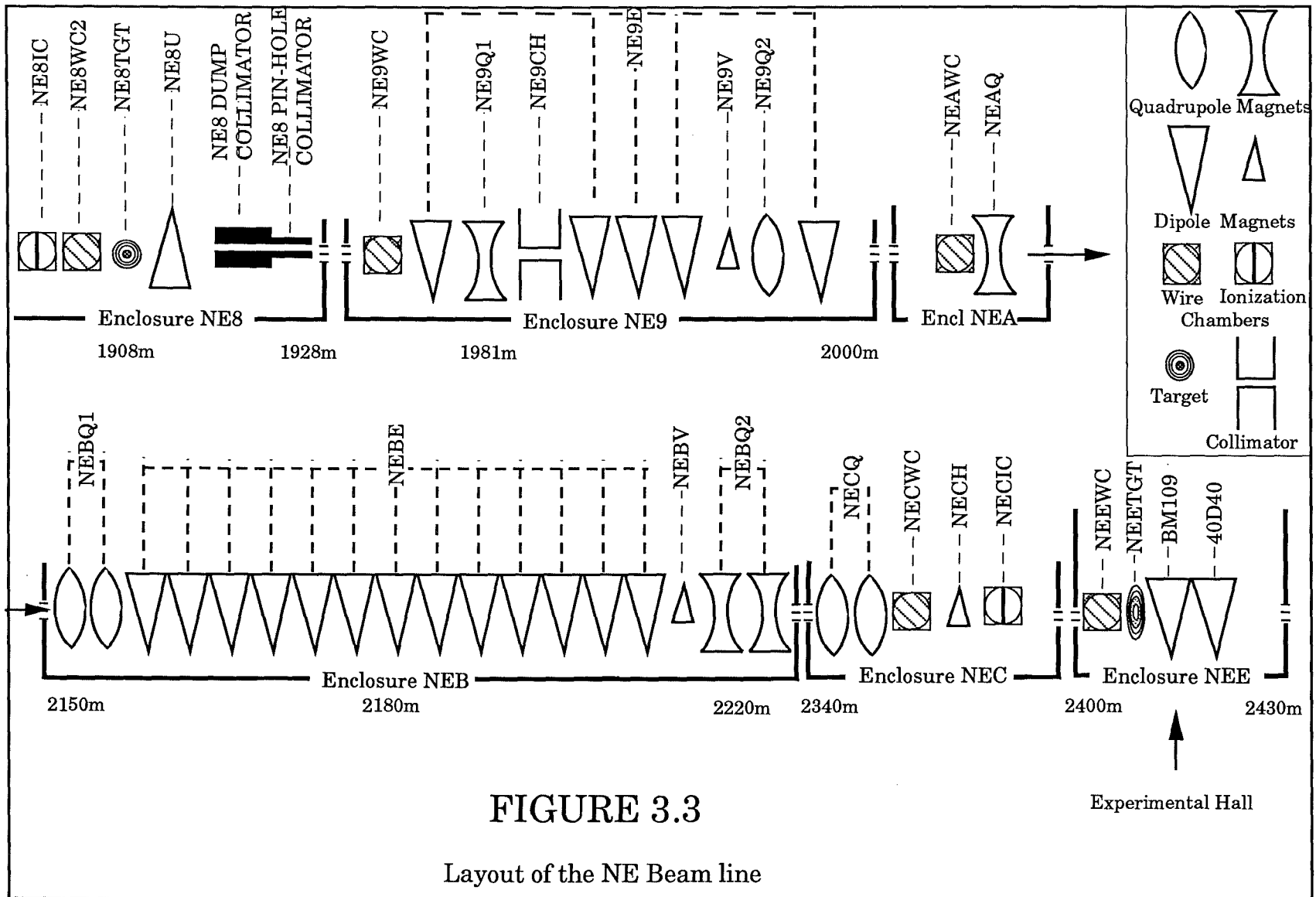
### **§3.2 The Neutrino East Beamline**

The three primary areas for particle beam extraction from the Fermilab accelerator are the Proton, Meson, and Neutrino Areas for fixed target experiments. This experiment was operated within the Neutrino East Beamline (NE). In addition to secondary beams, this beamline also supports primary protons from the accelerator. The general properties of NE include a maximum proton momentum of 900 GeV/c, with a momentum dispersion ( $\pm\Delta p/p$ ) of 3.3% and a maximum flux of  $5 \times 10^7$  protons per second per  $10^{12}$  protons extracted from the accelerator.<sup>52</sup>

High energy charged particle beams are created and controlled by implementing two beam handling constraints, namely, restricting the path of the beam to an electromagnetic channel; and confinement of the beam within a geometric channel. By using strings of magnets that have different field shapes, the particle beam can be deflected in one plane (by a bending magnet or dipole), or focused and defocused in more than one plane (by multipole magnets with alternating polarity). Since the particles might interact with whatever material it encounters, the geometric channel can in general be defined by: an evacuated beam tube (to reduce the interactions with air); beam collimators (with opening gaps defined by materials that will effectively absorb the particles they encounter); and the aperture of the magnets in the beamline.

The design and operating conditions expected of the NE beamline were determined by the particle intensity and targeting requirements of the E711 experiment. The horizontal width of the targets restricted the

horizontal extent of the beam design to be about 1 mm at the E711 target station to match the width of the target in the analyzing magnet bend direction. This constraint provided, as close as feasible, a point origin in one dimension for the interaction vertex in each event. The importance of these thin target and beam size constraints was to maximize the rate capability and eliminate the need for instrumentation for tracking particle trajectories upstream of the analysis magnets. The capability of localizing the interaction point and of performing the experiment at high luminosity gives the fixed target experiment a unique and distinct advantage over colliding beams experiments, in this one aspect. The beam for E711 was produced, using the existing beam handling devices already operating in NE. Figure 3.3<sup>53</sup> shows the elements in the beamline from the NE8 upstream enclosure to the E711 experimental hall.



The computer program TRANSPORT<sup>54</sup>, was used to determine the ideal magnetic field strengths and field orientations needed to produce the desired beam. This program uses matrices to represent drift spaces and magnets, and uses vectors to represent individual particle rays. The displacement components of the vectors describe the solution to the equations of motion at a point along the path of the particle. A particle of mass  $m$  and charge  $q$  with momentum  $\mathbf{p}$  is subject to a Lorentz force  $\mathbf{F} = q\mathbf{v} \times \mathbf{B}$  in the region of a magnetic field  $\mathbf{B}$ , where unagitated, the particle will tend to move along a circular path. The equations of motion in the  $x$  (horizontal) and  $y$  (vertical) directions, for a particle subject to a Lorentz force, can be written as :

$$\frac{d^2x}{dz^2} + \frac{q}{p} B_y = 0 \quad ; \quad \frac{d^2y}{dz^2} - \frac{q}{p} B_x = 0 \quad \text{where} \quad v \equiv \frac{dz}{dt} = \text{constant} \quad (3.1)$$

Therefore, in an ideal horizontal bending field (no fringe field effects), the solution to the equations as a function of time and thus the resultant displacement is given by:

$$\begin{aligned} x &= r \cos\left(\frac{qB}{m} t\right) \\ z &= r \sin\left(\frac{qB}{m} t\right) \end{aligned} \quad (3.2)$$

where  $r$  represents the radius of circular curvature. Equations for ideal vertical bending fields give similar results.

Deviations from the ideal horizontal and vertical planes can also occur. Charged particle coulombic interactions, or collectively, space

charge effects within the beam, as well as magnetic fringe field effects , will tend to cause the beam particles to diverge from their central path, or ideal orbit. However a typical quadrupole field, which has a gradient such that the field vanishes along the central axis, will focus a beam in one plane and simultaneously defocus in the other plane, effectively controlling the beam's angular divergence.

Thus the TRANSPORT program combines the particle displacements ( $x$  and  $y$ ) and angular divergences ( $x'$  and  $y'$ ), in two planes; the fractional deviation of the momentum of the particle ray from the central trajectory design momentum of the system, known as the momentum dispersion ( $\Delta p/p$ ); and the longitudinal displacement ( $z$ ) along the beam direction (i.e. the path length difference between the particle ray and the central ray trajectory), to give a description of the maximum and minimum extents of the beam (in both horizontal and vertical beam profiles). These variables make up a six component ray vector with respect to the reference trajectory, i. e.:

$$\begin{bmatrix} x \\ x' \\ y \\ y' \\ z \\ \frac{\Delta p}{p} \end{bmatrix} \quad (3.3)$$

Using the ray vectors, (which describe the beam particle's characteristics at a point), in conjunction with the transfer matrices, (which can describe drift spaces as well as dipole and quadrupole magnets), allows one to predict the beam profiles at other points, by solving six simultaneous



linear equations for a static magnetic system. A simple example would be the drift of a particle along the beamline from  $z_0$  to  $z$ . The ray vector at the new point  $z$  would be given by:

$$\begin{bmatrix} 1 & L & 0 & 0 & 0 & 0 \\ 0 & 1 & 0 & 0 & 0 & 0 \\ 0 & 0 & 1 & L & 0 & 0 \\ 0 & 0 & 0 & 1 & 0 & 0 \\ 0 & 0 & 0 & 0 & 1 + \frac{L}{z_0} & 0 \\ 0 & 0 & 0 & 0 & 0 & 1 \end{bmatrix} \begin{bmatrix} x_0 \\ x' \\ y_0 \\ y' \\ z_0 \\ \frac{\Delta p}{p} \end{bmatrix} = \begin{bmatrix} x \\ x' \\ y \\ y' \\ z \\ \frac{\Delta p}{p} \end{bmatrix}$$

$$\text{where } x = x_0 + x' * L \quad ; \quad y = y_0 + y' * L \quad ; \quad z = z_0 + L \quad (3.4)$$

Changes in the beam profile due to magnetic forces can be similarly calculated.

Figure 3.4 shows the Monte Carlo TRANSPORT results for the beam profile in the NE beamline. In Figure 3.4a, the profiles are given for the  $x$  and  $y$  extent of the beam, from the NE8 enclosure where the beam defining pinhole collimator is located, to the downstream end of the NEE enclosure beyond the E711 target station. The collimator had an opening gap of nearly  $6.25 \text{ mm}^2$ . The regions on the graph at which the beam sizes radically change is caused by quadrupole magnets modifying the beam divergence at those points. Figure 3.4b shows details of the predicted horizontal focus at the target.

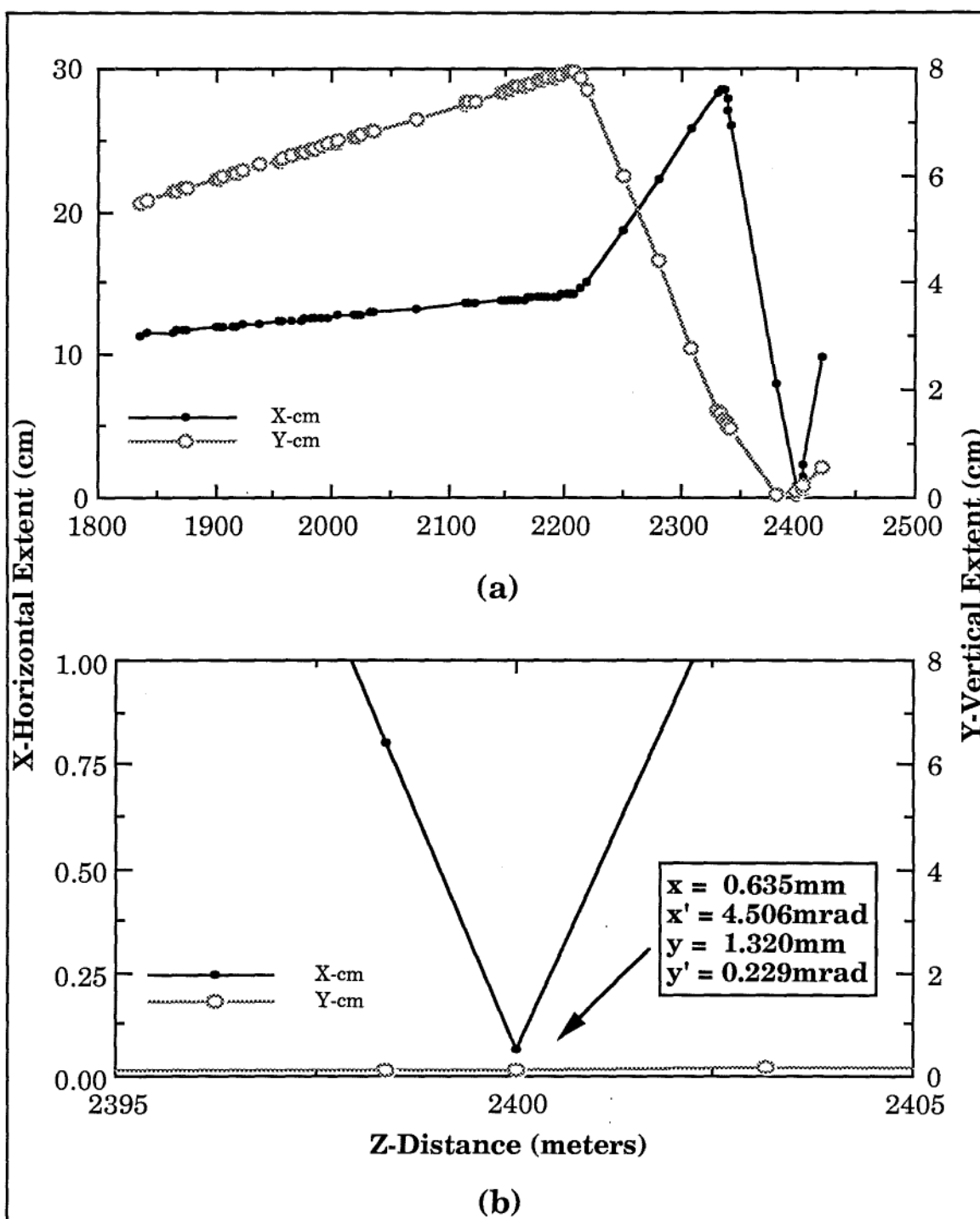


FIGURE 3.4

Beam Envelope for the NE Beam Design  
Monte Carlo Results

### **§3.3 The Beam Monitoring System**

The monitoring of characteristics of the proton beam and control of the beam was accomplished using various beamline devices. Qualitative characteristics of the beam divergence as well as beam positioning at various locations were determined from profiles generated by segmented wire ionization chambers (SWIC). Each chamber has horizontal and vertical wire planes that produced digitized signals proportional to the beam intensity encountered by each of the 128 wires in a plane. The wires had a 1.0 mm spacing, and the signals produced corresponded to profiles of the horizontal and vertical widths of the beam.

#### **§3.3.1 Proton Beam Intensity**

The total intensity of the proton beam per beam spill was measured with a calibrated ionization chamber (NECIC), and the calibration of this chamber is shown in Figure 3.5. The ionization chamber was used since the scintillation counters could not operate at the large flux rate of the experiment. The calibration data was taken at low beam intensities (less than  $20 \times 10^6$  protons/ beam pulse) and correlated with two overlapping, 3 inch by 4 inch (7.62 x 10.16 cm) scintillation counters (located in the beamline at the entrance to the experimental hall) and beam intensity values from the secondary emission monitors provided by the accelerator instrumentation. Each digitized count of NECIC represented a measured value of two pico-coulombs of collected charge, with a pedestal value (when the beam is not transmitted), of 137 counts.

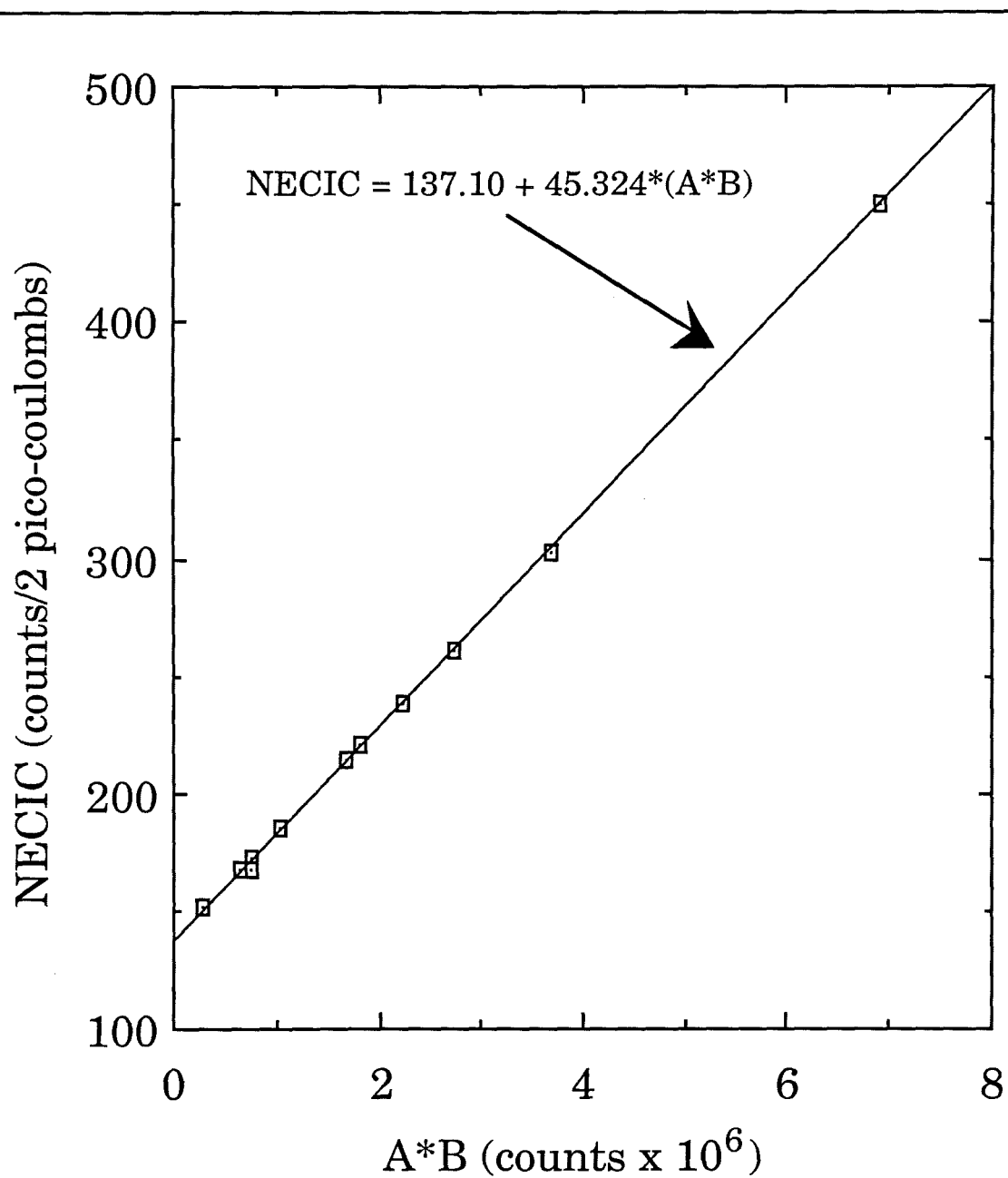


FIGURE 3.5

Calibration of the NECIC ionization chamber with respect to scintillation counters at low beam intensity

So the number of protons could be determined from a line fit to the data of Figure 3.5, and is presented as follows:

$$\text{Flux (protons)} = (\text{NECIC} - 137) * 22 \times 10^3 \quad (3.5)$$

The chamber was positioned so that it intercepted all of the beam, and was located between the last magnetic elements and the experimental target so that the beam measured by the ionization chamber was not deflected before hitting the target. At the low beam intensities the ionization chamber was calibrated to an accuracy above 98 % .

### §3.3.2 Proton Beam Control

The control on the crucial horizontal beam position at the NEE target was provided by a secondary (vernier) dipole magnet (NECH) located in the NEC enclosure nearly 60 meters upstream of the target. This magnet was used to maximize and maintain the intensity of the beam on the target. The position of the beam for maximum luminosity was ensured by frequently scanning the beam across the target. The NECH dipole was calibrated using the NEEWC SWIC located 2 meters upstream of the experimental target. Some statistical data, such as a reading of the position of the peak of the horizontal beam profile were ascertained from the electronics used to operate the SWIC. The calibration of this dipole in units of amps per millimeter with respect to beam positioning is shown in Figure 3.6.

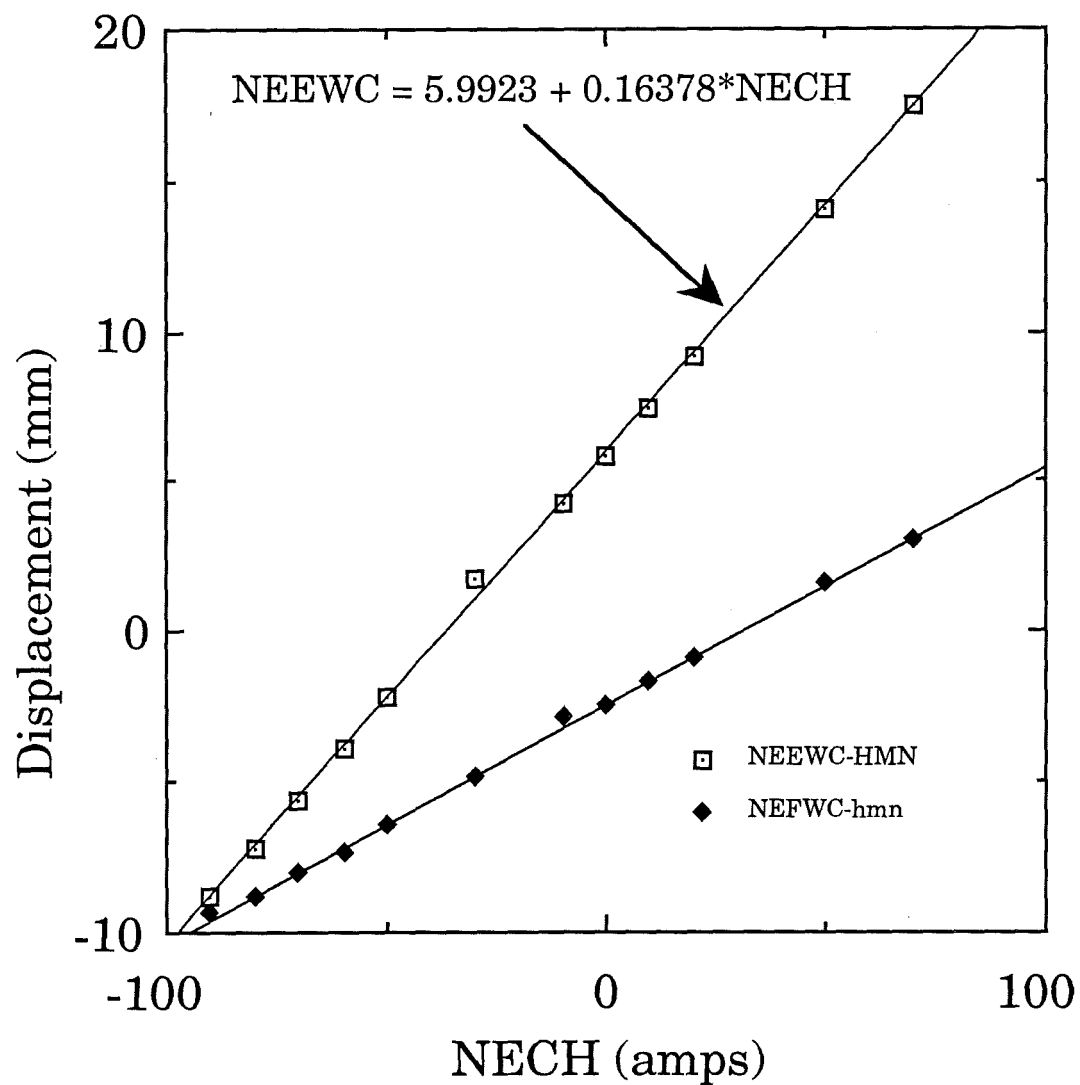


FIGURE 3.6

Calibration of the NECH dipole magnet  
with respect to the 1mm wire spacing  
of the NEEWC wire chamber : 6.29 amps/mm.  
Position data at NEFWE is also shown

The calibration is 6.29 amps/mm which takes into account the distance from the target to the NEEWC device. The beam displacement was also recorded on a SWIC (NEFWC) in the next experimental hall. This data is also shown indicating a smaller slope due to the additional deflection produced by the constant magnetic field of the spectrometer magnets located immediately downstream of the target .

The particles were focused on the target using the combination of quadrupole magnets found in the NEB and the NEC enclosures. Determining the best focus, and therefore the maximum intensity of the beam at the target was accomplished by adjusting the focus of the beam using the quadrupoles, sweeping the beam horizontally across the target ("target scans") and maximizing the ratio of the radiation scattered by the target at nearly 90 degrees with respect to the beam direction, to the total beam intensity measured by the ionization chamber. Although a few detail target scans (one luminosity measurement per beam pulse), were completed and written to the data tapes, the target scans mentioned here were usually done within the time of two or three accelerator pulses (flat top extraction cycles of 40 – 60 seconds), and were important for establishing the initial targeting, as well as maintaining that maximum targeting. Determination of the luminosity of the experiment will be discussed in a later chapter. Horizontal and vertical target scans are shown in Figures 3.7 and 3.8 respectively.

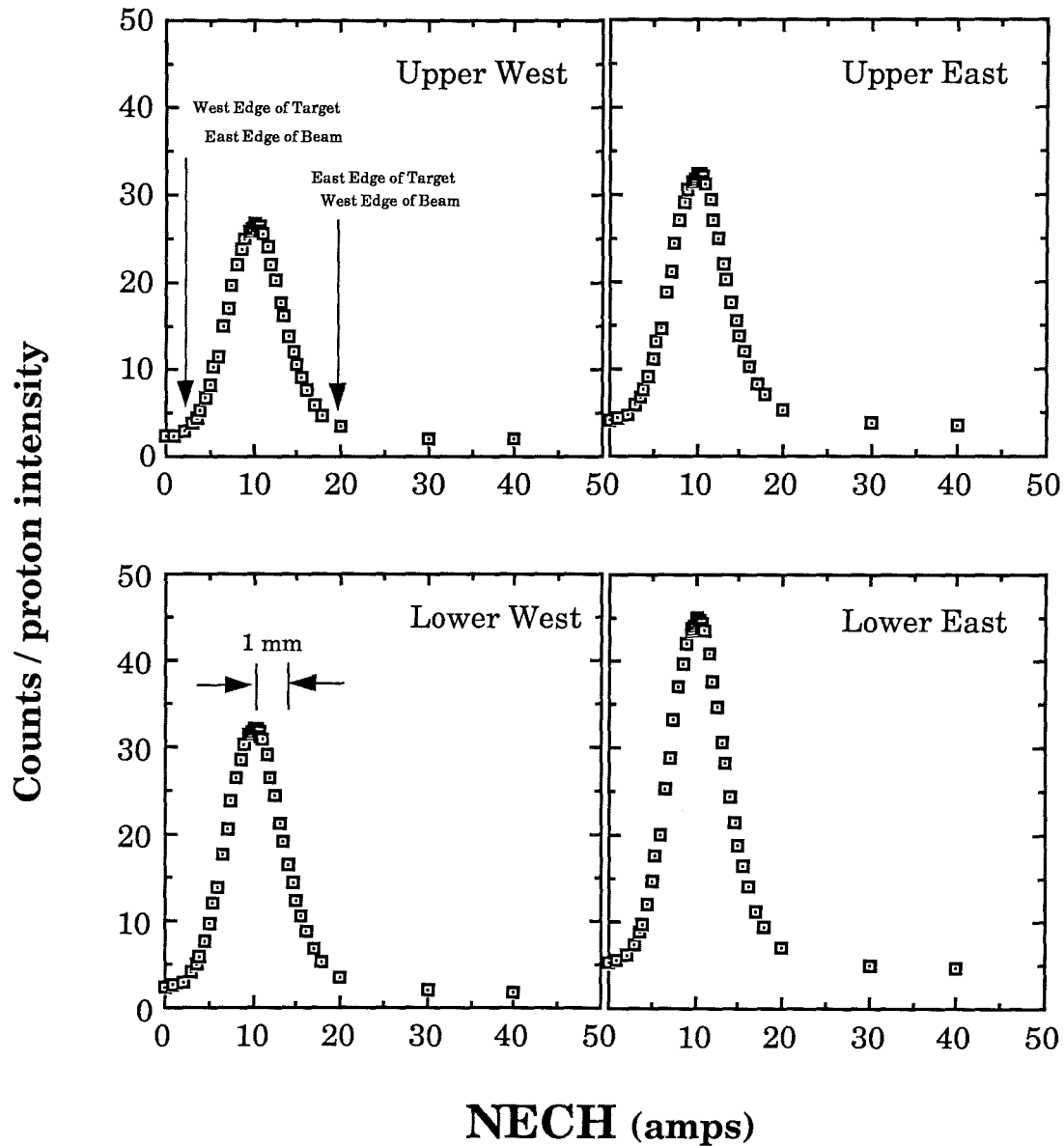


FIGURE 3.7

Target Scan Profiles from the Four Luminosity Stations using the NECH dipole for horizontal beam deflections calibrated at 6.29 amps/mm. For these beam scans the horizontal beam size is approximately the target size.



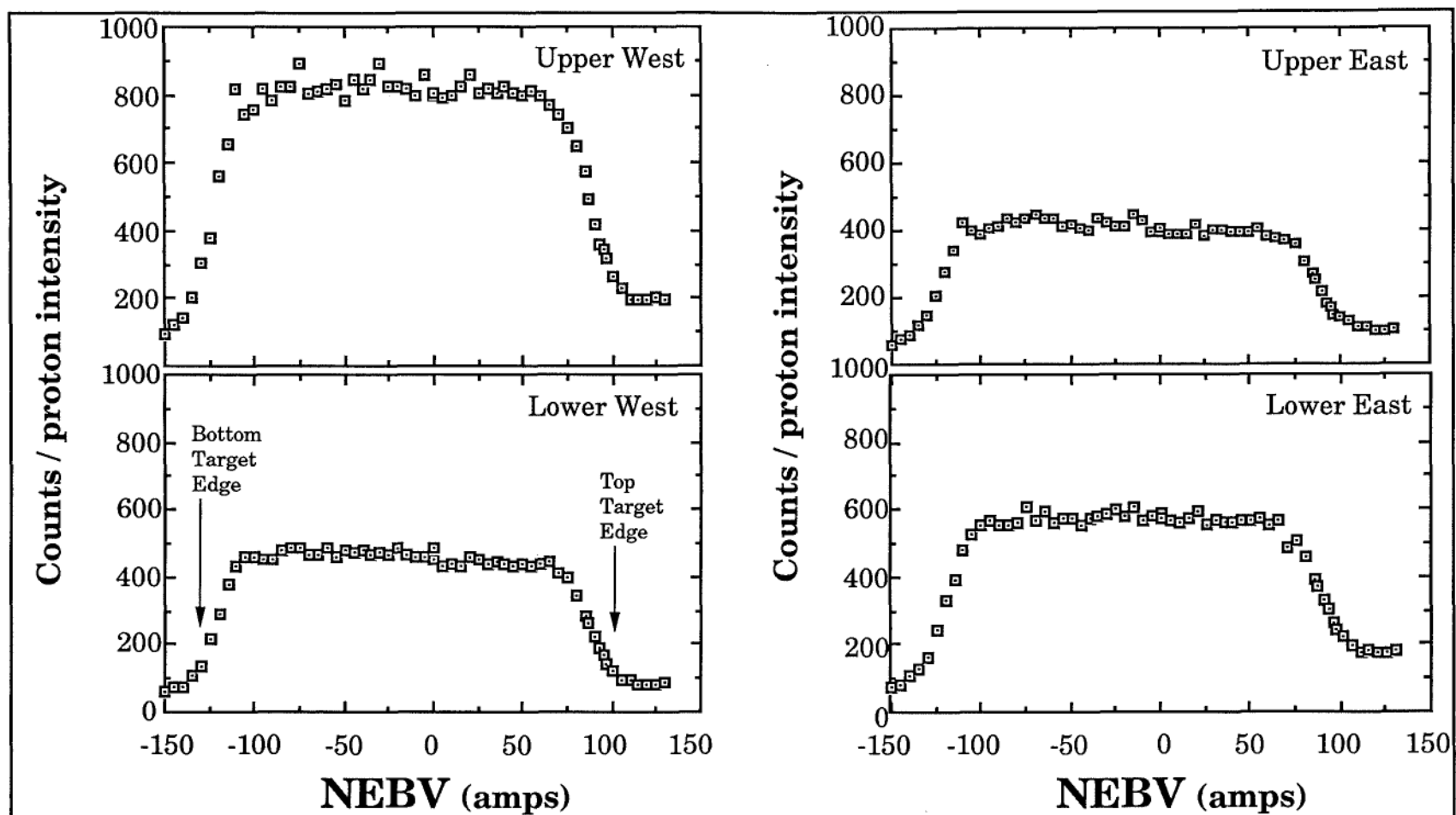


FIGURE 3.8

Target Scan Profiles from the Four Luminosity Stations using the NEBV dipole for vertical beam deflections at the target

The labels Upper West etc., correspond to the location of the luminosity counters in the laboratory, where upper is above the beamline and west is west of the beamline. A similar explanation can be assumed for the other names. The vertical scales for Figures 3.7 and 3.8 differ because the beam focus was different for the two separate scans. In the horizontal scans the flat region of the distribution at the higher magnet currents indicates where the beam misses the target to the east. This also presents a location where interactions due to upstream materials could be measured. Likewise for the vertical scans, a flat region at higher positive currents indicates the beam position near the top of the target. Since the target was held vertically, the lower part of this distribution was not as flat due to beam interactions with the target holder. Details of the target apparatus will also be presented in the next chapter. Calculations that determine the beam horizontal size (0.93 mm) from Figure 3.7 and verify a vertical target size (5.715 cm) from Figure 3.8 are given in Appendix B.

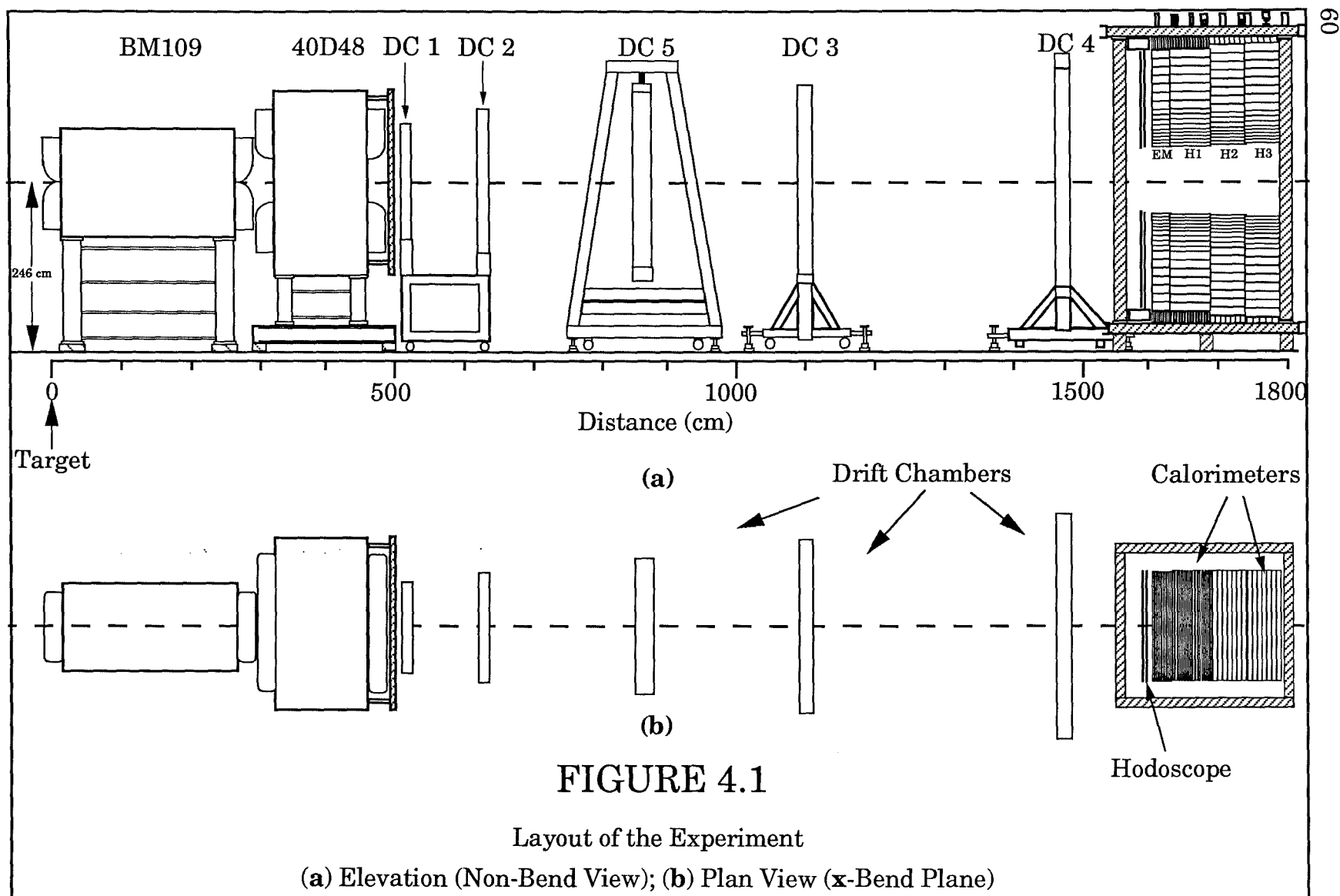
## CHAPTER 4

### THE EXPERIMENTAL APPARATUS

#### §4.1 Introduction

The technical requirements of this experiment demanded a spectrometer system that would provide data sufficient to determine the angular dependence, charge dependence, and atomic weight dependence of massive hadron pairs produced in the collisions of 800 GeV protons with nuclear targets. The detector was designed within specific limits to incorporate features that included a large angular acceptance, a high interaction rate capability and high momentum resolution.

The experiment used an open geometry, double arm spectrometer which is shown in Figure 4.1. The laboratory reference frame is defined by the  $z$  axis pointing along the proton beam direction (north), with the positive  $y$  axis pointing up in the vertical direction, and the positive  $x$  axis pointing west with respect to the beam direction, all consistent with a right handed coordinate system.



The detector consisted of a removable target station which used four different targets alternately, each of which were about 10% interaction length each, of aluminum, beryllium, iron, and tungsten. With proper beam focusing on the 1mm thin targets in the x direction, described in Chapter 3, vertex reconstruction in the horizontal plane was not necessary. This focusing scheme was critical, as particle tracking upstream of the magnet was not possible due to the high intensity rate. This also reduced material in the beam which would increase the background radiation. The beam targeting position and the fraction of the beam hitting the target were measured by the luminosity monitoring system. The system consisted of four sets of triple coincidence counters which were placed in a plane nearly 90 degrees to the beam line, symmetrically surrounding the target and mounted just upstream of the analyzing magnets. These two momentum analyzing magnets provided a charged particle deflection in the horizontal plane weakly coupled to the transverse momentum components of the hadron pair.

Five stations of multiwire drift chambers were placed between the magnets, and the hodoscope planes and calorimeters for particle tracking. Because of the small and steeply falling cross section with increasing mass in the production of di-hadrons, the experiment ran at a high interaction rate ( $\approx 2.5 \times 10^6$  interaction/sec). To accommodate this high rate, the calorimeter system was divided into two vertically separated arms, leaving a gap around the beam axis as a zone where low momentum transfer charged particles avoided the active region of the detector. In addition, low momentum charged particles were horizontally

deflected out by the magnetic field. The central region of the wire chambers corresponding to the region between the calorimeters, was also desensitized to allow for the large particle flux along the beam axis. The four hodoscope planes along with the two sampling calorimeters (i.e. the electromagnetic and the hadronic) were used to generate a real time event selection signal, which was the trigger for the experiment.

#### **§4.2 The Targeting System**

The target station was located at the entrance gap immediately upstream of the first analysis magnet. A diagram of the system is shown in Figure 4.2 . The station consisted of an aluminum staff holder attached to a servo-plate on a linear translation stage, which could be adjusted by a built in vernier caliper. The base plate was mounted on a level shelf attached to the front face of the upstream analysis magnet. The target was placed in a slot at the top of an acrylic staff and held in place with a plastic ring.

The horizontal position of the target and its alignment to the beam axis were determined by an alignment fixture. The fixture consisted of an aluminum tube  $\approx 2.54$  cm in diameter, which was affixed to the upstream face of the first magnet, and could slide into the beam region horizontally at the correct height. The end surface of the tube was machined flat and optically surveyed to be aligned with the beam axis. When fully extended horizontally, this surface would determine the position of the target and align the edge of the target toward the oncoming beam.

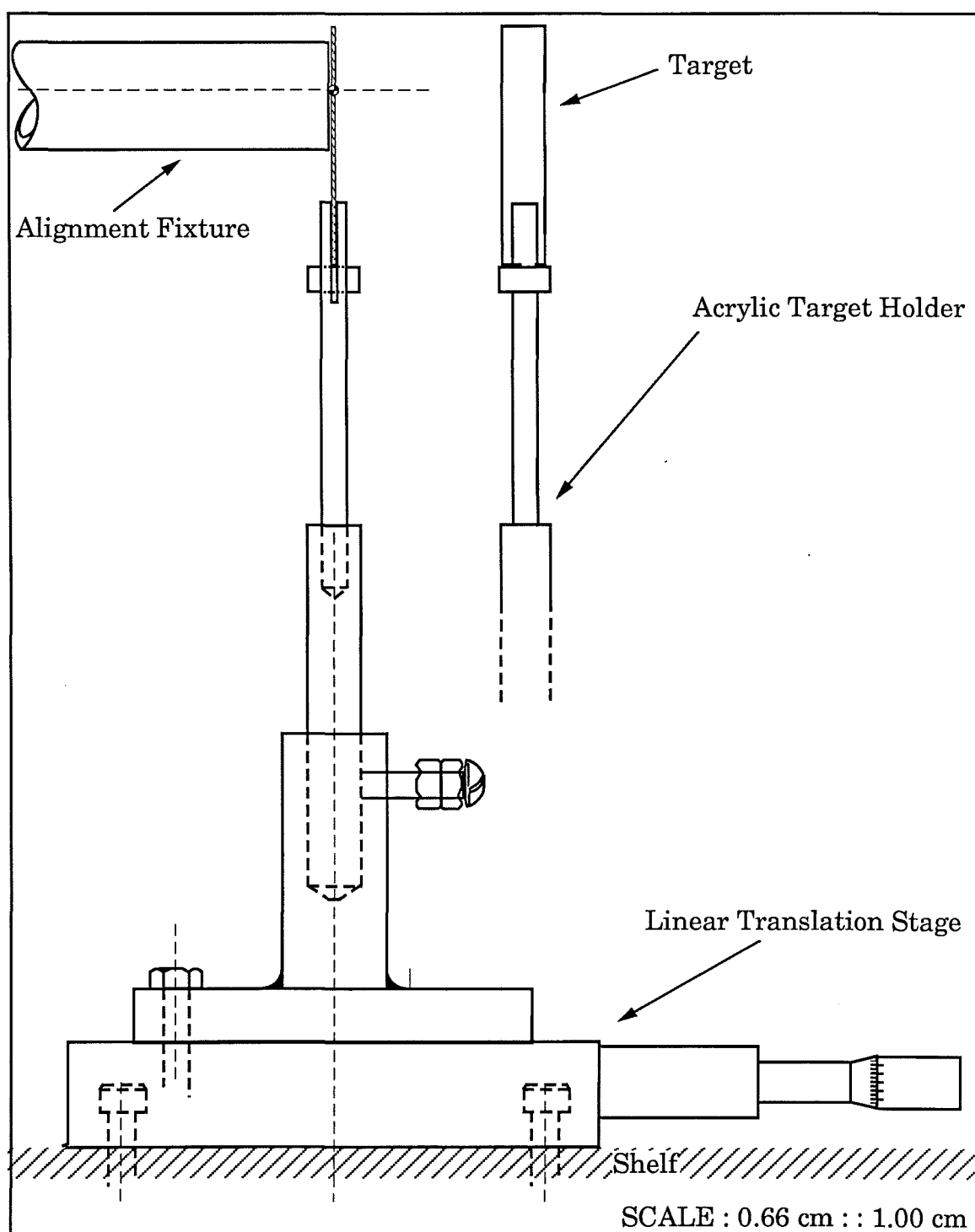


FIGURE 4.2

The E-711 Target Station looking downstream along the beam axis.

Data were taken using four different targets, whose characteristics are presented in Table 4.1. It should be noted that the z dimension was constrained to be a 10% interaction length for each target, and (with the exception of the iron target), the x dimension was fabricated as close to 1mm as possible.

Table 4.1

**Technical Information on the Experimental Targets**

Target Material	Atomic Weight	Dimensions			% Interaction Length
		x (cm)	y (cm)	z (cm)	
Beryllium	9.01	0.10225	5.715	4.066	9.99
Aluminum	26.98	0.08357	5.715	3.951	10.03
Iron	55.85	0.08492	5.715	1.670	9.97
Tungsten	183.85	0.10211	5.715	0.956	9.97

§4.2.1 Luminosity Monitors

The luminosity monitoring system consisted of an array of four sets of scintillation counters as shown in Figure 4.3.



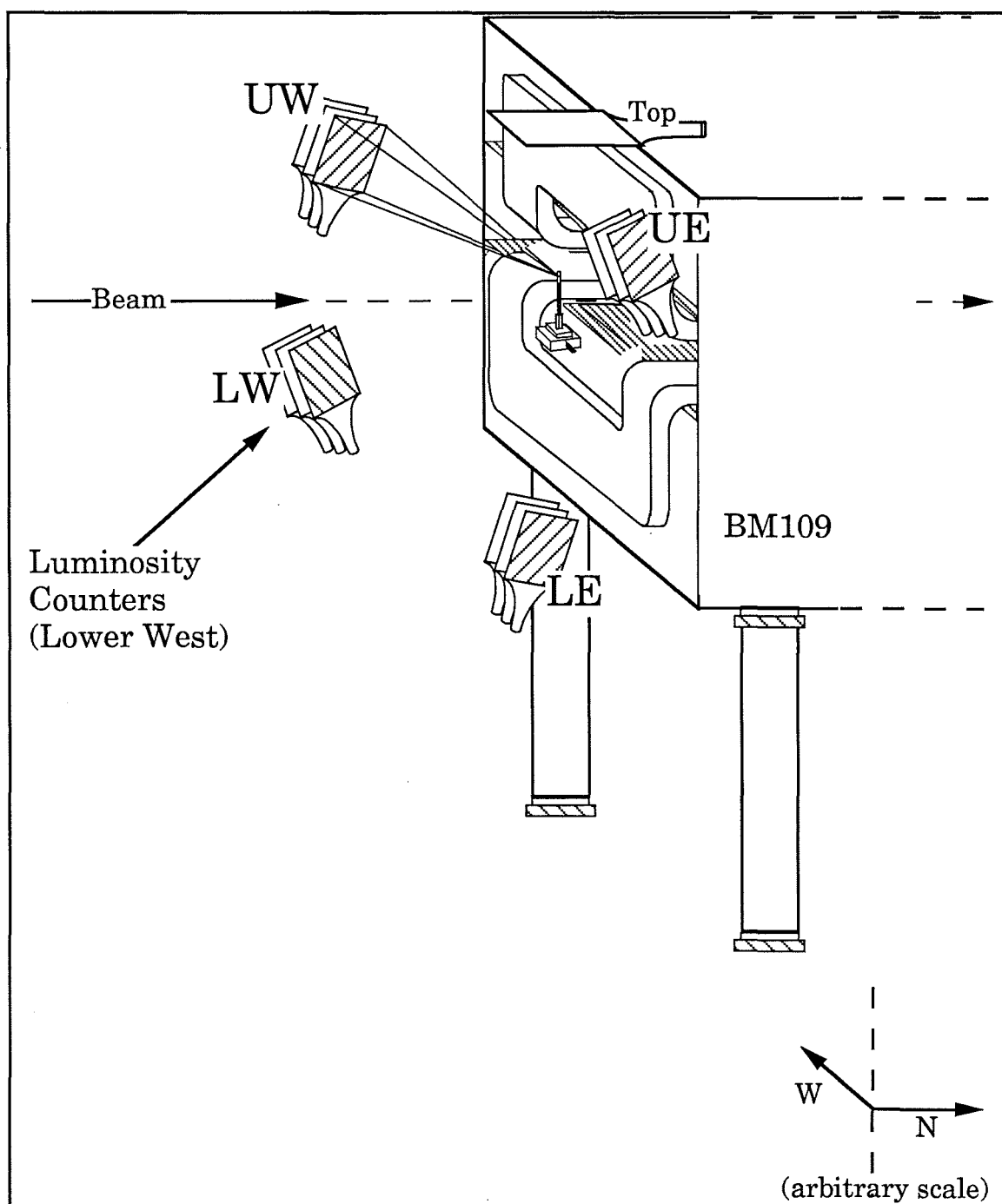


FIGURE 4.3

The Luminosity Monitoring System.

Four sets of Triple coincidence scintillation counters surround the Target Station. The upstream face and coils of the BM109 Magnet are also shown.

They were mounted between the front face of the first analyzing magnet and the upstream shielding wall. These counters measured the radiation produced at nearly 90 degrees to the beam axis within their region of acceptance, and at a distance of about 1.5 meters from the target. The wide angle scattering due to the beam target interaction is proportional to the total interaction rate. The incident beam flux and the fraction of the beam hitting the target as measured by this system are important components in determining the luminosity of the experiment .

The luminosity monitors were calibrated by horizontally scanning each target and correlating the number of counts given by the luminosity monitors,  $N_c$ , with the total beam flux  $N_b$ . The number of counts depends on the beam flux (as measured by the ionization chamber), the fraction of the beam hitting the target,  $F$  and the amount of that beam fraction which interacted with the target producing particles at wide angles and low intensity into the acceptance of the monitors. The target scans produced a horizontal distribution  $f(x, x_b)$ , of the beam intensity with a peak beam-target interaction point,  $x_b$ . This distribution function was parameterized by a gaussian beam distribution centered at  $x_b$ , overlapping a step function target distribution. Integrating the function over the width of the target gives the beam-target fraction,  $F$ .

$$F = \int f(x, x_b) dx \quad (4.1)$$

Therefore accounting for the background from interactions in the air and the target stand, a relation between  $N_c$  and the beam target fraction can be found.

$$N_c = C \left[ N_b \times (F - \text{background}) \right] \quad (4.2)$$

where the proportionality constant  $C$ , is determined for each set of monitors. The four independent measurements were, on the average consistent with each other to within  $\approx 1\text{-}2\%$ , and these target scans were performed when ever the target was changed as well as periodically over the course of the experiment to monitor consistency. Also one pulse scans were performed whenever  $N_c / N_b$  changed.

### **§4.3 The Spectrometer Magnets**

The momentum components of the hadrons produced in the interaction can be determined from the interaction point, the particle deflection due to a static magnetic field, and the particle trajectory downstream of the magnetic field region because of the point-like target in the bend view. Two analysis magnets just downstream of the target station provided the horizontal magnetic deflection for the spectrometer system.

#### **§4.3.1 Magnet Sizes**

The magnets were placed so that the magnetic field was vertically oriented. The vertical aperture dimension of the upstream magnet along the  $y$ -axis was shimmed since this was the limiting aperture of our detector as viewed from the target.

The upstream device, a BM109 magnet, had dimensions of 3.0 meters coil to coil along the beam direction with an aperture size of 50.8 cm in the  $y$  direction and 60.9 cm in the  $x$  direction. The magnetic length was

$\approx 2.65$  meters in the  $z$  direction. The downstream device was a modified 40D48 magnet, with dimensions 1.92 meters long and aperture size 101.6 cm in the  $y$  dimension and 93.7 cm in the  $x$  dimension. Its magnetic length was  $\approx 1.78$  meters long. A "mirror" iron plate was placed on the downstream edge of the 40D48 to shield the first drift chamber from the fringe magnetic field. The  $z$  positions of the magnetic centers relative to the target were 1.14 meters and 3.63 meters for the two magnets.

#### §4.3.2 Field Uniformity and Momentum Kick

The magnetic field in both magnets was oriented in the  $y$  direction, producing magnetic deflection for the charged particles in the  $x$ - $z$  plane. The field strength within the aperture gap of each magnet was measured using the Fermilab ZIPTRACK field measuring system.<sup>55</sup> When three independent coils oriented perpendicular to each other were moved along the  $z$ -axis of the magnets, a current was induced in the coils, integrated and digitized to give a result that was correlated with the strength of the three components of the magnetic field. Figure 4.4 presents a field strength map of the  $y$ -component of the magnetic field along the  $z$ -axis. At the operating currents of these electromagnets, the BM109 had a field strength of  $\approx 1$  tesla and the 40D48 had a field of  $\approx 0.8$  tesla. Each magnet was scanned more than 50 times covering most of the areas of the magnet gap. The measured fields were uniform over most of the magnet aperture volume to within  $\approx 1$ -2%.

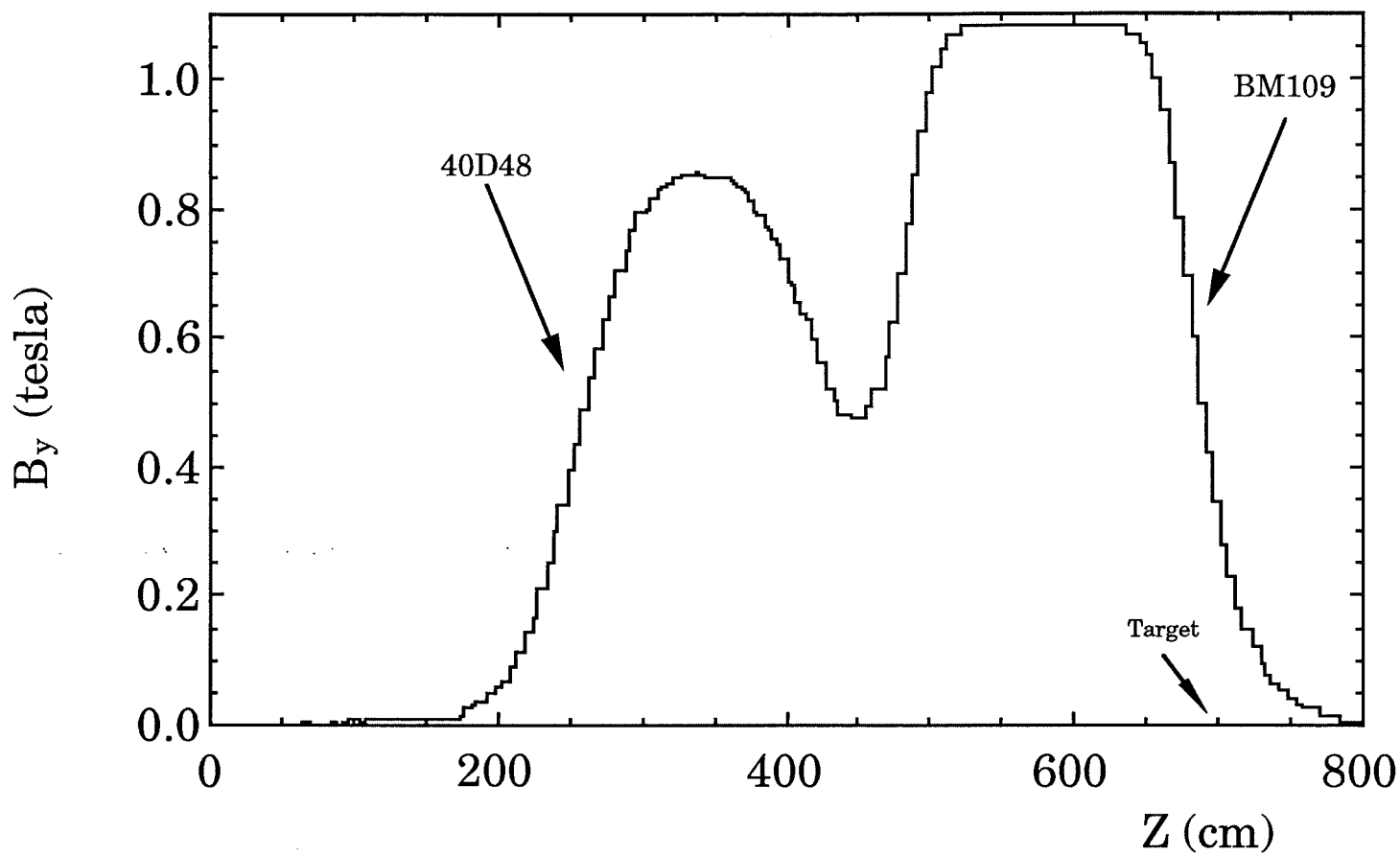


FIGURE 4.4

Measurement of the Y- component of the magnetic  
field strength along the z-axis

The total angle of bend of a charged hadron in the magnetic field is given by the relation (eq. B.2) in Appendix B. This equation also leads to a relation for the transverse momentum deflection (often called the  $p_T$  kick) provided by the magnet and proportional to the magnetic strength,

$$p_T \propto k \int \mathbf{B} \cdot d\mathbf{l}$$

This  $p_T$  kick is characteristic of the magnetic system and our two combined magnets produced a  $p_T$  horizontal kick of 1.16 GeV/c, meaning that an energetic charged particle incident on this magnet system would have experienced a momentum deflection of this amount, upon exiting the downstream magnet gap.

#### **§4.4 The Multiwire Drift Chambers**

A drift chamber is a particle tracking device that uses the drift time of charged ions produced by a charged particle passing through the gas in a chamber, to measure a projection of the spatial position along the particle's trajectory. The coordinate measured is perpendicular to the direction of the wire. A charged particle passing through the gas of the chamber will leave in its wake, a number of electrons and positive ions, along the path of the ionizing radiation. In the same environs, a region of approximately uniform electric field is produced between planes of anode and cathode wires. For most of the time the aforementioned electrons will drift in this electric field toward the anode wires. But within several wire diameters, due to the electric field increase of  $1/r$ , the electrons accelerate to an energy that produces secondary ionizations and these secondary

electrons in turn do the same. This electron avalanche near the anode wire, produces a detectable signal. The position where the particle traversed the chamber is then determined from the drift velocity in the known gas mixture, the measured drift time, and the geometry of the chamber wires and wire spacings.

#### §4.4.1 Dimensions and Alignment

The five chambers (in order of their location, DC1, DC2, DC5, DC3, and DC4), were placed downstream of the analysis magnets, and separated along the z-axis so that the corresponding sense wires would symmetrically align and project back to the target. The chamber locations (z) according to their relative distance to the experimental target and the dimensions (x and y) of the active areas of the chambers are listed in Table 4.2.

Table 4.2

#### **Drift Chamber Active Region and Distance From Target**

<b>Chamber</b>	<b>x (cm)</b>	<b>y (cm)</b>	<b>z (cm)</b>
<b>DC1</b>	103.9	110.4	539.0
<b>DC2</b>	129.5	137.6	675.0
<b>DC5</b>	169.3	175.7	823.0
<b>DC3</b>	224.7	226.8	1118.0
<b>DC4</b>	299.1	302.5	1486.0

The chambers were optically surveyed to the beam axis in the designed location. Interactions detected from the target with the magnets

off were used to align the chambers and set the relative timing of the chambers along with magnet on data to get the chamber to chamber alignment. The chambers (#1 and #4) defined the coordinate system. Triggered events produced wire distributions, and adjustments to the timing were made in the data acquisition software.

#### §4.4.2 Cell Layout and Wire Specifications

The configuration of the wire planes indicated by the cross section of one edge of a chamber is presented in Figure 4.5. The anode or "sense" wire planes were placed between two cathode planes, which produced the perpendicular electric field. Each stack of planes had a ground plane layer at the outside, to shield the sense planes from the electromagnetic interference.

The stack of planes in each chamber included anode planes labeled X, Y, U, and V. The wires in the X, and Y planes were strung vertically and horizontally, respectively, to provide information on the x and y position of the particle's trajectory. The U and V plane wires were oriented 10 degrees clockwise and 10 degrees counter clockwise of vertical to give additional projected coordinates and to associate the projections when there were more than 1 particle in the spectrometer. Each wire tension was approximately 20 grams and the wire glued to the FR-4 circuit board frames. Each frame was then stacked and held in place by alignment pins and metal cores, constructed as part of the aluminum frame of the chamber which allowed for precise placement. With this configuration the wires were optically surveyed for each plane during assembly.



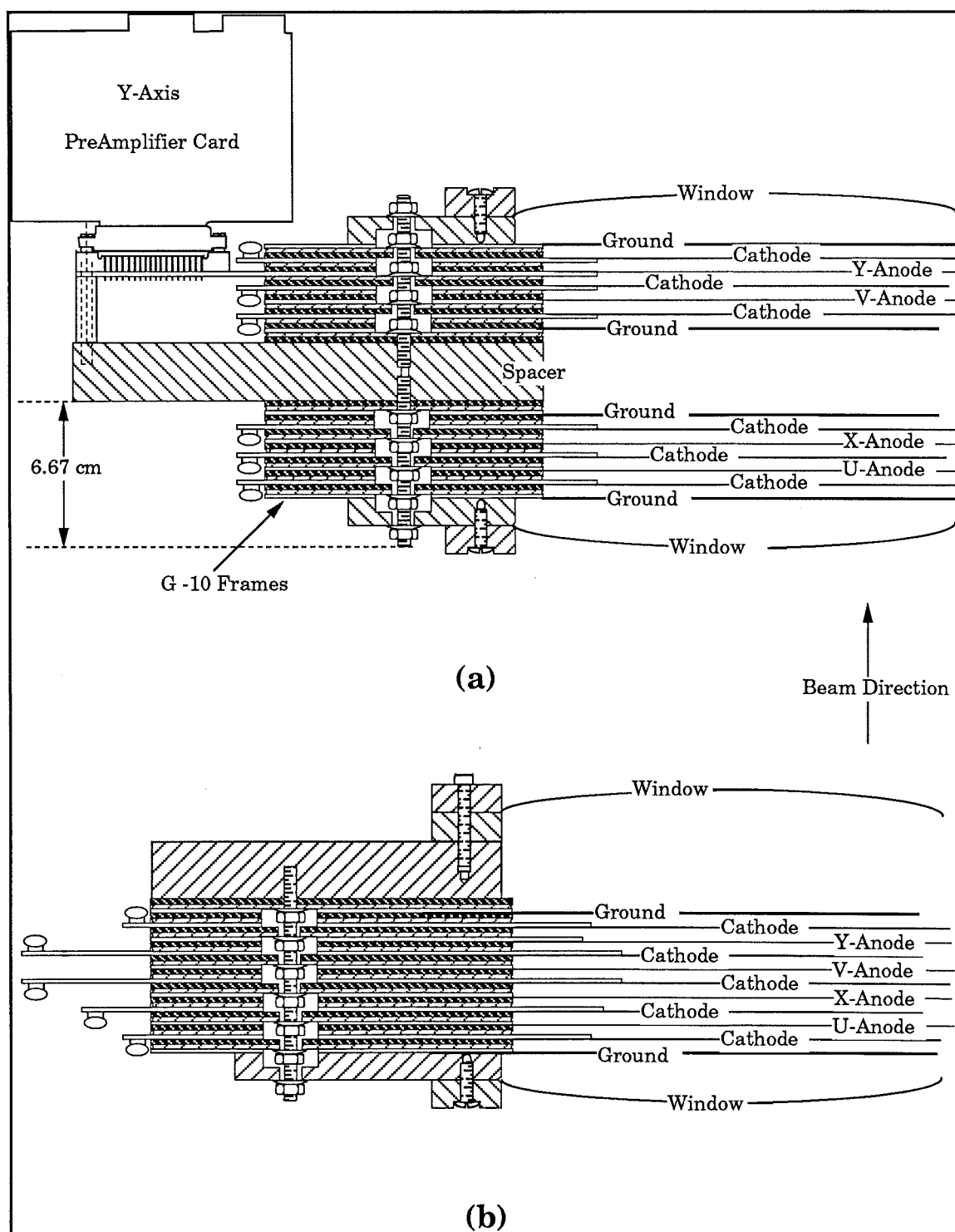


FIGURE 4.5

Portion of the cross section of the drift chambers. DC1 and DC2 used configuration (a), and DC5, DC3, and DC4 used configuration (b).

The sense wires were made of gold plated tungsten for the needed tensile strength and the ability to solder the wire to the readout copper pads. All the other wires were composed of a silver coated alloy of beryllium and copper (Be-3%, and Cu-97%). There were 256 sense wires in the X plane of each chamber and 544 sense wires in the Y planes, (DC5 had 576). The U and V planes had 352 sense wires (but DC1 and DC2 had 320) per chamber.

In the drift space of the chamber, it is desirable to have as uniform an electric field as possible, so that the drift distance will vary linearly with time. The wire spacings in the chambers DC3 and DC4 were large compared to the other chambers. To improve the electric field uniformity, field wires were placed between the anodes and held at positive operating voltages with respect to the approximately grounded sense wires. As mentioned previously the majority of the wire spacings were designed to produce a symmetric geometry that projected back to the target. The field shaping wires had the same spacing as the anode wires but were shifted by  $1/2$  cell. The wire spacings are presented in Table 4.3.

Table 4.3  
**Drift Chamber Wire Spacings**  
 units of millimeters

Chamber		Anode	Cathode	Field	Ground
DC1		2.03	1.0	—	2.0
DC2		2.53	1.0	—	2.0
DC5		3.05	2.0	—	2.0
DC3	Plane				
	X,Y	4.17	2.0	4.17	2.0
	U,V	4.11	2.0	4.11	2.0
DC4	Plane				
	X,Y	5.56	2.0	5.56	2.0
	U,V	5.47	2.0	5.47	2.0

The cathode plane to the anode plane separation was 0.51cm for DC1 and DC2, while the separation for the downstream chambers DC5, DC3, and DC4 was 0.66cm. The cathode plane to ground plane separation was the same as above with the exception of a 0.25mm shim added to DC4 to improve voltage stability.

The diameters of all of the anode wires was 25.4 $\mu$ m and 76.2 $\mu$ m for the field wires. The ground wires were 127 $\mu$ m in diameter, while all cathode wires were 76.2 $\mu$ m, except for the 63.5 $\mu$ m cathode wires of DC1.

#### §4.4.3 The Central Beam Region

This experiment was often operated with a beam flux of nearly  $3 \times 10^8$  protons per pulse. The particle detection efficiency depended on the particle flux, the chamber high voltages, and the chamber gas composition.

The operating voltages of the chambers were set for the expected flux of high  $p_T$  scattered particles in the active regions of the chambers. Consequentially, in the central region, (where the large flux of non-interacting beam particles and low transverse momentum scattered particles traverse the chambers), the ionization produced would be considerably larger. In fact the signal from these wires would be continuously produced during the beam spill.

To alleviate this problem, the drift chambers were desensitized in the central beam region. The horizontally oriented cathode wires in this region (88 wires) were operated approximately 400 volts lower than the active regions. Also, to minimize electric field gradients, a "transition" region (between the active and the desensitized region, using 16 wires) was maintained at approximately 200 volts lower than the active region.

#### §4.4.4 The Gas Mixture

The passage of charged particles through the chambers leaves charged ions in the particles' wake along their trajectory. Some desirable properties of the gas mixture for these chambers include low operating

voltage, high signal gain, high interaction rate capability, and a fast recovery time.<sup>56</sup>

The upstream chambers, DC1, DC2, and DC5 used a gas mixture of argon (82%), carbon dioxide (17.0%), and Freon (0.4%). DC3 and DC4 were operated with a argon (50%) and ethane (50%) mixture filtered through an ethyl alcohol bath at a temperature 0°C. The chambers were operated at room temperature and a slight over pressure to ensure a uniform flow of gas through the system and prevent air contamination. RTV silicon rubber was used to form the gas seal on the aluminum frame and the gas was confined to the chamber using Mylar plastic windows approximately 0.5 mm thick.

#### §4.4.5 Drift Chamber Operating Conditions

The chambers were operated in a high beam flux environment. In such a high intensity beam, it is necessary to operate the chambers at a voltage level that is low enough to prevent the gas from becoming continuously ionized (Geiger mode), and causing chamber voltage breakdown. This lower voltage (and therefore weaker electric field) reduces the signal size on the sense wires. Thus the signal from each sense wire was amplified twice in separate and different stages. First the direct signal from each wire was connected to a preamplifier (as shown in Figure 4.5) which produced a gain of  $\approx 20$ . Second, the output signal of the preamplifier was connected to amplifier/discriminator circuits (Nanometric 272) which produced an emitter coupled logic pulse (ECL). Information on the preamplifiers and the amplifiers is given in Appendix

C. Through delay cables, the logic pulses were used as inputs to the time-to-digital converters (LeCroy TDC's) which produced the recorded digital information for determining the drift times and consequentially the spatial position from the wire.

Depending on the sense wire spacing, the maximum drift times varied from 100 to 400 nanoseconds (nsec). The spatial resolution depends on the timing measurement and the drift velocity. With a maximum wire spacing of 5.56mm, and a 100nsec drift time, the drift velocity was approximately 5.56cm/ $\mu$ s. A typical timing measurement accuracy of 4nsec leads to a spatial resolution of approximately 222 $\mu$ m.

Typical operating voltages for the chambers are shown in Table 4.4.

Table 4.4

**Chamber Operating Voltages**

Chamber	Cathode (kVolts)	Field (kVolts)
DC1	-3.05	—
DC2	-3.30	—
DC5	-3.65	—
DC3	-2.40	-1.40
DC4	-2.30	-1.45

The particle detection efficiency at the nominal operating conditions varies from chamber to chamber and plane to plane. The plane efficiency was determined by requiring that a track in the spectrometer would be

recognized by the track reconstruction programs, without using actual data from that plane. The fraction of the time that the plane produced actual data for that requirement was stated as the efficiency. One set of representative chamber plane efficiencies is shown in Table 4.5. The chambers were also affected by dead sense wires, which were timely repaired when possible. Thus the plane efficiencies varied with time due to the intermittent lost of clusters of sense wires per plane.

**Table 4.5**  
**Chamber Plane Efficiencies**

<b>Chamber</b>	<b>X</b>	<b>Y</b>	<b>U</b>	<b>V</b>
<b>DC1</b>	0.778	0.698	0.742	0.837
<b>DC2</b>	0.895	0.740	0.883	0.814
<b>DC5</b>	0.776	0.644	0.776	0.753
<b>DC3</b>	0.887	0.899	0.885	0.934
<b>DC4</b>	0.946	0.912	0.952	0.948

#### **§4.5 The Hodoscopes and Calorimeters**

The hodoscopes and calorimeters produced a real time event signal that was used to indicate the occurrence of interacting events in the experiment. The two vertically separated arms of the system each consisted of two hodoscope planes followed by a sampling calorimeter. Fast photomultiplier tubes in conjunction with scintillator material produced the fast response signal required for the trigger. Similar to the drift chamber geometry, the calorimeter system was also positioned and the elements segmented to produce a symmetric projection back to the target.

Polyvinyl toulene (PVT), a Bicron Corporation manufactured scintillator (#BC 408) was used in this system. The scintillator has an attenuation length of  $\approx 1.5\text{m}$ , and photon pulse emission within 10nsec. The two types of photomultiplier tubes (PMT) used were manufactured by the Hamamatsu Corporation. The hodoscopes utilized the 12 stage type R329 with a signal rise time of  $\approx 2.6\text{nsec}$ , while the calorimeters used the 10 stage type R2154 tubes with a rise time of  $\approx 3.4\text{nsec}$ .<sup>57</sup>

The LeCroy 1440 high voltage system was used to supply the voltage to the PMT bases, and was externally computer controlled by a VAX-780 computer.

#### §4.5.1 The Hodoscopes

The initial identification of charged particles in the calorimeter was accomplished using sets of vertically segmented scintillation counters in front of each calorimeter. Each hodoscope consisted of two planes, HF(front) and HB (back) of 16 separate scintillation counters each. The planes were mounted so that the counters slightly overlapped, thus eliminating the open spaces between the counters. The counters were composed of a plate of scintillator 0.93cm thick, with Lucite plastic connecting each end of the scintillator to the 51mm diameter photomultiplier tubes.

The voltage of the phototubes at the end of the hodoscope elements was set such that a minimum ionizing particle would produce a pulse



height of  $-100$  mVolts at the output. The PMT output was adjusted using a resistor in the PMT base.

The dimensions of each module in the hodoscope plane are listed in Table 4.6, and a hodoscope section is shown in Figure 4.6.

**Table 4.6**

**HF and HB Hodoscope Dimensions**

Scintillator Thickness  $z=0.93$  cm

Module #	X(cm)	Y(cm)
1	29.5	6.35
2	33.8	6.35
3	38.1	6.35
4	42.2	6.35
5	46.5	6.35
6	52.8	8.89
7	59.2	8.89
8	65.8	8.89
9	72.1	8.89
10	82.6	14.0
11	93.2	14.0
12	103.9	14.0
13	114.3	14.0
14	125.0	14.0
15	134.6	14.0
16	146.3	14.0

#### §4.5.2 The Calorimeters

Calorimeters in general, are devices in which a particle whose energy is to be measured, deposits all of its energy in the material of the device. The composition of the material is such that a certain fraction of the initial energy of the particle is transformed into a detectable signal, because the particle interacts and deposits all of its energy in the form of a "shower" of decreasingly lower energy particles. These total absorption detectors can be of two general classes, the homogeneous calorimeter and the type that periodically samples the development of the shower (i.e. sampling calorimeter). The two major types of sampling calorimeters identify particles that initiate 1) an electromagnetic, or 2) a hadronic shower. This experiment used sampling calorimeters for the particle energy measurement. The energy is measured in a number of sensitive layers interspersed by passive absorbers. The general configuration of our detector was a number of plates of metallic absorber interleaved with scintillator planes as the active material. Thus the sensitivity of the detector depended on the detection of light from these planes. The passive absorber for the electromagnetic part of the calorimeter was lead, while iron was used in the hadronic part. In these detectors, one measures the energy loss of the shower particles as they traverse the active layer of the detector. This represents a fraction of the total energy of the particle that generated the shower.

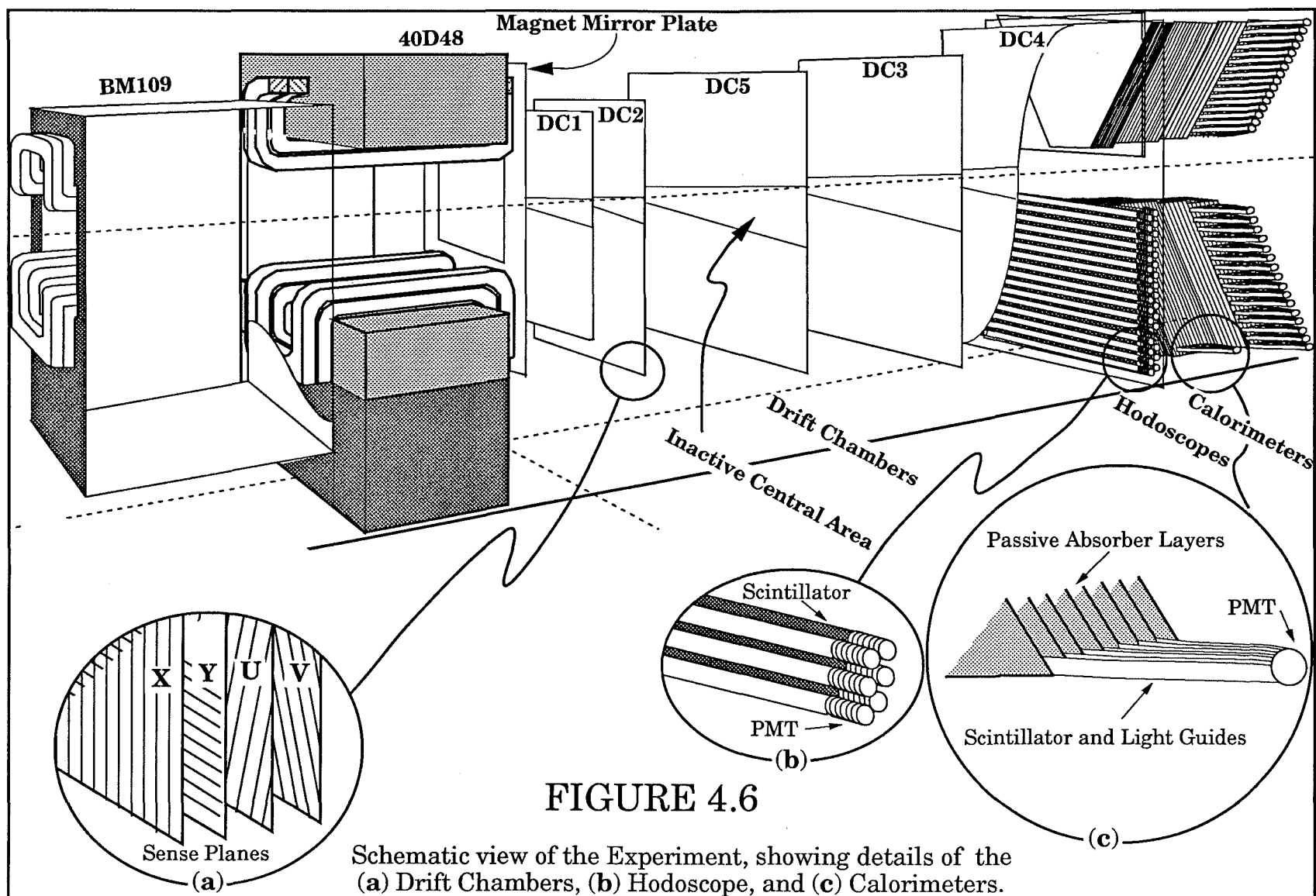
The energy loss mechanisms relevant to high energy electromagnetic showers include ionization for electrons and positrons,

$e^+e^-$  pair production, Compton scattering and the photo-electric effect for photons. Bremsstrahlung however, accounts for the principle source of energy loss at high energies. As a 1 GeV electron passes through material it will electromagnetically radiate many photons. Photons with energy greater than 5→10 MeV will create  $e^+e^-$  pairs. The energetic electrons and positrons from this process will also radiate photons and the process will continue until the subsequent particles possess too low an energy to produce more particles. Within the material charged particles will have a mean range and ionization loss ( $dE/dx$ ) characteristic of that material. The average energy loss of this shower of particles correspond to the penetration range inside the material. As the shower develops, the spectrum of particles becomes softer and eventually gets absorbed in the material of the detector.

Calorimetric energy measurements for the hadron shower are conceptually similar to that of the electromagnetic shower. A number of important processes contribute to the propagation of the hadron showers and energy loss in the sampling detector. When the high energy hadron penetrates the material, it initially may pass on nearly 50% of its energy through scattered secondary hadron ionization. Also nearly 30% of the particles produced in each hadron collision are  $\pi^0$ 's from nuclear interactions. The  $\pi^0 \rightarrow \gamma\gamma$  and  $\pi^0 \rightarrow e^+e^-\gamma$  channels give rise to electromagnetic showers. Therefore nearly all the particles in the hadron shower are the  $e^+$ ,  $e^-$ , and  $\gamma$ 's. Other processes such as neutrino production and primary hadron ionization in addition contribute to the energy loss and the process continues until the showers are completely

absorbed in the detector. The dimension of the shower is determined by the mean free path between interactions (i.e. the nuclear interaction length). Therefore knowing the interaction length of the material, determines the depth of the detector that will completely contain the shower.

Each of the calorimeters in this experiment was composed of four sections: the electromagnetic (EM) and three hadronic sections (H1, H2, and H3). Each section in depth, was composed of alternate layers of scintillator and metal. The scintillator layer was further divided along the y-axis into 16 different modules. Figure 4.6 illustrates the general structure of these detectors. The EM as well as the H1 sections consisted of 14 layers of 0.635cm thick scintillator. There were 13 plates of 1.27cm thick lead for the EM, while H1 used 14 plates of 3.175cm thick steel. Sections H2 and H3 both used 7 plates of 6.35cm thick steel as an absorber with 7 layers of scintillator. The vertical segmentation into 16 modules of scintillator and associated layers of metal, made possible the isolation of energy within a module segment that could be directly associated with a single particle track detected by the drift chambers. The dimensions of the calorimeter modules are listed in Table 4.7. The geometric angular acceptance was  $\pm 25.3$  degrees in azimuth ( $\phi$ ), and a vertical angle  $\theta_y$  range of  $\pm (20 \text{ mrad} \rightarrow 100 \text{ mrad})$  from the beam axis target location in the laboratory reference frame. A detail of the calorimeter section is shown in Figure 4.7.



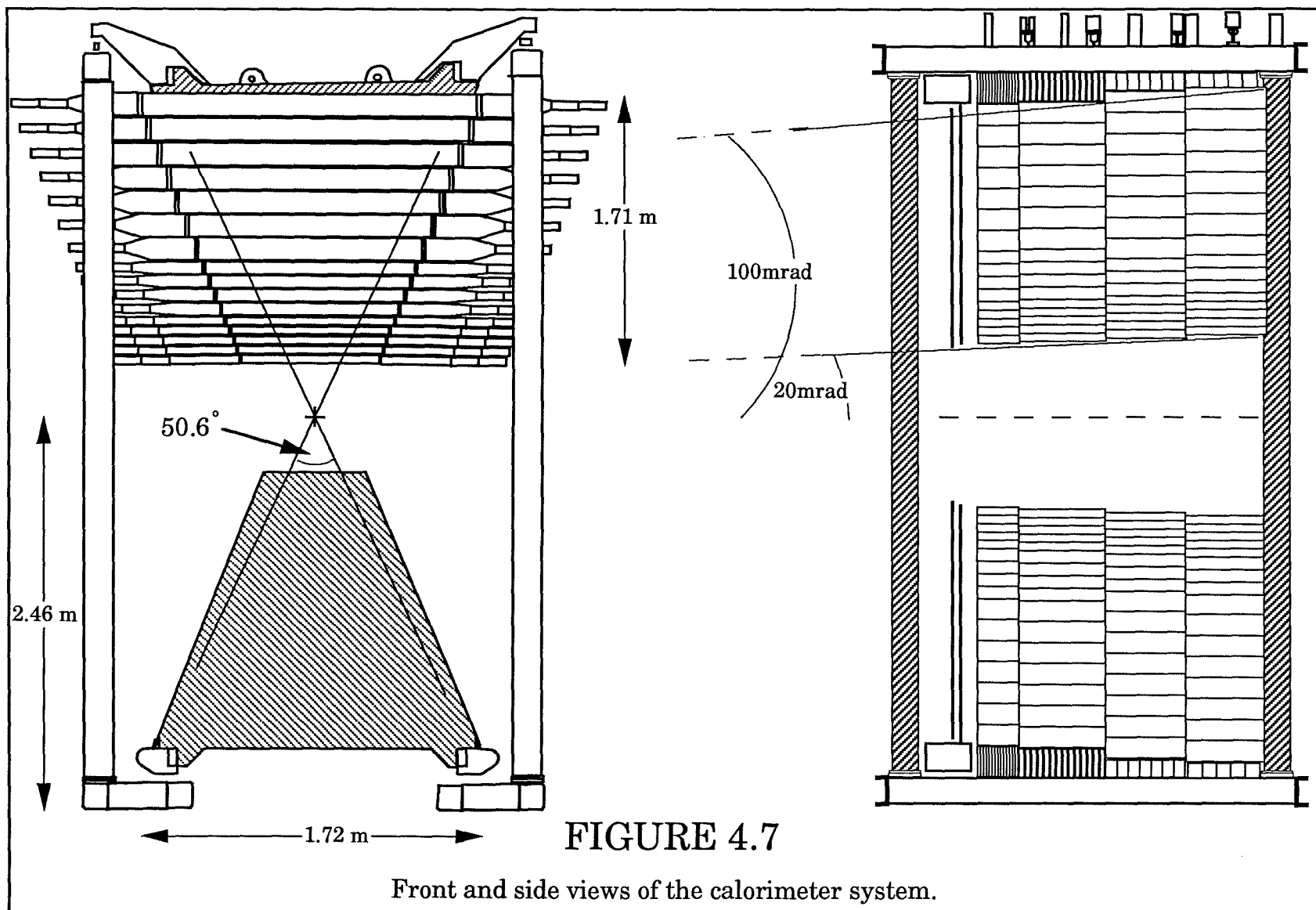


Table 4.7

**Calorimeter Module Dimensions**Scintillator Thickness  $z=0.635$  cm

Module #	EM and H1		H2 and H3	
	X (cm)	Y (cm)	X (cm)	Y (cm)
1	44.7	5.1	49.0	5.1
2	49.0	5.1	53.3	5.1
3	53.3	5.1	57.4	5.1
4	57.4	5.1	61.7	5.1
5	61.7	5.1	66.0	5.1
6	68.1	7.6	74.4	7.6
7	74.4	7.6	81.0	7.6
8	81.0	7.6	87.4	7.6
9	87.4	7.6	97.8	12.7
10	97.8	12.7	108.5	12.7
11	108.5	12.7	119.1	12.7
12	119.1	12.7	129.5	12.7
13	129.5	12.7	140.2	12.7
14	140.2	12.7	150.9	12.7
15	150.9	12.7	161.5	12.7
16	161.5	12.7	172.0	12.7

The depth for these calorimeters based on the radiation and interaction lengths was chosen so that the electromagnetic shower would be contained in the electromagnetic section and the hadronic shower would be contained in the total calorimeter. The EM section was 29.69 radiation lengths along the z axis and the complete calorimeter was 9.24 proton interaction lengths long.

#### §4.5.3 The Calorimeter Operating Conditions

A photomultiplier tube was mounted at each end of each module, and the high voltage to the PMT base was supplied by a computer controlled LeCroy 1440 high voltage supply. Because the pulse heights of signals from muons and hadrons in the calorimeter could not be digitized at the same scale in the analog to digital converters (15-bit LeCroy 2285 ADC), the calorimeters were operated at two different gain settings. This was done to facilitate the calibration of the calorimeters with both muons and hadrons discussed in the next section. Operationally the gain of the R2154 photo tube was adjusted by a potentiometer connected to the 6<sup>th</sup> dynode in the PMT base. For a steady and constant voltage across the dynodes, the high gain to low gain settings could not be distinguished by any timing characteristic changes of the phototube signal. The electrical schematic diagrams for both the hodoscope and calorimeter PMT bases are presented in Appendix C.

During normal data acquisition, the calorimeter was set for low gain. The particular setting of a given module was determined to keep the PMT pulse heights and the corresponding ADC counts within a



reasonable range. The low gain to high gain ratios were proportional to a factor of  $\sin \theta_y$  where  $\theta_y$  was the polar angle relative to the target and beam axis for each module. When adjusted by this factor for the proper gain, the response of the PMT was proportional to the transverse momentum of the incoming hadron. The high gain settings were made with muons to produce a uniform response of the PMT. The low gain settings were used in the normal data acquisition mode. The low gain to high gain ratios were measured periodically using radioactive sources and light emitting diodes (LEDs) and adjusted to a predetermined factor relative to the high gain setting, throughout the experimental data acquisition.

#### §4.5.4 The Calorimeter Calibration

The calibration of the calorimeter included a hardware calibration facilitated by adjusting the high gain and low gain of the photomultiplier tubes such that the response of the modules was proportional to the transverse energy of a hadron within that module. In addition to this calibration, a monoenergetic particle beam at low intensity was used to calibrate the calorimeter response with hadrons of known energy.

The gains of the phototubes were set using a calculation of the muon energy deposition in the calorimeters. Knowing the energy range of the minimum ionizing particles in the materials, and the thickness of the material, one can calculate the peak muon energy deposited in the material. Table 4.8 list the muon energy deposition for various material depths used in the four sections of the calorimeter.

**Table 4.8****Muon Energy Deposition in the Calorimeter**

Section	Total Material Thickness (cm)			Peak Muon Energy (MeV)
	Scintillator	Lead	Steel	
<b>EM</b>	8.89	16.51	—	208.5
<b>H1</b>	8.89	—	44.45	490.9
<b>H2</b>	4.45	—	44.45	483.2
<b>H3</b>	4.45	—	44.45	483.2

The gains of the PMT's for each module in the calorimeter were set so the peaks of the muon energy distribution in ADC counts were made the same number. The high gains of the four sections (EM, H1, H2, H3) of the calorimeter were therefore set to a relative ratio of :<sup>58</sup>

$$0.44 : 1.0 : 1.0 : 1.0$$

to correspond to the approximate relative ratios of the energy deposited for a minimum ionizing particle in the material.

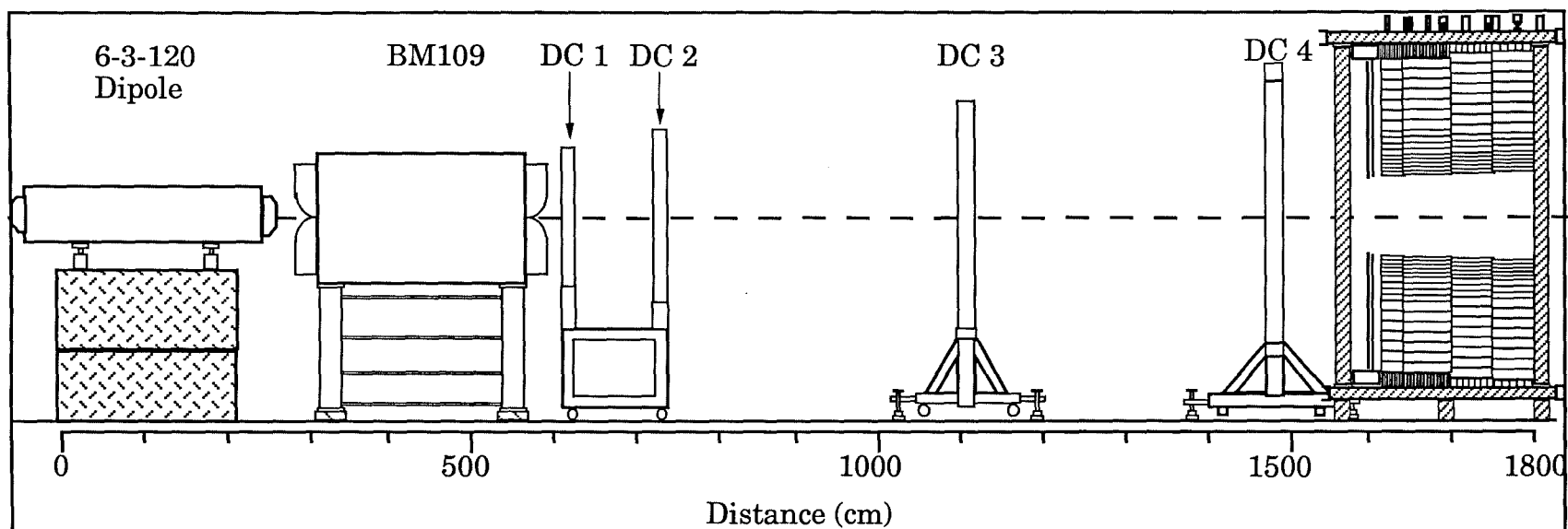
The low gains were set relative to the high gains proportional to  $\sin \theta_y$ , so that

$$\frac{\text{low gain}}{\text{high gain}} = C \times \sin \theta_y ,$$

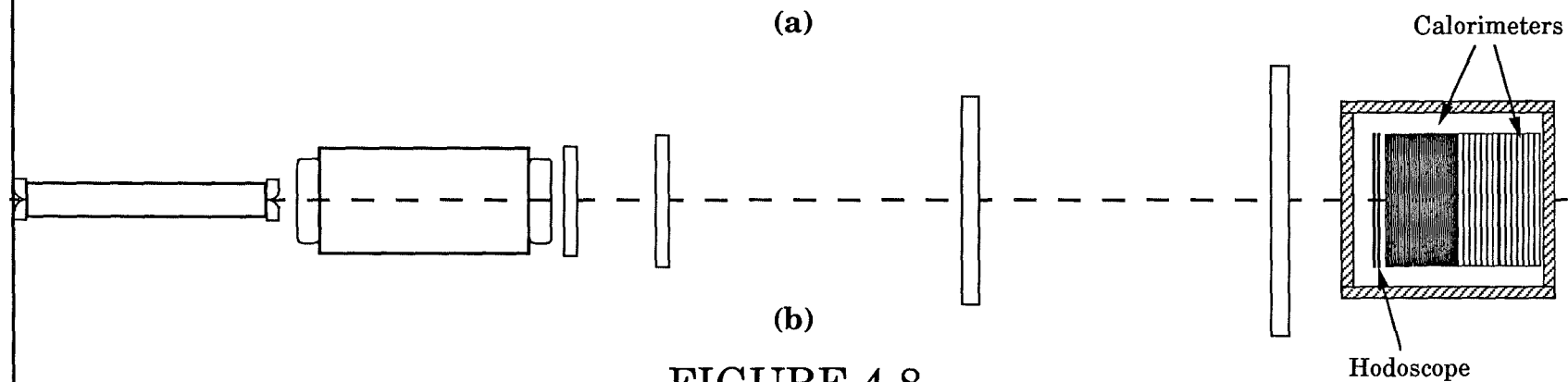
with 
$$\sin \theta_y = \frac{y}{\sqrt{y^2 + z^2}}$$

where  $C$  is a constant,  $\theta_y$  is the polar angle at  $x=0$ ,  $y$  is the vertical distance from the beam axis, and  $z$  is the distance from the target. The low gain to high gain ratios could be maintained by adjusting the base gain and the module response was checked by light-emitting diodes (LED) which were installed near the front face region of each photomultiplier tube.

The 800 GeV/c proton beam impinging on a thick metal target placed in the NE beamline in the NE8 enclosure (see Figure 3.3), produced a secondary meson beam for the detector calibration. By scaling the currents in the subsequent magnets, the beamline momentum selected a particular energy for transport to the calorimeter. An auxiliary dipole magnet (6-3-120) with its field oriented horizontally and placed in the location of the experimental target, was used to sweep the secondary hadron beam into specific modules of the calorimeter. Figure 4.8 illustrates the configuration for the calibration beam.



(a)



(b)

FIGURE 4.8

Layout of the Calibration Beam Setup

(a) Elevation (Bend View); (b) Plan View

The ADC counts produced by the pulse height of each PMT were scaled by the ADC counts generated from the muon calibration. A general expression for the hadron energy ( $E_{\text{beam}}$ ) in terms of the scaled ADC counts ( $X$ ) and calibration constants ( $C$ ) can be written:

$$E_{\text{beam}} = \sum_{i=1}^4 C_i(z) \sum_{j=1}^2 \sum_{k=1}^{16} X_{ijk}(x,y) \quad (4.3)$$

In this equation there are four calibration constants corresponding to each section of the calorimeter in  $z$ , so that the index  $i$  has a range of 4. The index  $j$  represents the signal from the two PMT's at either end of the module, while the index  $k$  has a range over the 16 modules. The calibration constants therefore relate the number of minimum ionizing particles deposited in a section of the calorimeter with the energy lost by the hadronic shower in that section. With known pulse height response and hadron calibration beam energy, the calibration constants can be calculated<sup>59</sup> by minimizing the  $\chi^2$  which is defined:

$$\chi^2 = \frac{\left[ E_{\text{beam}} - \sum_{i=1}^4 C_i(z) \sum_{j=1}^2 \sum_{k=1}^{16} X_{ijk}(x,y) \right]^2}{\sigma^2} \quad (4.4)$$

Here  $\sigma$  is the error in the beam energy and the calorimeter measurement, namely:

$$\sigma = \sqrt{(\Delta E_{\text{beam}})^2 + (\Delta E_{\text{calorimeter}})^2} \quad (4.5)$$

The calibration was determined from data produced by the hadron beam incident on the upper calorimeter. The minimization of  $\chi^2$  with respect to the calibration constants produced the results and a typical one is listed in Table 4.9.<sup>60</sup> The errors in the constants were statistical. The systematic errors were determined from deviations in the calibration constants for two different measurements, and were estimated to be 5%, 2%, 9%, and 19%, for EM, H1, H2, and H3 respectively.

The corrected energy resolution using the average beam energy ( $E$ ) and the beam energy resolution  $\Delta E_{\text{beam}}$ , leads to the calorimeter resolution. That is, from eq. (4.5):

$$\left(\frac{\sigma}{E}\right)^2 = \left[\left(\frac{\Delta E_{\text{beam}}}{E}\right)^2 + \left(\frac{\Delta E_{\text{calorimeter}}}{E}\right)^2\right] \quad (4.6)$$

A sampling calorimeter fractional energy resolution is known to be related as :<sup>61</sup>

$$\frac{\Delta E_{\text{calorimeter}}}{E} = \text{constant} / \sqrt{E}.$$

Figure 4.9 presents a total energy distribution measured by the calorimeter using the data and constraints listed in Table 4.9. The event selection in Table 4.9 is based upon the number of ADC counts in the Phototubes corresponding to an equivalent number of minimum ionizing particles (MIP's), as well as the position of the particle showers on the specific modules. The hodoscope required 0.65 MIP's in a module to be identified as an incident single particle, and the calorimeter required 30 MIP's, while the EM section required a pulse height corresponding to at

least 1 MIP's. From Table 4.9, 7371 events survived these two cuts. Noting the measurements listed, the  $y$  position cut restricted the particle shower to be in a vertical position contained within the vertical edges of a module. This also assured a more precisely defined momentum. The  $y$ -difference cut constrained the difference between the center of the module which contained the most MIP's and the actual vertical position (i.e.  $y$ -cut), to be no greater than 5 cm.

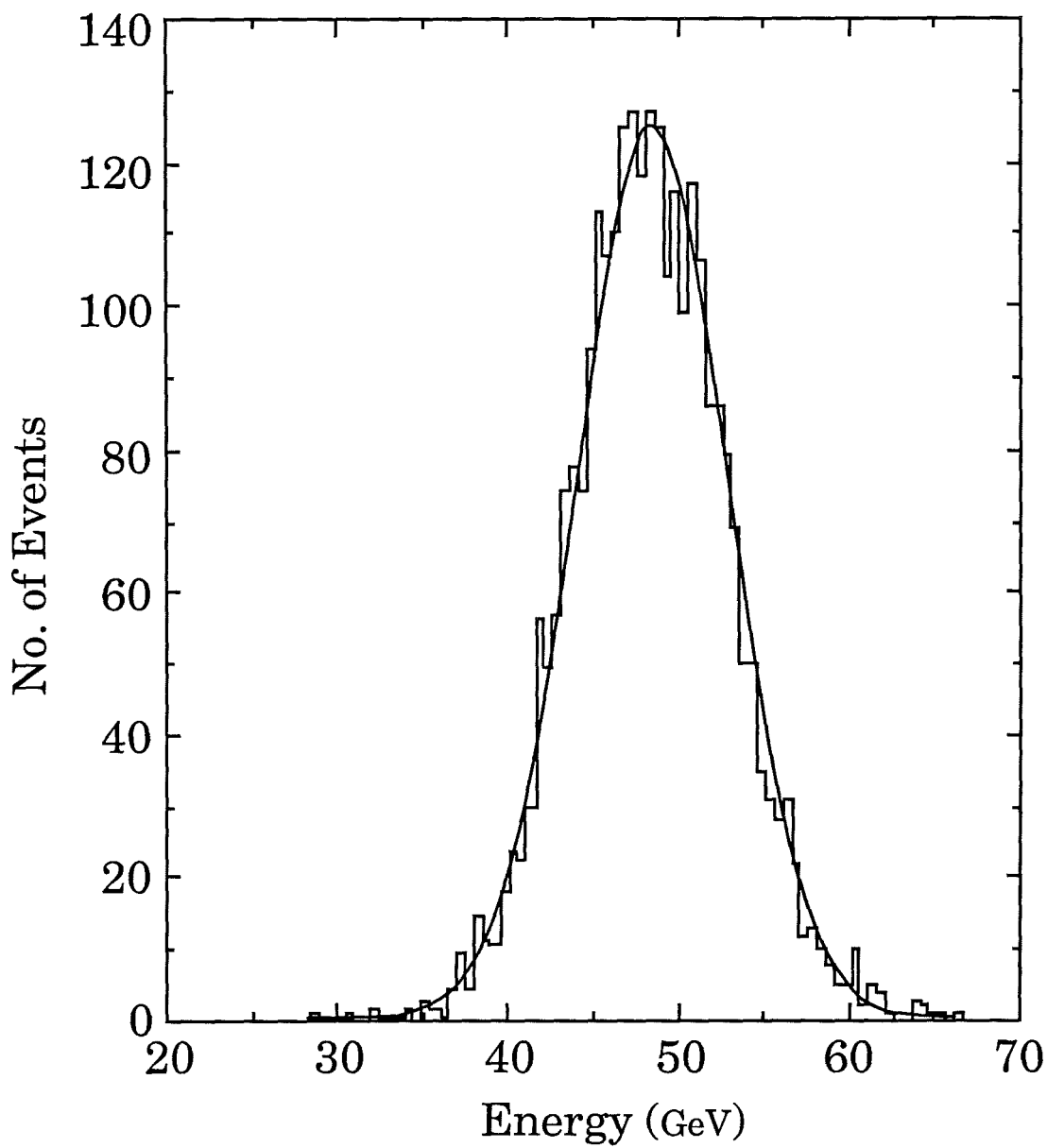


FIGURE 4.9

The total energy distribution measured by the calorimeter using the data listed in Table 4.9. The curve shown is a gaussian fit to the data



**Table 4.9****Calorimeter Calibration Results**Derived from Run 114, Beam energy  $48.8 \text{ GeV} \pm 2.7\%$ 

(Reference 60)	
Attribute	Results
Run 114	9924 events
No. after hodoscope cut	7641 events
No. after EM cut	7371 events
No. after Y position cut	5726 events
No. after Y difference cut	5184 events
Total selected events	5184 events
High gain calibration	7 MeV/ADC count
Relative calibration constants	
$C_1$ (EM section)	$0.446 \pm 0.002$
$C_2$ (H1 section)	$0.930 \pm 0.004$
$C_3$ (H2 section)	$0.855 \pm 0.009$
$C_4$ (H3 section)	$0.923 \pm 0.030$
Resolution	
$\sigma / E$ of corrected energy	9.6 %
$\Delta E_{\text{calorimeter}} / E$	$64\% / \sqrt{E}$

## CHAPTER 5

### TRIGGER AND DATA ACQUISITION

#### **§5.1 General Considerations**

High energy detectors are capable of producing electronic signals that indicate that a particle interaction has taken place and generate some signals that are correlated with the characteristics of the final state that is under study. The combination of the spatial and temporal correlation of these signals can produce a single signal which is called a trigger used to enable the digitizing and readout sequence.

In the discussion in Chapter 2, it was noted that an event can be initiated by a single high- $p_T$  particle called a trigger particle. This trigger particle is associated with jets and that 75% to 90% of the trigger side jet momentum is carried by this leading particle. Because of this large momentum fraction, it is thought that the trigger hadron momentum approximates the scattered parton momentum. This feature was exploited in the design of the dihadron trigger where an event has a pair of leading particles, one for each of the high- $p_T$  jets. This pair is used to formulate a unique dihadron event. The high- $p_T$  dihadron events occurred a small fraction of the time out of nearly  $2.5 \times 10^6$  interactions/sec. When the trigger logic signals were satisfied, all the salient information describing the event was interrogated and stored on magnetic tape. During the 5msec

to 10msec "dead time", the trigger logic was disengaged to allow the information to be digitized and read out.

The experiment was monitored using a variety of computers dedicated to observing the beamline devices, reading out the ADC and TDC digitized signals, and performing some online analysis.

## **§5.2 The Event Trigger**

An event satisfied the trigger when a high- $p_T$  hadron was detected in each of the upper and lower calorimeters, within specific timing constraints and above a momentum threshold.

The charged particle signal was provided by the hodoscope while the transverse momentum of the hadrons was determined by the localized energy deposition within the segmentation of the calorimeter. Similar to the definition presented in Chapter 2, the effective mass of the dihadron state can now be approximated as the sum of the transverse momentum components ( $p_T$ ) of the two hadrons. Namely:

$$M_{h_1 h_2} \approx p_{T_1} + p_{T_2}$$

where the subscripts 1 and 2, refer to the two different hadrons. Logic signals based on this selection were used to form the mass trigger. In addition the symmetry of the pair trigger was formed with combinations of the charged,  $p_T$ , and mass logic signals.

The modules of both the hodoscope and the calorimeter were numbered from 1 to 16 ranging from a position closest to the beam axis for

number 1 and farthest away for number 16 (see Figure 4.7). The modules were grouped vertically in sets of 2 adjacent modules for the hodoscope and sets of 4 adjacent modules for the calorimeter, called segments. For each combination of one upper and one lower segment in the calorimeter, one can form a sum of all the scintillator pulse heights weighted by the angle for that scintillator from the target. The width of the hadron shower and the energy resolution along with the scintillator slat width are the determining factors in the  $\theta$  resolution and thus the  $p_T$  resolution. The energy can be approximated by the momentum  $p$  such that for a particular angle,  $p_y$  (the  $y$  component of the momentum) is the major component of the transverse momentum and thus  $E_y$  is a good approximation of the  $p_T$  of the hadron. Therefore the minimum segment size was chosen so that it contained the entire energy of a hadron shower. Table 5.1 lists the components of the 12 segments for the hodoscope and the calorimeter, in terms of the detector modules. It should be noted that the module nearest to the beam for the calorimeter and the first two modules nearest the beam for the hodoscope were not included in the trigger system, because of the high multiplicity of particles in the region near the high intensity beam and because of the shower containment. Thus the rate of particles in these modules would be prohibitively high.

**TABLE 5.1****Calorimeter and Hodoscope Segmentation**

Segment	Hodoscope Elements	Calorimeter		
		Modules	Segment Sizes (cm)	
			EM & H1	H2 & H3
1	3-4	2-3-4-5	20.4	22.9
2	4-5	3-4-5-6	22.9	25.4
3	5-6	4-5-6-7	25.4	27.9
4	6-7	5-6-7-8	27.9	30.4
5	7-8	6-7-8-9	30.4	35.5
6	8-9	7-8-9-10	35.5	40.6
7	9-10	8-9-10-11	40.6	45.7
8	10-11	9-10-11-12	45.7	50.8
9	11-12	10-11-12-13	50.8	50.8
10	12-13	11-12-13-14	50.8	50.8
11	13-14	12-13-14-15	50.8	50.8
12	14-15	13-14-15-16	50.8	50.8

### §5.2.1 Charge and $p_T$ Signal

The purpose of the hodoscope was to signal the presence of a charged particle in the spectrometer. In the previous chapter, the dimensions and configurations of the hodoscopes were given. With this geometry, the signals from the individual elements of this detector were used to create the  $Q_k$  ( or charge) logic signal. A coincidence was required between the discriminated signals from two ends of the front modules combined with the analogue sum of the back modules. The  $Q_k$  logic signals can be written symbolically as:

$$Q_k = \left[ \left( HF_{k+2}^E \cdot HF_{k+2}^W \right) \cdot \left( HB_{k+2}^E + HB_{k+2}^W \right) \right] \cdot \text{OR} \cdot \\ \left[ \left( HF_{k+3}^E \cdot HF_{k+3}^W \right) \cdot \left( HB_{k+3}^E + HB_{k+3}^W \right) \right]$$

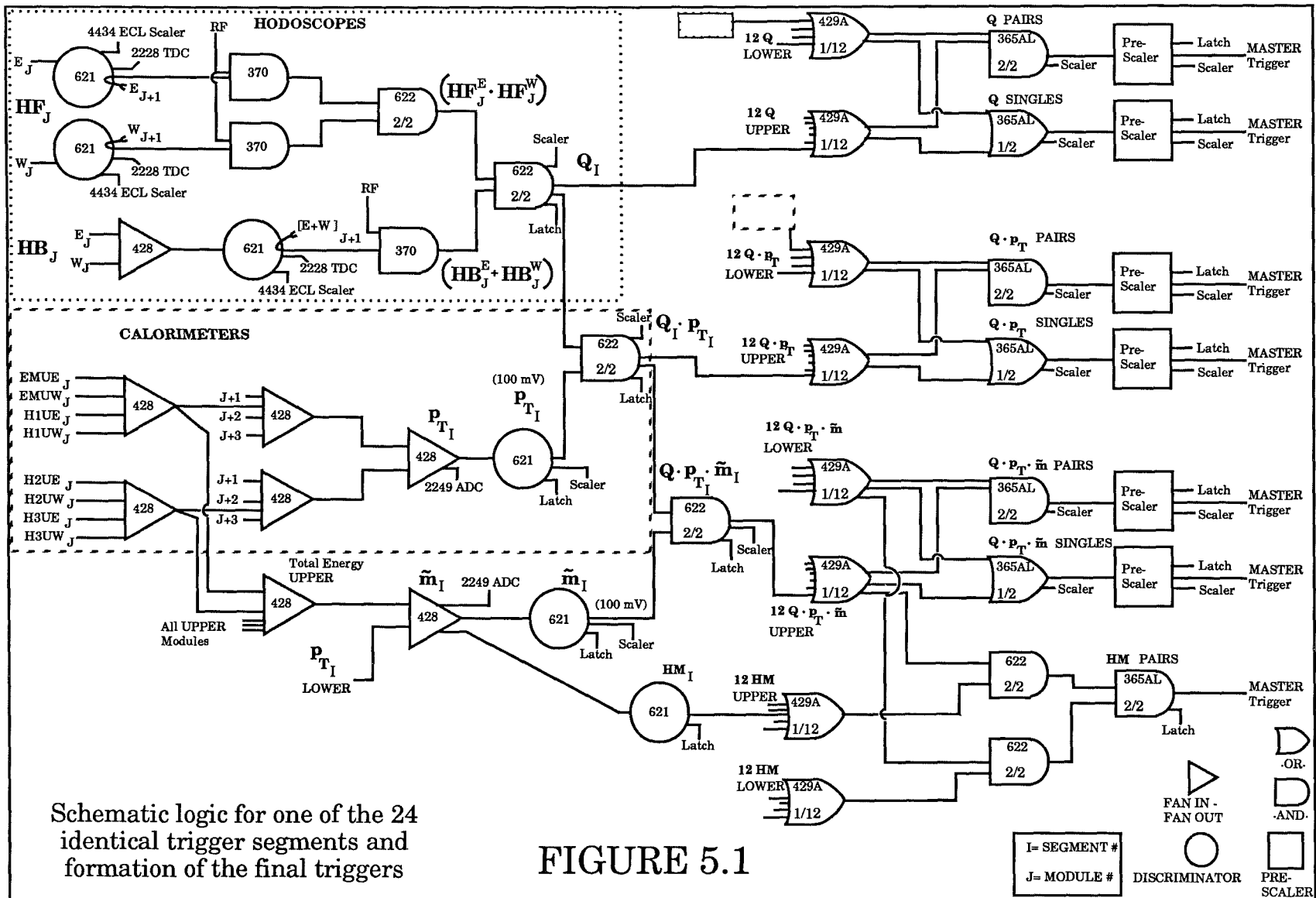
where HF and HB corresponds to the front and back hodoscopes, E and W for the east and west sides of the module, and k is the segment number. This final signal indicated the passage of a charged particle through adjacent front and back overlapping hodoscope modules numbered k+2 and k+3, from the center of calorimeter segment numbered k.

The transverse momentum ( $p_T$ ) signal was generated when a hadronic shower generated a pulse in a segment above a set threshold. The analog signal of a segment was proportional to the  $p_T$  of the hadron

and the discriminator threshold was set so as to indicate the presence of a hadron greater than  $2 \text{ GeV}/c \text{ } p_T$ .

### §5.2.2 Mass Trigger

As stated earlier, the effective mass of the dihadron state ( $M_{h_1 h_2}$ ) was approximated by the sum of the transverse momentum components of the two hadrons. To limit the electronics needed to cover all the pairs combinations (144) of the 12 upper and 12 lower calorimeter segments signals, the  $\tilde{m}$  mass signals were produced. For each segment this signal consisted of the  $p_T$  for a single particle in one calorimeter plus the total transverse momentum signal in the opposite calorimeter. The resulting analog signal of this sum was discriminated to produce 24 ( $\tilde{m}$ ) logic signals corresponding to a lower mass threshold of  $6 \text{ GeV}/c^2$  and 24 higher mass (HM) logics signals corresponding to a threshold of  $8.5 \text{ GeV}/c^2$ . A schematic diagram of the electronic logic of one of the 24 identical trigger segments is shown in Figure 5.1. The numbers inside of the symbols indicate the electronic model number and a coincidence level (if any).





### §5.2.3 Particle Pair Triggers

The particle pair triggers were formed from the four types of logic signals described in the previous section. The final pair triggers can be symbolically written as :

$$Q \cdot p_T, \quad Q \cdot p_T \cdot \tilde{m}, \quad Q \cdot p_T \cdot HM$$

where the pair signal for these trigger represents a coincidence between the upper and lower calorimeter signals and HM (high mass) is the mass trigger at the higher threshold. These pair signals are defined symbolically in the following way:

$$Q \cdot p_T = (Q_i \cdot p_{T_i})_{\text{upper}} \cdot (Q_j \cdot p_{T_j})_{\text{lower}}$$

$$Q \cdot p_T \cdot \tilde{m} = (Q_i \cdot p_{T_i} \cdot \tilde{m}_i)_{\text{upper}} \cdot (Q_j \cdot p_{T_j} \cdot \tilde{m}_j)_{\text{lower}}$$

$$Q \cdot p_T \cdot HM = \left[ (Q_i \cdot p_{T_i} \cdot \tilde{m}_i) \cdot (HM)_k \right]_{\text{upper}} \\ \cdot \left[ (Q_j \cdot p_{T_j} \cdot \tilde{m}_j) \cdot (HM)_k \right]_{\text{lower}}$$

where the subscripts i, j, k refer to the specific segments within each of the upper and lower calorimeters. Balancing the total number of each type of trigger required prescaling the  $Q \cdot p_T$  and  $Q \cdot p_T \cdot \tilde{m}$  triggers generally by factor of 128 and 2 respectively. The high mass trigger was not prescaled.

The finite shower containment and resolution of a calorimeter segment caused the  $Q \cdot p_T \cdot \tilde{m}$  trigger to be less than 100% efficient for hadron pairs less than 7.5 GeV/c<sup>2</sup> in mass. The  $Q \cdot p_T$  trigger on the other

hand was greater than 92% efficient at lower masses. The trigger efficiency for a particular mass was therefore defined as a ratio:

$$\epsilon_{\text{trig}} = \frac{N_{Q \cdot p_T \cdot \tilde{m}}}{N_{Q \cdot p_T}}$$

where  $N_{Q \cdot p_T \cdot \tilde{m}}$  is the number of  $Q \cdot p_T$  events which also set latches for the  $Q \cdot p_T \cdot \tilde{m}$  trigger while  $N_{Q \cdot p_T}$  is the number of  $Q \cdot p_T$  triggers. Table 5.2 lists the trigger efficiencies in two mass ranges. The other efficiencies were discussed in the previous chapters.

**TABLE 5.2**  
**Trigger Efficiencies**

<b>Mass Range</b> (GeV/c <sup>2</sup> )	<b>Efficiency</b>
7.0 – 7.5	83 ± 8.8 %
> 7.5	100 ± 8.0 %

### **§5.3 Data Acquisition**

Digitized information was stored in the CAMAC<sup>62</sup> electronics when the event triggers were generated. Then electronic interrupts were generated, signaling that the PDP-11 computer system should read out this information on the experimental and beam instrumentation, and write it onto magnetic tape for final storage.

#### **§5.3.1 Experiment Monitoring**

The experiment utilized a PDP-11 computer running the Fermilab MULTI<sup>63</sup> program dedicated to event data acquisition and a VAX-780 computer used for quality assessment of the experimental data through real-time analysis of a fraction of the accepted events. A PDP-11/84 linked to a PDP-11/44, allowed control of devices and monitoring of instruments critical to the integrity of the beam by operating the system known as EPICS<sup>64</sup>.

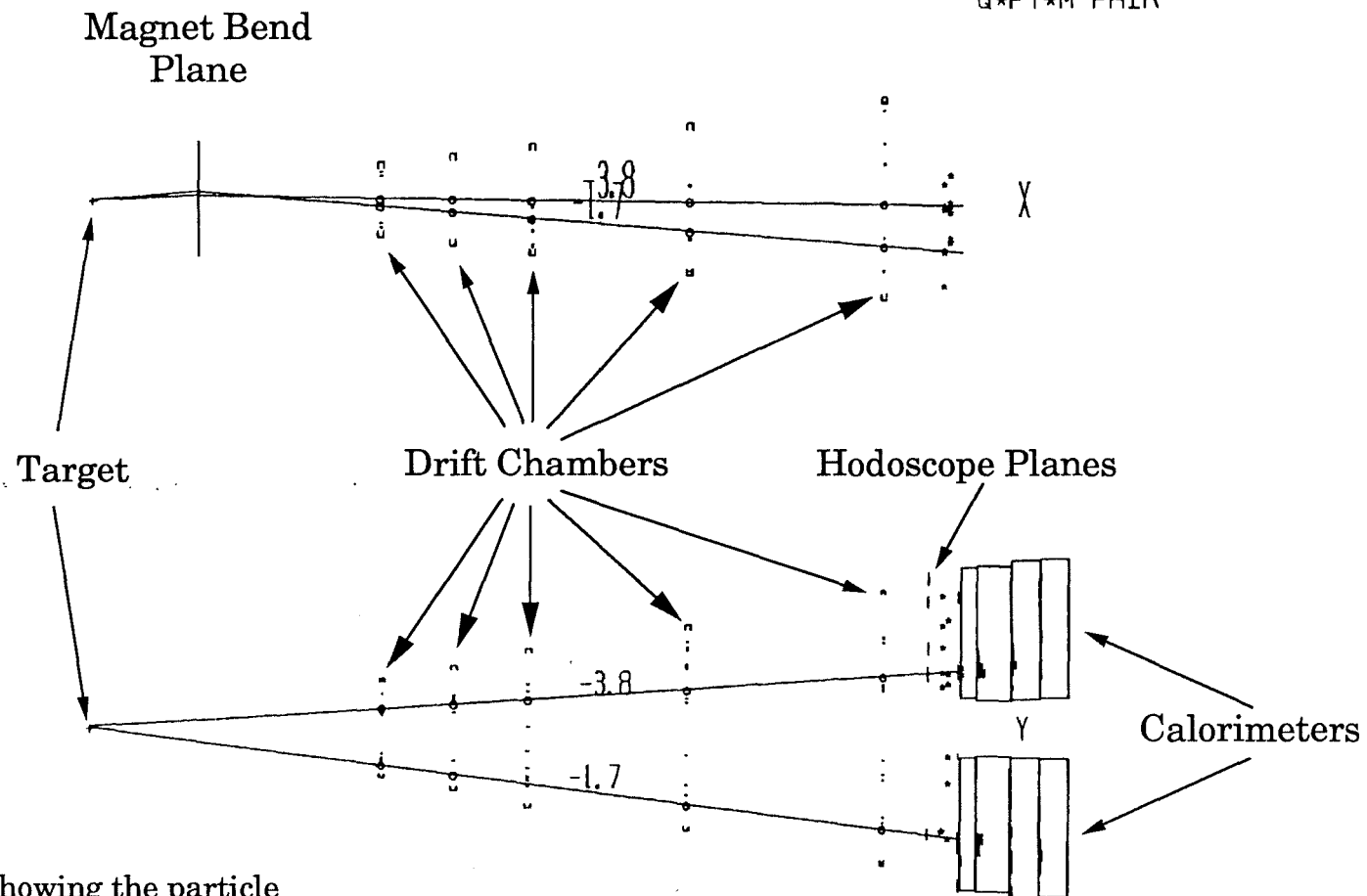
The MULTI program controlling the data acquisition, sent copies of a small fraction of the events to the VAX-780 computer. An online event processing program (CONSUMER) then allowed the user to produce histograms, event displays and distributions of the data. Histograms of the ADC's, scalars and latches were produced to monitor the performance of the calorimeter and the hodoscope. The event display utilizing the results of a pattern recognition routine produced plots of particle tracks, hodoscope and calorimeter pulse heights, and verified the track

momentum as in the example shown in Figure 5.2. In addition wire hit histograms were used to monitor the cabling.

### §5.3.2 Data Readout Interrupts

Two types of interrupts (A and B) were generated by the trigger electronics that indicated that the computer was to read in specific sets of digitized information from CAMAC. The A interrupt sequence was generated when the event triggers were satisfied, within the 20 second beam spill. Prior to the beam spill 16 A-interrupts were automatically generated to record the pulse heights of the hodoscopes and calorimeter modules so that this value without beam (called a pedestal) could be subtracted from the beam spill readings to get the correct values associated with actual particles in the events. Table 5.3 lists the A-interrupt event record information. The B-interrupt was initiated at the end of each beam spill where information listed in Table 5.4 was read out for the spill record. This information includes the detector information as well as the beam monitoring information.

A INTERRUPT  
 RUN 1803 EVENT 329  
 Q\*PT\*M PAIR



Event Display showing the particle tracks, magnetic bending, hodoscope signals and energy deposition in the calorimeters.

FIGURE 5.2

## TABLE 5.3

### A - interrupt Event Record Information

Data Output	Readout Electronics
Wire Chamber Drift times	LeCroy 4290 TDC
Hodoscope Phototubes pulse heights	LeCroy 2285 ADC
Calorimeter Phototubes pulse heights	LeCroy 2249 ADC
All Logic Signals	EG & G C124 Latches
Q segments	
$p_T$ segments	
$\tilde{m}$ segments	
Pair Logic segments	
Final Trigger type signals	EG & G C124 Latches
Event numbers and luminosity counts since the last event	Jorway Scalers

## TABLE 5.4

### B- interrupt Spill Record Information

All the information was read from Jorway Scalers  
as accumulated counts for each device

Data Output
Power supply currents from the analyzing and beamline magnets
Ionization chamber
Luminosity monitors
Final Trigger types prescaled
Final Trigger types unprescaled
Q segments
$p_T$ segments
$\tilde{m}$ segments
$Q \cdot p_T$ segments
$Q \cdot p_T \cdot \tilde{m}$ segments

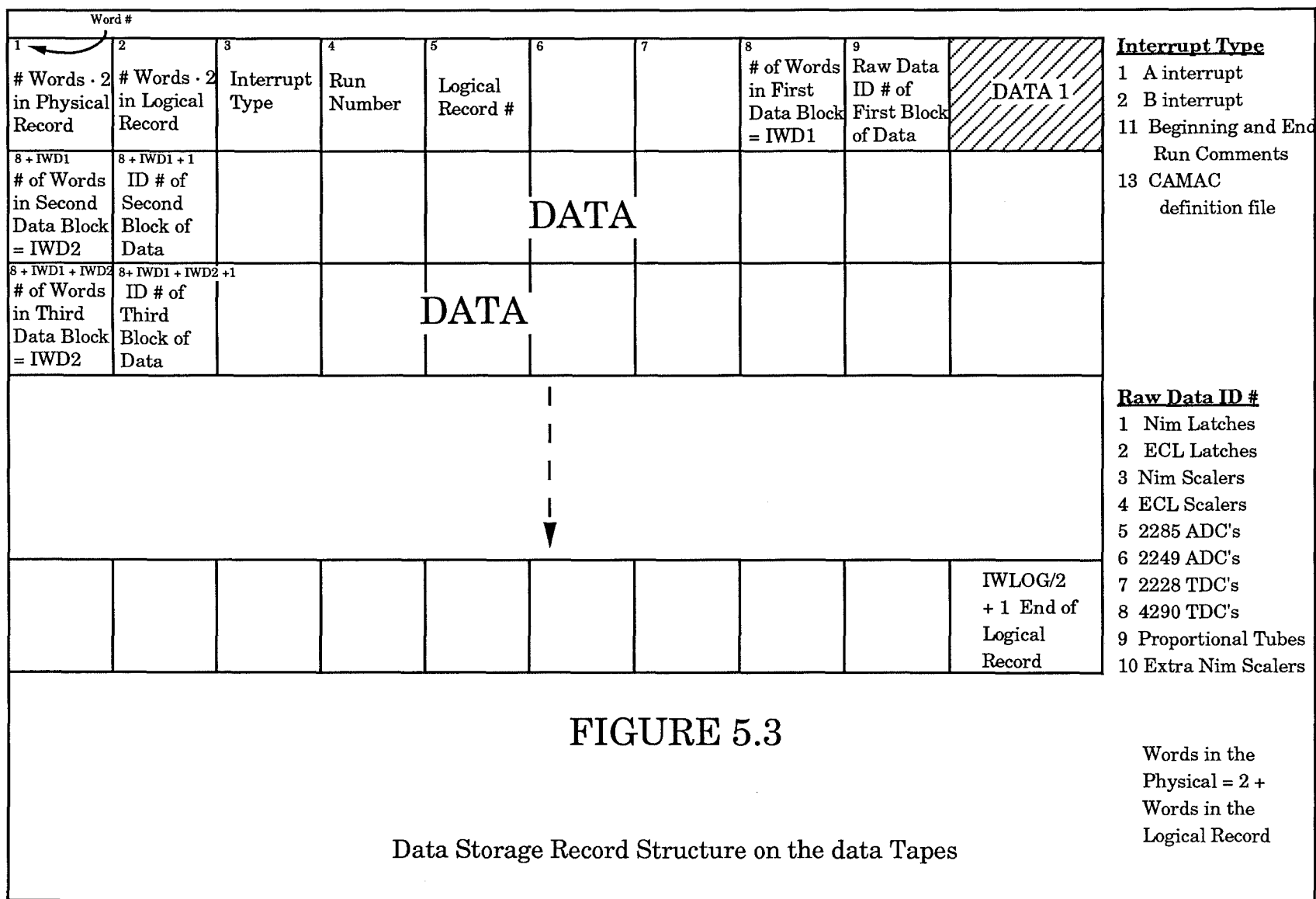
### §5.3.3 Data Storage

The raw data analyzed in this work totaled approximately  $20 \times 10^6$  event records written on 455, **6250 bpi** magnetic tapes.

Various data acquisition modes operated throughout the experiment. Low intensity beam periods for the detector alignment and instrumentation calibration as well as periods with the spectrometer magnet currents set to zero (called "straight through runs") were done to study the systematics of the instruments, the effect of the analyzing magnetic fields, and study the alignment of the wire chambers to the target in the  $\mathbf{x}$  direction. To collect information on the various background radiation sources in the detector, target in place data and comparative target out data were taken, along with the the target scans discussed in earlier chapters.

The data structure stored on the magnetic tape is shown in Figure 5.3.





## CHAPTER 6

### DATA PROCESSING

#### **§6.1 Track Recognition and Reconstruction**

The process of track identification and track reconstruction was done using the high speed vector computing processors of the CDC CYBER-205 and the ETA-10 computers. These computers using a vectorized algorithm<sup>65</sup>, greatly improved the data processing speed over a scalar algorithm. The vector algorithm had an average processing time of approximately 11 msec/event for the ETA-10 (model E) as compared to nearly 5 sec/event for an optimized scalar code capable of similar reconstruction efficiency on a VAX 11/780 computer. The two codes produced similar results.

The TDC information from the drift chambers giving the positions of hits in the 20 sense wire planes was used to search for and select particle tracks in the data. Candidate tracks with a  $p_T > 1.0$  GeV/c were first selected from two dimensional searches in each of the four projections (x-z, y-z, u-z, v-z). Each of the sense wire planes were grouped into "cells", (three physical wires per cell ; i.e. 193 y cells, 86 x cells, 118 u cells, and 118 v cells). These cells were used to create lookup tables comprised of all the possible cell combinations that could form a valid track. Tracks were then identified by comparing the pattern of hits in the data with groups of cell

combinations that contained hits and consequently defined previously calculated tracks. The tracks in the cells were unfolded into real wire locations where the slopes of the track and the track target intercepts are calculated. Next, these two dimensional tracks, from the four different views were used to form three dimensional tracks. The resulting hit pattern was fitted to a straight line using the drift time information from the TDC's to further specify the spatial distance from the wire. The ambiguity in determining which side of the wire that the particle passed was resolved by using the side that best met the criterion for an acceptable fit. The algorithm requirements included 15 hits out of a possible 20, with 3 out of 4 views (x, y, u, v) having at least 3 out of 5 hits and at least 2 hits in the remaining views. The  $\chi^2$  per degree of freedom was required to be less than 7. The parameters needed to fit the tracks and calculate a  $\chi^2$  were done simultaneously for all the tracks in the vector algorithm mode and the tracks that passed the  $\chi^2$  cut were tagged. The tracks that failed were flagged for deletion. In addition to the track information, ADC, scaler, and latch information for each event and trigger pedestal events and spill records were written to the data summary tapes (DST's).

The reconstruction efficiency per track of this algorithm was calculated to be  $90.4 \pm 0.5\%$ , the error being statistical. Because the operating conditions of the wire chambers (and therefore the wire chamber efficiencies) varied over the duration of the data taking, the reconstruction efficiencies of the two track events verses the single track events also varied slightly over this period resulting in a variation of the reconstruction efficiency. The efficiency of the algorithm was coupled to

the plane efficiency of the wire chambers (see Table 4.5). To account for this effect, the vector algorithm used for the initial track reconstruction was compared to another independent track reconstruction program which used a less restrictive  $\chi^2$  requirement (so that it would be 100% efficient). Data samples for each target were passed through both programs and then subjected to event selection criterion. The reconstruction efficiency was the ratio of the remaining events after the selection process. The two track reconstruction efficiencies for different targets and data samples are listed in Table 6.1. For each of the 455 raw data tapes a DST was written. The percentage of events surviving the track selection per target is listed in Table 6.2.

**TABLE 6.1**  
**Two Track Reconstruction Efficiencies**

Target	Efficiencies
Beryllium	0.594
Aluminum	0.786
Iron	0.611
Tungsten (early data)	0.640
Tungsten	0.585

**TABLE 6.2**  
**Event Selection percentages  
for the Data Summary Tapes**

Target	DST events / Raw data events %
Beryllium	52
Aluminum	61
Iron	60
Tungsten	41

## **§6.2 Track Momentum Calculation**

The track momentum was calculated using the results of the track reconstruction downstream of the magnets, the target track intercepts, the target position and the deflection of the track due to the known magnetic field. The track reconstruction results included the particle trajectory slopes in the x-z (horizontal) and y-z (vertical) planes and their intercepts at  $z = 0$ , the target location. The magnet bend was in the horizontal plane corresponding to a  $P_t$  of  $\pm 1.16$  GeV/c . The  $\pm$  sign corresponds to the charge of the deflected particle. The particle was assumed to bend at the bend point of the magnet system in the horizontal plane. The bend plane was determined from detailed Monte Carlo calculations using measured magnetic field maps.

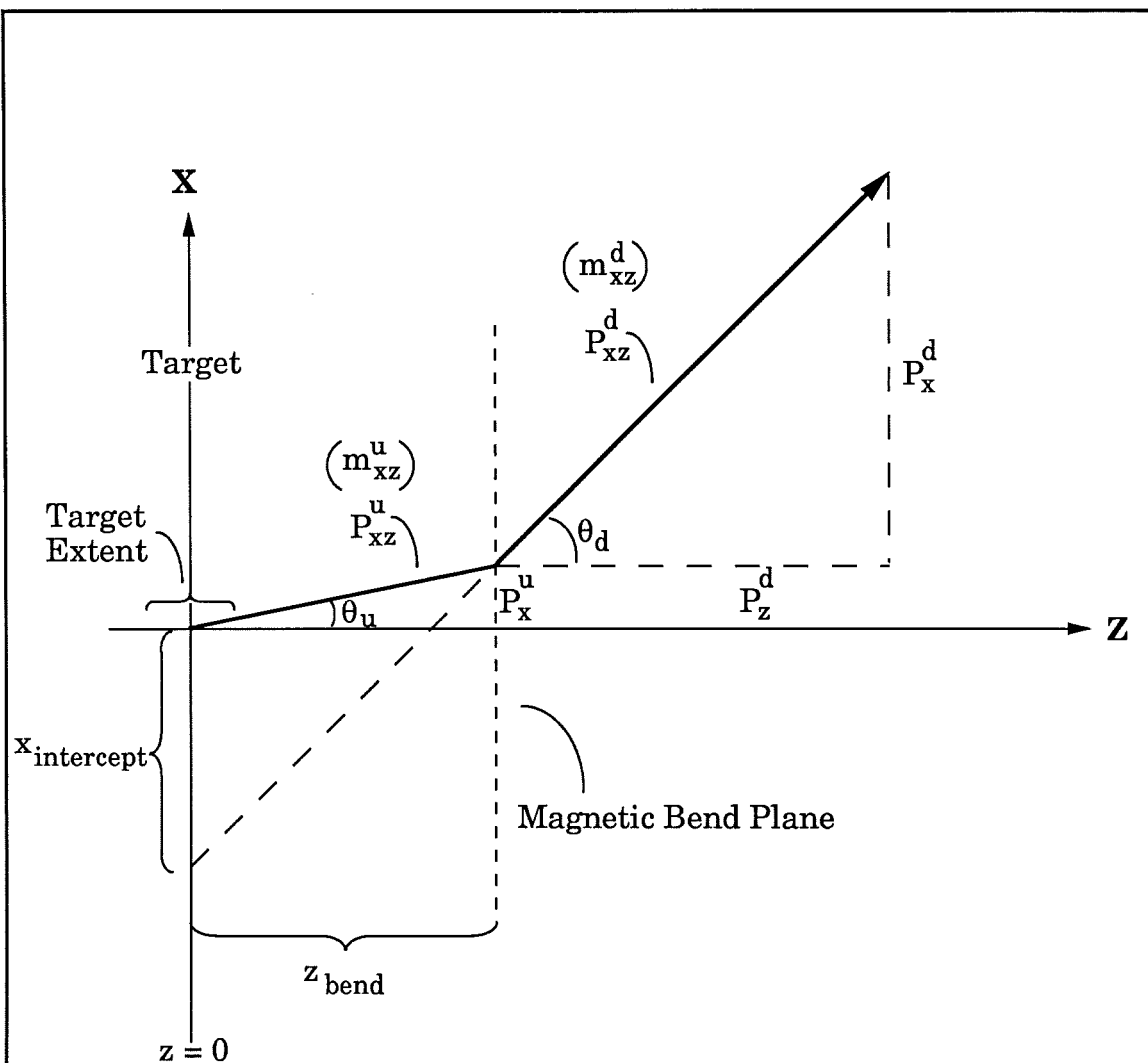
Figure 6.1 presents an illustration of the pertinent variables necessary for the momentum calculations. The interaction was assumed to occur at the target center and the momentum components are written:

$$P_x^d = P_x^u + P_t \quad (6.1)$$

$$\left(P_{xz}^u\right)^2 = \left(P_{xz}^d\right)^2 = \left(P_x^d\right)^2 + \left(P_z^d\right)^2 = \left(P_x^u\right)^2 + \left(P_z^u\right)^2 \quad (6.2)$$

$$P_x^d = \left(m_{xz}^d\right) P_z^d \quad (6.3)$$

where m's are the slopes and P's are the momentum, with  $P_t$  the momentum "kick" of the magnet.



: Scale exaggerated with respect to  $Z$

FIGURE 6.1

Illustration of the track momentum parameters with the positions of the target and bending plane. The slopes are the variables labeled  $m$ . The subscripts  $u$  and  $d$  stand for upstream and downstream.

Using the measured downstream slopes  $\left(m_{xz}^d\right)$ , the known bend point  $(z_{\text{bend}})$  and target intercept  $(x_{\text{intercept}})$  leads to the components of the momentum:

$$P_x^u = \left(m_{xz}^u\right) P_z^u, \text{ where } \left(m_{xz}^u\right) = \frac{\left(m_{xz}^d\right) z_{\text{bend}} + x_{\text{intercept}}}{z_{\text{bend}}} \quad (6.4)$$

$$P_y^u = \left(m_{yz}^u\right) P_z^u, \text{ where } \left(m_{yz}^u\right) = \left(m_{yz}^d\right) = \text{the } yz \text{ slope.} \quad (6.5)$$

$$P_z^u = \frac{-P_t \left(m_{xz}^u\right) \left[1 + \left(m_{xz}^d\right)^2\right]}{\left(m_{xz}^u\right)^2 - \left(m_{xz}^d\right)^2} + \frac{P_t \left(m_{xz}^d\right) \sqrt{\left(m_{xz}^u\right)^2 + \left(m_{xz}^d\right)^2 + \left(m_{xz}^u\right) \left(m_{xz}^d\right) + 1}}{\left(m_{xz}^u\right)^2 - \left(m_{xz}^d\right)^2} \quad (6.6)$$

The errors in the calculation are mainly due to the resolution of the drift chambers and the finite length and width of the target. Table 6.3 lists the calculated errors in the momentum for the different targets. The terms in  $p^2$  are due to the  $x$  intercept error caused by the finite target width and the drift chamber resolution, while the term in  $p$  is due to the target length.



**TABLE 6.3****Momentum Resolution Error per Target**

Target	$\Delta p$
Beryllium	$2.8 \times 10^{-4} p^2 + 5.26 \cdot 10^{-3} p$
Aluminum	$2.7 \times 10^{-4} p^2 + 5.12 \cdot 10^{-3} p$
Iron	$2.54 \times 10^{-4} p^2 + 2.16 \cdot 10^{-3} p$
Tungsten	$2.79 \times 10^{-4} p^2 + 1.23 \cdot 10^{-3} p$

**§6.3 Data Summary File Event Selection**

Further compaction of the data led to data summary files (DSF), which were stored on disk for convenience of analysis. The events within these file were selected from the DST's with pedestals subtracted, and with the calculated energy deposited for each module and segment of the calorimeter. The latch information and the track momentum were also included in the output's compact form and each DSF corresponded to events from a single DST. Table 6.4 presents a summary of the event selection for the data summary files. The DST's corresponding to periods when the operating conditions were not ideal were not included in this DSF data sample, hence the difference between the number of DST's and

the DSF's. As stated in the last chapter, the pair triggers mentioned here are:  $Q \cdot p_T \cdot \tilde{m}$  and  $Q \cdot p_T \cdot HM$ , and both these triggers are included in the numbers listed in Table 6.4.

**TABLE 6.4**  
**Event Selection summary**  
**for the Data Summary Files**

<b>Target</b>	<b>No. of Tapes</b>	<b>No. of Files</b>	<b>DSF Events</b>	<b>Number of Pair Triggers</b>
	<b>DST's</b>	<b>DSF's</b>	<b>(x 10<sup>6</sup>)</b>	<b>(x 10<sup>6</sup>)</b>
Beryllium	107	67	1.580	1.450
Aluminum	46	29	0.941	0.762
Iron	76	66	1.800	1.680
Tungsten	216	71	1.090	0.861
<b>Totals</b>	445	233	5.411	4.753

## CHAPTER 7

### THE DATA ANALYSIS

#### §7.1 Introduction

The analysis described here determined the angular dependence of the production of massive dihadrons using data for three charge states in a mass range of 7 to 15 GeV/c<sup>2</sup>. The description of the criteria for selecting the high p<sub>T</sub> dihadron events pertinent to determining the charge, mass and angular dependence is presented in this chapter. The definitions of the measured quantities, relations derived from measured quantities, and the limits on those parameters are given.

#### §7.2 The Measured Variables

The six dimensional phase-space of the dihadron system can be described by a complete set of variables chosen to be the mass of the dihadron system ( $M$ ); its transverse momentum ( $\vec{p}_T : \vec{p}_{T_1} \text{ \& } \vec{p}_{T_2}$ ); the rapidity of the dihadron system ( $Y$ ) in the proton-nucleon center of mass frame; the cosine of the polar angle ( $\cos\theta^*$ ) between the dihadron axis and the beam direction in the rest frame of the dihadron system; and the azimuthal angle ( $\phi^*$ ) of the plane defined by the beam direction and the dihadron axis in that frame. If you label the two hadrons (1 and 2) in the dihadron system, then the mass ( $M$ ) can be written:

$$M = \sqrt{\left(E_1 + E_2\right)^2 - \left(\vec{P}_1 + \vec{P}_2\right)^2} \quad (7.1)$$

where E and P are the energy and momentum.

The magnitude of the net transverse momentum is:

$$p_T = \sqrt{\left(P_{1x} + P_{2x}\right)^2 + \left(P_{1y} + P_{2y}\right)^2} \quad (7.2)$$

where the components of the three vectors are  $P_x$ ,  $P_y$ ,  $P_z$ , with z along the beam axis.

The longitudinal rapidity is a quantity that aids in describing the motion of the hadron-hadron system in the proton-nucleon center-of-mass frame and can be defined as:

$$Y = \frac{1}{2} \ln \left[ \frac{\left(E_1 + E_2\right) + \left(P_{1z} + P_{2z}\right)}{\left(E_1 + E_2\right) - \left(P_{1z} + P_{2z}\right)} \right]. \quad (7.3)$$

Rapidity intervals are invariant to boosts along the z-axis, the axis defining the longitudinal momentum.

The determination of the parton scattering angle is inexact. The leading particle effect, where  $\langle z_{\text{trig}} \rangle \approx 0.9$ , means that the angles of the two hadrons are parallel to the quarks, thus  $\theta^*$  can be derived from the two leading hadrons. Although the intrinsic momentum of the hadrons is not known, the main source of inaccuracy in the angle then is due to the unequal hadron fragments. So the ambiguity in  $\theta^*$  is due to unequal transverse momentum. The parton-parton scattering angle ( $\theta^*$ ) is between

the dihadron axis and the beam direction in the rest frame of the dihadron massive state. The polar angle for each particle can be defined:

$$\cos\theta_1^* = \frac{P_{1z}^*}{|\vec{P}_1^*|} \quad \text{and} \quad \cos\theta_2^* = \frac{P_{2z}^*}{|\vec{P}_2^*|} \quad (7.4)$$

where  $P_z^*$  and  $P^*$  are the  $z$  component and the total momentum respectively of an individual hadron in the dihadron system. The average of these angles is used.

### **§7.3 The Integrated Luminosity**

In order to calculate the cross section from a measured number of experimental events, the integrated luminosity must be known. In general the luminosity can be defined as :

$$\mathcal{L} = \frac{N_{\text{events}}}{\sigma} \quad (7.5)$$

where  $N_{\text{events}}$  is the number of events and  $\sigma$  the reaction cross section. The integrated rate of proton-nucleon interactions therefore is used as a normalization factor in determining the cross section. Alternatively the luminosity can be determined from the known properties of the target materials and the measured number of incident beam particles, including the beam targeting fraction accounting for the beam depletion in the target. Specifically the luminosity can be evaluated as:

$$\mathcal{L} = N_b F \int_0^\ell \frac{N_{\text{sc}}}{V} e^{-z/\lambda_T} dz \quad (7.6)$$

so that

$$\mathcal{L} = N_b F \lambda_T \frac{N_{sc}}{V} \left[ 1 - e^{-\ell/\lambda_T} \right] \quad (7.7)$$

where:

$N_b$  = number of incident beam particles

$F$  = beam-target fraction as defined in Chapter 4 (eq. 4.1)

$\lambda_T$  = proton interaction length for the target material

$\frac{N_{sc}}{V}$  = number of target scattering centers per volume

$\ell$  = target length

The dimension, material composition and properties of the target directly determine the last three variables listed above. The incident beam flux  $N_b$  was measured by an ion chamber and the beam targeting fraction was measured by luminosity scintillation counters. The counters described previously in Chapter 4, were calibrated using horizontal target scans and a measurement of the total beam flux. The total number of counts accumulated from each set of luminosity counters was parameterized as:  $N_c = C [N_b \cdot (F + B)]$  where  $C$  depends on the solid angle of the counters and the cross section for producing particles at the angles subtended by the counters, and  $B$  is the background fraction.

The beam target fraction  $F$  was calculated as:

$$F = \int_{x_0 - \frac{w}{2}}^{x_0 + \frac{w}{2}} f(x, x_b) dx \quad (7.8)$$

using the horizontal distribution of the beam intensity  $f(x, x_b)$  which is parameterized as a gaussian distribution centered at  $x_b$ . In this formula  $w$  is the width of the target and  $x_0$  is the target center.

The systematic error in the calculation of the luminosity was due to the calibration of the ion chamber ( $\pm 2\%$ ) and due to the variations in the background from different target scans. The errors were estimated to be less than 4% for the beryllium target and less than 2% for each of the three other targets. Table 7.1 list the total integrated luminosities correcting for the attenuation of the incident beam in each of the four targets.

**TABLE 7.1**  
**Total Integrated Luminosity**

Target	Protons on Target	$\mathcal{L}$ / Nucleus (nanobarns <sup>-1</sup> )	$\mathcal{L}$ / Nucleon (nanobarns <sup>-1</sup> )
Beryllium	$(2.65 \pm 0.06) \times 10^{12}$	$1.774 \times 10^3$	$1.598 \times 10^4$
Aluminum	$(2.32 \pm 0.04) \times 10^{11}$	$2.258 \times 10^2$	$6.090 \times 10^3$
Iron	$(1.60 \pm 0.04) \times 10^{12}$	$2.756 \times 10^2$	$1.539 \times 10^4$
Tungsten	$(2.36 \pm 0.06) \times 10^{12}$	$3.534 \times 10^1$	$6.497 \times 10^3$

#### **§7.4 Background Study**

Background contamination of the data sample was due mainly to interactions produced near the target, such as in the air around the target or in the target holder. Even though the experiment triggered on hadron pairs, it was also considered possible for uncorrelated single hadrons from two distinct interactions to mimic a high  $p_T$  dihadron event.

To determine the background from non-target materials, data were taken periodically throughout the experiment, with the target removed from the target station and also with the entire station removed. These data were analyzed in the same way as the target data, and the percentage of the events was determined based on the beam flux for each target type. It was found that less than 3% of the beryllium events and less than 1.5% of the events from the other targets were background of this type, totaling less than 95,000 events.

Single hadron signals from the upper calorimeter were compared to time delayed signals of single hadrons from the lower calorimeter. The coincidence rates for these signals were recorded for delay times that were consistent with a dihadron trigger logic signal. This coincidence rate indicating background events of this type was found to be less than 0.1%.

#### **§7.5 Event Selection Criteria**

The final data set included all events that met the minimum requirements for the analysis. These requirements were based on constraints determined from the characteristics of the detector, and from



limitations placed upon the values of the measured quantities (called "cuts"). The following constraints were adhered to in the selection of individual particle tracks and pairs of tracks:

(a) Target Vertex Position : Individual tracks were required to intercept the target in the non-bend view (which is along the y-axis). The position of the track at the target ( $y_{tgt}$ ) must intercept the target within a range of values relative to the nominal targeting position (see Fig.4.2) given by:

$$-2.0 \text{ cm} \leq y_{tgt} \leq 1.6 \text{ cm}$$

Figure 7.1 shows the distribution of the intercept of tracks at the tungsten target. The beam was positioned so that the interactions occurred approximately 1.6 cm vertically below the top of the target. The distribution is centered at  $\approx -0.17$  cm with limits on the vertex applied to the data as shown.

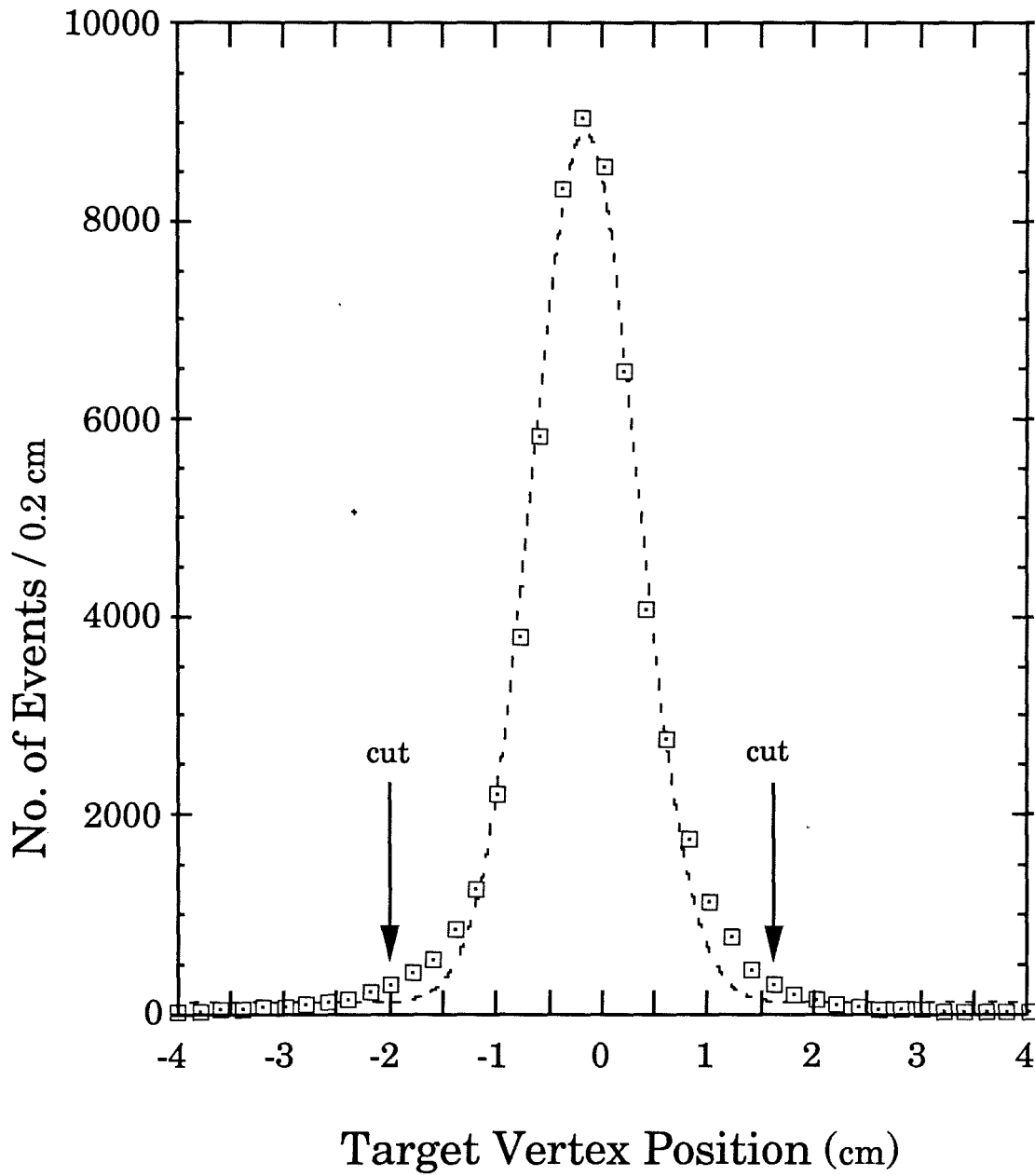


FIGURE 7.1

The track y-vertex position distribution centered around the nominal targeting location. The curve is a gaussian distribution fit to the data.

(b) Calorimeter Fiducial Volume : The y position of a track at the front face of the calorimeter was restricted to a region where the energy shower of the impinging particle was fully contained by the calorimeter. This requirement made it possible to eliminate those tracks that were identified by the square geometry of the drift chambers, but were not in the trigger because they did not project to a fiducial volume within the trapezoidal dimensions of the calorimeter. The containment volume was therefore determined by the y position on the front face of the calorimeter and the range of the azimuthal angle measured from the beam centered y-axis on the calorimeter front face. The limits of the y position on the bottom calorimeter were:

$$-150.0 \text{ cm} \leq y_{\text{calor}} \leq -40.0 \text{ cm}$$

and the limits of the y position on the top calorimeter were:

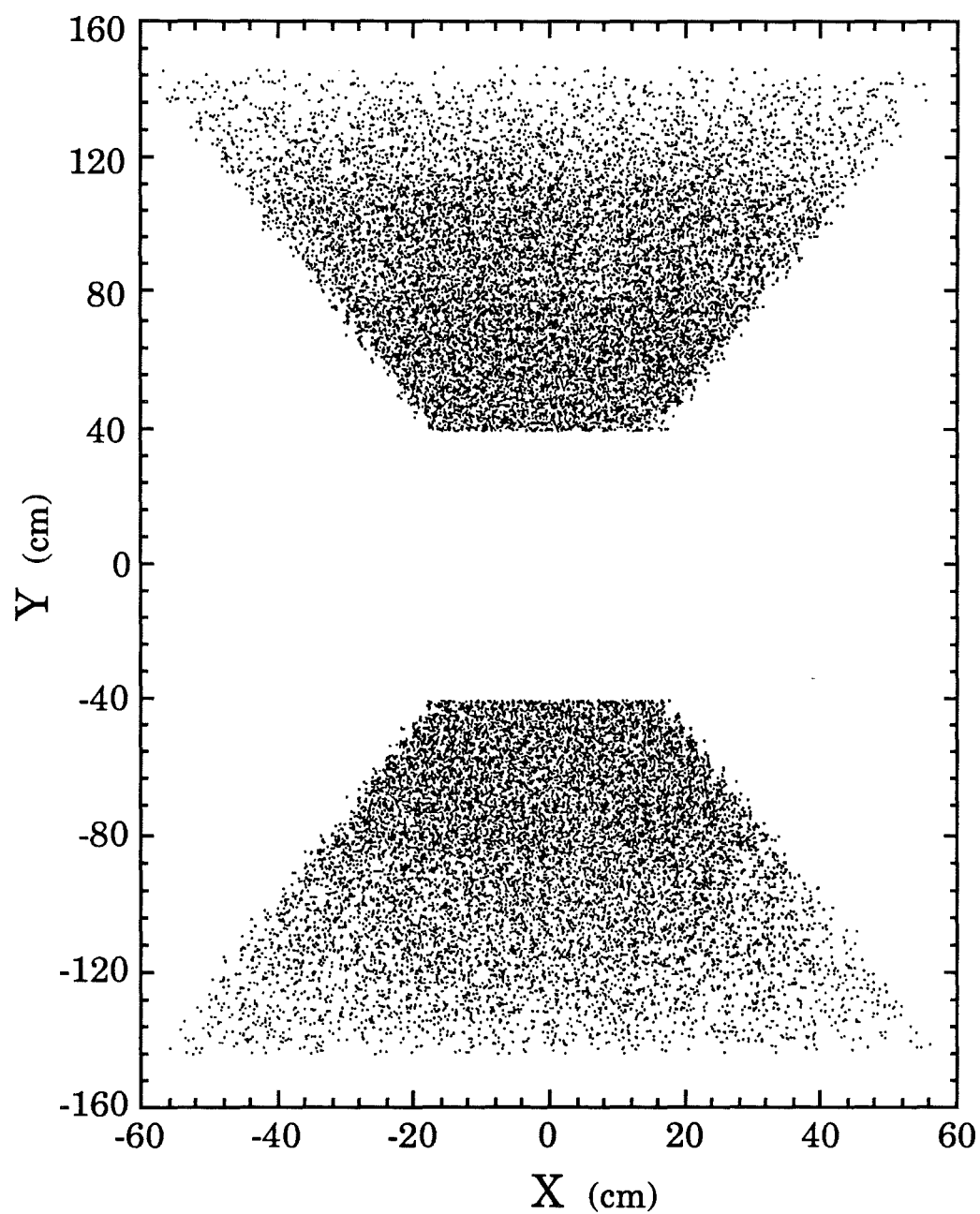
$$40.0 \text{ cm} \leq y_{\text{calor}} \leq 150.0 \text{ cm} \quad ,$$

while the range of the azimuthal angle was:

$$|\phi_{\text{calor}}| \leq 22.0^\circ$$

Note that the actual physical size of the calorimeter ranges from nearly 33 cm to 177 cm in  $|y_{\text{calor}}|$  and  $25.3^\circ$  for  $|\phi_{\text{calor}}|$ .

Figure 7.2 shows a distribution of intercept positions for tracks from unlike-sign dihadrons at the front face of the calorimeter. The trapezoidal shape reflects the constraints discussed above.



Calorimeter Hit Distribution

FIGURE 7.2

The distribution of hits for tracks of unlike sign charged dihadrons that intercept the front face of the calorimeter.

The following cuts on the measured quantities were applied to insure the validity of the accepted dihadron events.

(a) Momentum : The y component of the momentum of a particle was restricted to make sure that the particle's transverse momentum was above the hardware trigger threshold. Since  $p_y \approx p_T$ , this sets a limit on  $p_T$ . Thus :

$$|p_y| \geq 2.0 \text{ GeV}/c$$

(b) Energy and Track Momentum Comparison: The track momentum  $\mathbf{p}$  was reconstructed from the drift chamber information, while all of the hadronic energy in the fiducial volume of the calorimeter provides for a measurement of the energy of a good event. However spurious showers, photon conversion upstream, and even bad track reconstruction could lead to tracks of very large momentum but negligible energy deposition in the calorimeter. So the discrepancy between the energy and the momentum was limited for acceptable tracks. Figure 7.3 shows a distribution for identified tracks.

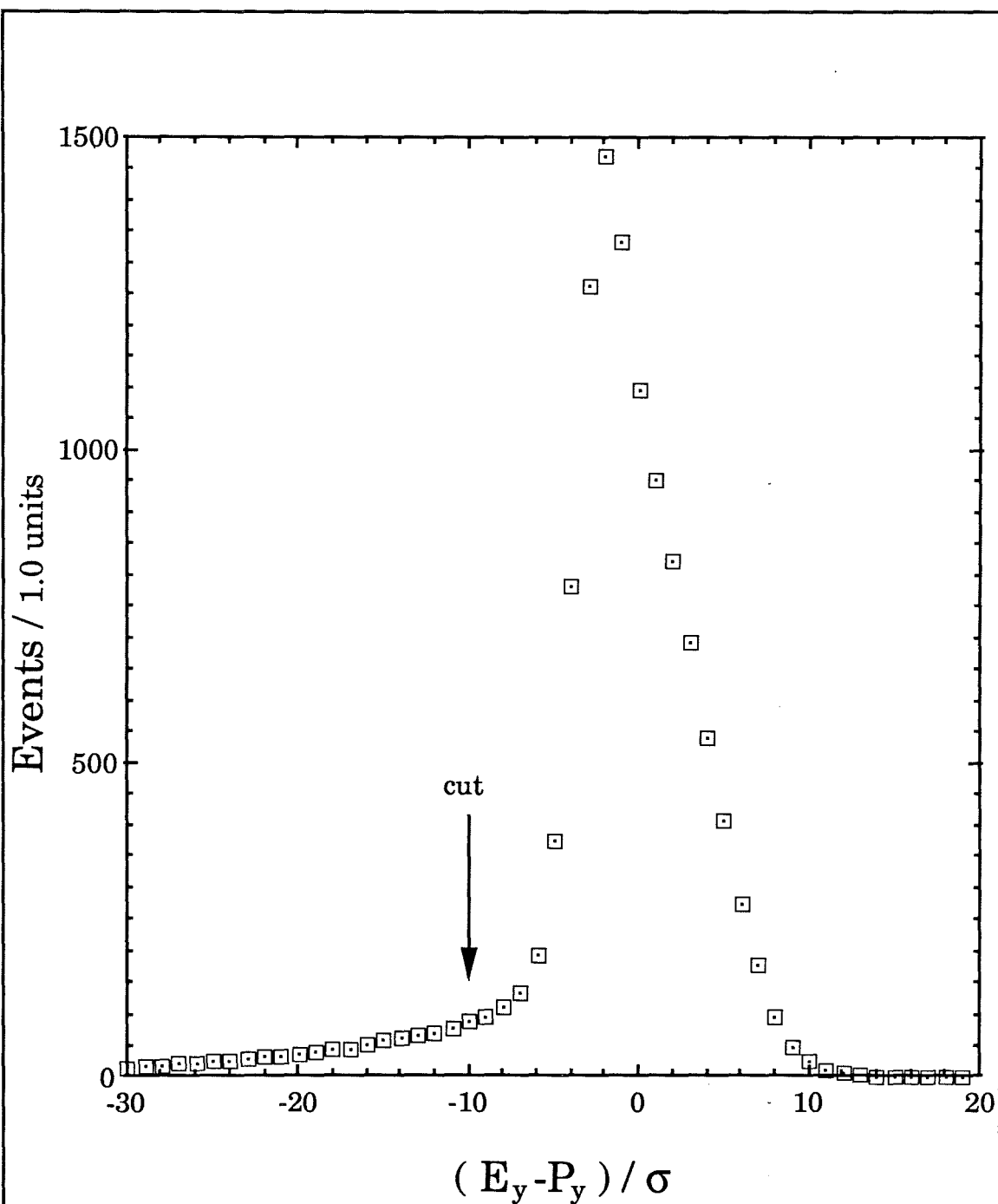


FIGURE 7.3

The distribution for identified tracks comparing the track momentum and corresponding energy deposition in the calorimeter.

The required limit on the comparison of energy and momentum for an energy segment as indicated in the last figure was:

$$\frac{E_y - p_y}{\sigma} \geq -10.0$$

where the  $\sigma = \sqrt{\Delta E^2 + \Delta p^2}$ . The  $\Delta E$  is the energy resolution of the calorimeter discussed in Chapter 4 and the  $\Delta p$  is the momentum resolution error. Note that for this calculation  $\Delta p = 2.7 \times 10^{-4} E^2$  (GeV) and uses the (more accurate) energy in the calorimeter instead of the momentum because those tracks with very high momentum are not as well reconstructed leading to a very large  $\Delta p$ .

(c) Mass of the Hadron Pairs : As stated in Chapter 5, the effective mass of the dihadrons was approximated by the sum of the transverse momentum of the two hadrons. The hardware threshold for the low mass trigger was set at 6 GeV/c<sup>2</sup> while the high mass trigger threshold was set at 8.5 GeV/c<sup>2</sup>. The selected hadron pairs therefore were chosen with a mass greater than this lowest hardware threshold. Namely for the low mass threshold:

$$M \geq 7.0 \text{ GeV}/c^2$$

Charge dependent events selected by dihadron mass are shown in Figure 7.4. The events are collected in 500 MeV bins and the low mass threshold is indicated.

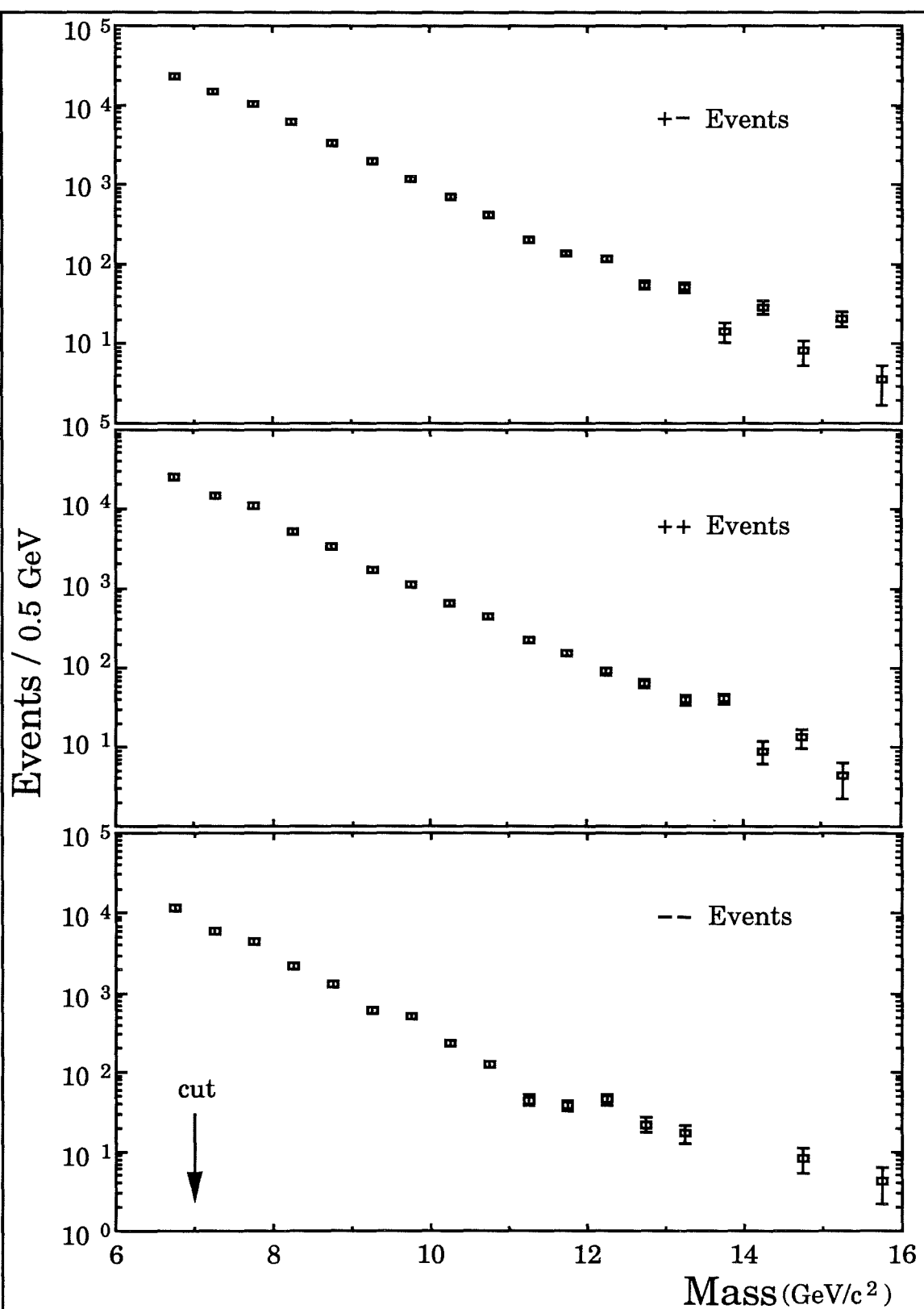


FIGURE 7.4

Event selection by hadron pair mass for the three different charge states.



(d) Electron/Hadron Energy Ratio : Particle energy deposition was studied to ensure that energetic electrons did not mimic hadron events. The  $\pi^0$  mesons produced in the target, decay to two photons in nearly one femto-second. These photons pass undeflected through the magnetic field. If one of these photons converts to an electron-positron pair on a chamber window, a track would be reconstructed, pointing back to the target in the  $\mathbf{x}$ -plane and be interpreted as having essentially an infinite momentum and  $p_T$ . The observed calorimetric energy would be the  $\pi^0$  energy. For a given track, a limit was placed on the ratio of the energy deposited in the electromagnetic segment of the calorimeter ( $E_{em}$ ), to the total energy deposited for that calorimeter segment ( $E_{calo}$ ). All the electron energy would be expected to be totally contained in the electromagnetic portion of the calorimeter. Thus it was possible to reject tracks by imposing the following requirement on this ratio:

$$\frac{E_{em}}{E_{calo}} > 0.98$$

A distribution of events testing the electron simulated hadron showers is shown in Figure 7.5. Events clustered around zero and spanning the distribution to nearly .99, indicate minor electromagnetic energy deposition and therefore are considered acceptable hadrons.

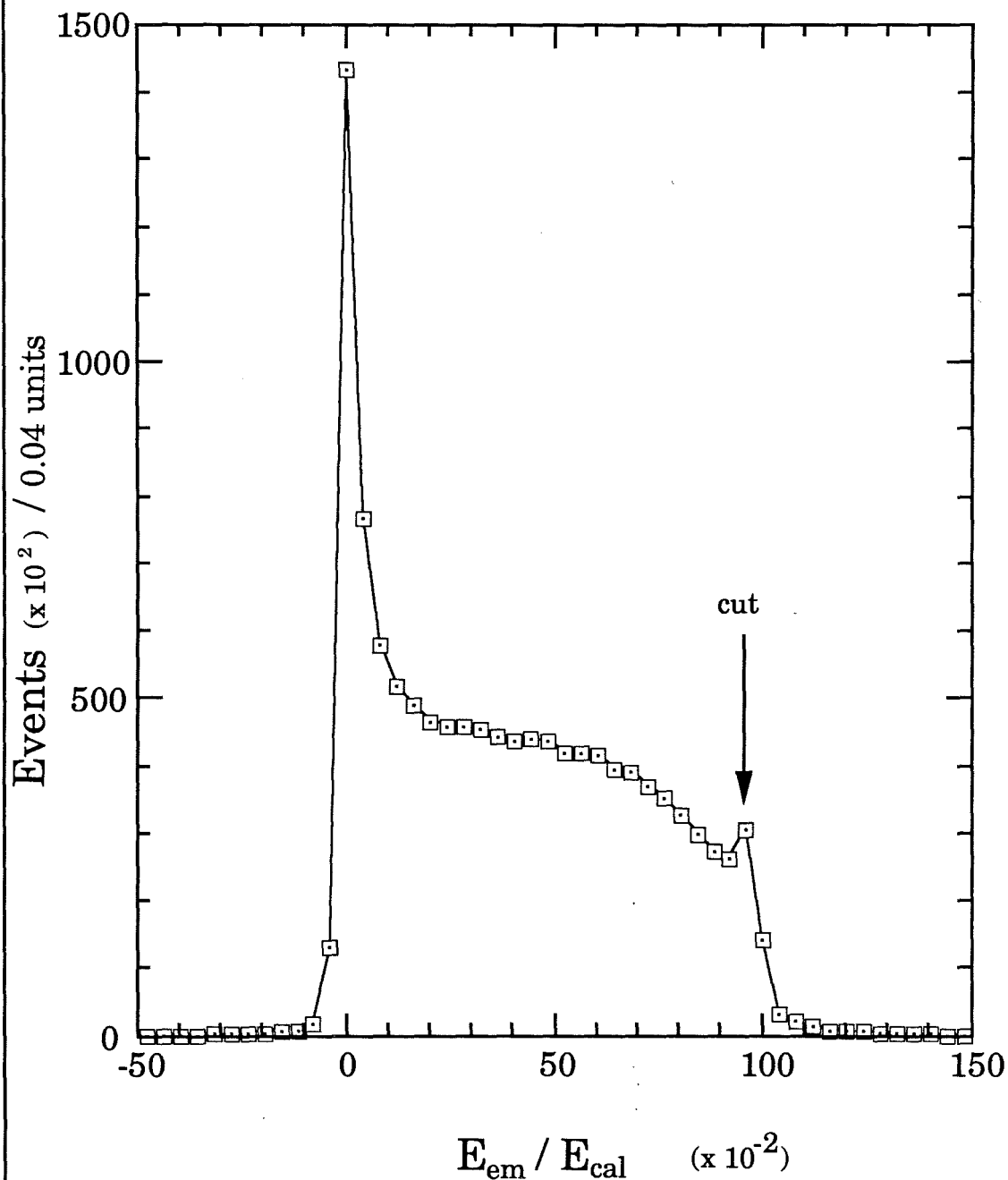


FIGURE 7.5

A distribution of events testing for the electron simulated hadron showers using the ratio of energy measured in the electromagnetic calorimeter, to the energy measured in the hadronic calorimeter.

(e) Rapidity and  $p_T$  Imbalance : In order to maximize the range of the  $\cos\theta^*$  distribution, the rapidity interval of integration is limited to ensure that the values of  $\cos\theta^*$  are within the acceptance of the detector, thereby also avoiding a distortion of the angular distribution. Thus the rapidity range was limited by:

$$-0.25 < Y < 0.10$$

The transverse momentum imbalance ( $\eta$ ) defined in Appendix A was limited so as to reduce the uncertainty in the definition of the scattering angle  $\theta^*$  in the parton-parton center-of-mass system. Assuming collinear fragmentation the imbalance is defined :

$$\eta = (P_{H_1} - P_{H_2}) = p_{TJ} (z_1 - z_2)$$

where  $z$  is the parton momentum fraction of the leading hadron, and  $p_{TJ}$  is the transverse momentum of the scattering parton. For the leading hadron, the parton transverse momentum can possess approximately 75% to 90% of the total momentum. The limit imposed therefore is :

$$\eta < 2.0 \text{ GeV}/c$$

(f) Duplicate Tracks : The track recognition and reconstruction algorithm described in Chapter 6 did not discriminate between tracks that were very closely clustered within the three (3) wire cell size limit defined in the algorithm. Two or more tracks could be reconstructed that differed only by one or two hits in the drift chamber planes. In these cases different tracks were identified with nearly the same characteristics, thus duplicating of the real track. To eliminate the duplicate tracks, a limit was

placed on the average radial separation between tracks. A separation parameter was calculated for all the possible combinations of tracks in each event:

$$D = \sqrt{\sum_{i=1}^5 (x_{ij} - x_{ik})^2 + (y_{ij} - y_{ik})^2} \quad (7.9)$$

where  $\mathbf{x}$  and  $\mathbf{y}$  represent the coordinates of track  $\mathbf{j}$  and  $\mathbf{k}$  at drift chamber  $\mathbf{i}$ . Tracks where  $D \geq 1.0$  cm were considered to be distinguishable. Tracks that are nearly identical would yield a value of  $D$  near 0. For groups of tracks with  $D < 1$  cm, the real track was selected from this group which had the best energy and track momentum comparison if the tracks were in the same fiducial volume segment. Otherwise the track with the best momentum fit was chosen.

### **§7.6 The Acceptance**

The geometric acceptance was limited by the magnet aperture and apparatus configuration. Since the reference frames were often different, a correction was necessary to transform from the dihadron center of mass frame to the proton-nucleon center of momentum frame (beam target system). The acceptance of the detector was calculated on a bin by bin basis using a Monte Carlo event simulation computer algorithm.<sup>66</sup> The vectorized code ran on a ETA-10 computer and generated charge dependent hadron pair events in bins of mass, rapidity, and  $\cos \theta$  for a range of transverse momenta. Acceptance tables were generated composed of elements that were a ratio of the number of events with tracking contained in a fiducial volume element of the calorimeter  $\{N_a(M, Y, \cos \theta^*)\}$ , to the number of generated events  $\{N_g(M, Y, \cos \theta^*)\}$ :

$$\epsilon_{\text{acc}} = \frac{N_a}{N_g}$$

Each event therefore was weighted by the ratio  $\epsilon_{\text{acc}}$  for the corresponding bin  $M$ ,  $Y$ ,  $\cos \theta^*$  and  $|p_T|$  of the event. Figure 7.6 presents a graphical description of the acceptance correction values for the events in the bins shown for  $p_T < 2.0$  GeV/c and the mass bin is  $9.0 - 10.0$  GeV/c<sup>2</sup>. This  $p_T$  of the pair (Eq.7.2) was used for the acceptance calculation and the same value was used for  $\eta$  described in the previous section.

The data must also be corrected for the inefficiency introduced by existence of inactive chamber sense wires. These "dead" wires contribute directly to the problematic change in the overall efficiency because of the resulting change in the chamber plane efficiencies. The inefficiency from this source was analyzed on a bin by bin, event by event basis since the dead wires were not uniformly distributed but locally clustered in the chamber system and tended to line up mainly in the non-bend view. The acceptance Monte Carlo produced wire hit histograms, and created files of dead wire locations in the spectrometer, so that tracks were examined with respect to their location within a region that contained a dead wire. One of the initial track recognition algorithm requirements was 15 hits out of a possible 20 to be considered as an acceptable track. Although the detector acceptance was limited by the geometry of the calorimeter and the wire chambers, a track hit corresponding to a dead wire location within a  $\pm 1/2$  wire spacing cell size was removed. If the subsequent total number of hits for that track became less than 15, then the event was removed for the bin. Otherwise, the criteria for acceptability of the track was applied.

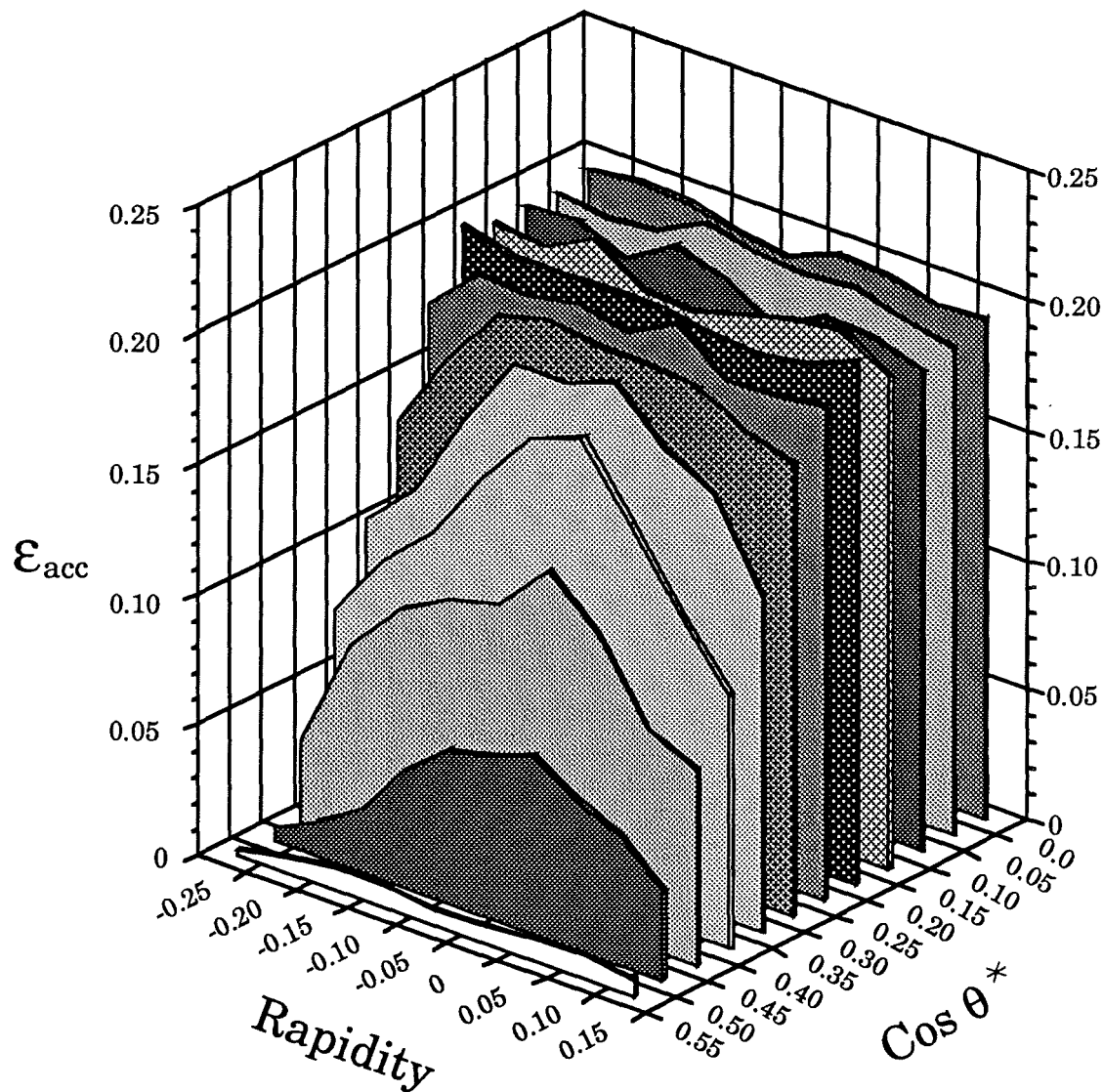


FIGURE 7.6

A graphical representation of one table of the acceptance calculation at a  $p_T$  limit of 2.0 GeV/c, in the mass bin of 9.0-10.0 GeV/c<sup>2</sup>, with a cosine of the scattering angle and the rapidity bin size of 0.05. This acceptance correction table was used for unlike sign dihadron events.

### §7.7 Differential Cross Section

The events are divided into bins of the measured variables in order to study their functional dependence. The Monte Carlo mentioned in the previous section used for calculating the acceptance and efficiencies produced an event distribution written as:

$$\frac{d^6\sigma}{dM dY d\cos\theta^* dp_{in} dp_{out} d\phi^*} \quad (7.10)$$

Where  $p_T^2 = p_{in}^2 + p_{out}^2$  and  $p_{in}$  is the transverse momentum in the scattering plane and  $p_{out}$  is perpendicular to that plane. They are gaussian distributions of unequal widths (due to the fragmentation imbalance) and the widths are adjusted to match the data. Then  $p_T$  is the transverse momentum of the pair and  $\phi^*$  the azimuthal angle of the plane defined by the beam direction and the hadron axis in that frame. The azimuthal angle can be integrated over  $2\pi$  radians in acceptance because the cross section is assumed independent of  $\phi$ . The complete expression for the cross section takes into account the track efficiencies ( $\epsilon_{track}$ ), the background corrected luminosity ( $L$ ), the number of observed events corrected for plane efficiencies and acceptance ( $N_{events}/\epsilon_{acc}$ ), and the trigger efficiency  $\epsilon_{trig}$ .

The complete differential cross section becomes:

$$\begin{aligned} \frac{d^3\sigma}{dM dY d\cos\theta^*} &= \frac{1}{\Delta M \Delta Y \Delta\cos\theta^*} \cdot \frac{1}{\epsilon_{track} \epsilon_{trig}} \cdot \frac{1}{L} \\ &\cdot \int dM \int dp_T \int dY \int d\cos\theta^* \frac{d^4 N_{events}/\epsilon_{acc}}{dM dY dp_T d\cos\theta^*} \end{aligned} \quad (7.11)$$

where  $\Delta M$ ,  $\Delta Y$ ,  $\Delta\cos\theta^*$  are the widths of the integration ranges for mass, rapidity, and cosine of the scattering angle.

## CHAPTER 8

### PHYSICS RESULTS AND DISCUSSION

#### **§8.1 Introduction**

This chapter presents the results of our measurements and where appropriate, a discussion of the data and its implications for theoretical interpretations. The angular distributions for each of the four targets in two mass ranges and three charge states are presented, along with the results of a functional fit to the data. The result on atomic mass dependence as a function of the scattering angle and dihadron charge state is also given. The angular distributions in different charge states resulting from integrating the target data with respect to mass bins are compared to leading log QCD calculations. The charge state dependence and the effect of intrinsic transverse momentum on the angular distributions, as well as the ratio of the cross sections with respect to the charge state are examined.

#### **§8.2 The Angular Distributions**

As stated in the Chapter 2, a way to parametrize the angular distributions was introduced by the CCOR collaboration (reference 49). The symmetrized form that has also been utilized here to fit the normalized data for each of the targets is:



$$\frac{d^2\sigma}{dM d\cos\theta^*} = \frac{1}{2} \left[ \frac{1}{(1 + \cos\theta^*)^a} + \frac{1}{(1 - \cos\theta^*)^a} \right] \quad (8.1)$$

The distributions are shown in mass bins of  $7.0 < M < 7.5 \text{ GeV}/c^2$  (low) and  $M > 7.5 \text{ GeV}/c^2$  (high) in the range of  $|\cos\theta^*| < 0.5$  for the three charge states. The transverse momentum of the dihadron state was required to be less than  $2.0 \text{ GeV}/c$ , to limit the variation in the choice of definition for  $\cos\theta^*$ .

The differential cross sections per nucleon as a function of  $\cos\theta^*$ , normalized by the total integrated cross section over the range of  $\cos\theta^*$ , are listed for the four targets in Tables 8.1 - 8.4. These measurements are shown in Figures 8.1 - 8.4, and the values of the cross section are averaged over a bin width of 0.05 as indicated by the horizontal error bars. Functional fits to the form (eq. 8.1), yielding a value of the power "a", are also shown on the tables for each target, mass bin, and charge state. Since the cross section per nucleon is independent of the nucleon number, the target data were integrated to improve the statistics and the values are listed in Table 8.5 with corresponding distributions shown in Figure 8.5.

**TABLE 8.1****Beryllium Target Angular Distributions**

The cross section numerical values have been normalized by the total integrated cross section over the range of  $\cos\theta^*$  for  $p_T < 2.0$  GeV/c for the three charge states, and the two mass ranges. Values of the parameter **a** obtained from fits of the form (eq. 8.1) to the data are listed.

<b>Mass</b> (GeV/c <sup>2</sup> )	<b><math>\cos\theta^*</math></b> (bin center)	<b><math>H^- H^-</math></b>	<b><math>H^+ H^-</math></b>	<b><math>H^+ H^+</math></b>
<b>7.0 &lt; M &lt; 7.5</b>	0.025	$1.29 \pm 0.22$	$1.20 \pm 0.08$	$1.33 \pm 0.15$
	0.075	$1.19 \pm 0.21$	$1.26 \pm 0.08$	$1.11 \pm 0.14$
	0.125	$1.20 \pm 0.22$	$1.36 \pm 0.09$	$1.19 \pm 0.15$
	0.175	$1.81 \pm 0.27$	$1.35 \pm 0.09$	$1.17 \pm 0.15$
	0.225	$1.94 \pm 0.28$	$1.47 \pm 0.09$	$1.46 \pm 0.17$
	0.275	$1.59 \pm 0.26$	$1.75 \pm 0.10$	$1.70 \pm 0.18$
	0.325	$1.80 \pm 0.29$	$2.07 \pm 0.12$	$2.32 \pm 0.22$
	0.375	$2.38 \pm 0.34$	$2.74 \pm 0.15$	$2.16 \pm 0.23$
	0.425	$3.56 \pm 0.53$	$3.18 \pm 0.19$	$3.45 \pm 0.35$
	0.475	$3.23 \pm 0.63$	$3.62 \pm 0.28$	$4.11 \pm 0.48$
<b>a</b>		<b><math>2.61 \pm 0.26</math></b>	<b><math>2.83 \pm 0.10</math></b>	<b><math>3.06 \pm 0.17</math></b>
<b>7.5 &lt; M</b>	0.025	$0.49 \pm 0.24$	$0.88 \pm 0.12$	$0.94 \pm 0.21$
	0.075	$1.02 \pm 0.36$	$1.01 \pm 0.12$	$0.71 \pm 0.19$
	0.125	$0.88 \pm 0.33$	$0.96 \pm 0.12$	$0.98 \pm 0.22$
	0.175	$0.99 \pm 0.33$	$1.08 \pm 0.13$	$1.41 \pm 0.28$
	0.225	$1.65 \pm 0.46$	$1.08 \pm 0.13$	$1.38 \pm 0.27$
	0.275	$2.13 \pm 0.55$	$1.65 \pm 0.16$	$1.63 \pm 0.30$
	0.325	$2.07 \pm 0.54$	$1.86 \pm 0.17$	$1.59 \pm 0.29$
	0.375	$3.14 \pm 0.69$	$2.62 \pm 0.22$	$2.97 \pm 0.44$
	0.425	$3.70 \pm 0.77$	$2.98 \pm 0.25$	$4.34 \pm 0.58$
	0.475	$3.93 \pm 0.93$	$5.89 \pm 0.49$	$4.07 \pm 0.62$
<b>a</b>		<b><math>3.83 \pm 0.37</math></b>	<b><math>3.82 \pm 0.16</math></b>	<b><math>3.69 \pm 0.26</math></b>

**TABLE 8.2****Aluminum Target Angular Distributions**

The cross section numerical values have been normalized by the total integrated cross section over the range of  $\cos\theta^*$  for  $p_T < 2.0$  GeV/c for the three charge states, and the two mass ranges. Values of the parameter **a** obtained from fits of the form (eq. 8.1) to the data are listed.

<b>Mass</b> (GeV/c <sup>2</sup> )	<b><math>\cos\theta^*</math></b> (bin center)	<b><math>H^- H^-</math></b>	<b><math>H^+ H^-</math></b>	<b><math>H^+ H^+</math></b>
7.0 < M < 7.5	0.025	$1.28 \pm 0.26$	$1.34 \pm 0.10$	$1.16 \pm 0.16$
	0.075	$1.04 \pm 0.24$	$1.36 \pm 0.10$	$1.18 \pm 0.16$
	0.125	$1.25 \pm 0.26$	$1.29 \pm 0.10$	$1.45 \pm 0.18$
	0.175	$1.46 \pm 0.29$	$1.40 \pm 0.11$	$1.58 \pm 0.19$
	0.225	$1.85 \pm 0.33$	$1.48 \pm 0.11$	$1.45 \pm 0.18$
	0.275	$2.61 \pm 0.39$	$1.69 \pm 0.12$	$2.07 \pm 0.23$
	0.325	$2.24 \pm 0.38$	$1.98 \pm 0.13$	$2.17 \pm 0.24$
	0.375	$2.31 \pm 0.42$	$2.58 \pm 0.18$	$2.24 \pm 0.26$
	0.425	$3.02 \pm 0.57$	$2.69 \pm 0.20$	$3.29 \pm 0.37$
	0.475	$2.94 \pm 0.59$	$4.19 \pm 0.32$	$3.40 \pm 0.49$
<b>a</b>		<b><math>2.52 \pm 0.28</math></b>	<b><math>2.72 \pm 0.12</math></b>	<b><math>2.67 \pm 0.19</math></b>
7.5 < M	0.025	$0.47 \pm 0.27$	$1.19 \pm 0.18$	$0.93 \pm 0.22$
	0.075	$1.33 \pm 0.50$	$1.09 \pm 0.17$	$1.15 \pm 0.25$
	0.125	$1.08 \pm 0.44$	$1.42 \pm 0.19$	$0.64 \pm 0.18$
	0.175	$0.83 \pm 0.37$	$1.22 \pm 0.18$	$1.30 \pm 0.26$
	0.225	$1.64 \pm 0.55$	$1.66 \pm 0.21$	$0.56 \pm 0.18$
	0.275	$0.98 \pm 0.44$	$1.70 \pm 0.21$	$1.12 \pm 0.26$
	0.325	$2.68 \pm 0.72$	$2.33 \pm 0.26$	$1.45 \pm 0.28$
	0.375	$2.69 \pm 0.75$	$2.58 \pm 0.28$	$2.27 \pm 0.38$
	0.425	$5.29 \pm 1.15$	$2.56 \pm 0.31$	$3.58 \pm 0.55$
	0.475	$3.01 \pm 0.95$	$4.26 \pm 0.49$	$7.01 \pm 1.03$
<b>a</b>		<b><math>3.79 \pm 0.42</math></b>	<b><math>2.87 \pm 0.20</math></b>	<b><math>4.87 \pm 0.36</math></b>

**TABLE 8.3****Iron Target Angular Distributions**

The cross section numerical values have been normalized by the total integrated cross section over the range of  $\cos\theta^*$  for  $p_T < 2.0$  GeV/c for the three charge states, and the two mass ranges. Values of the parameter **a** obtained from fits of the form (eq. 8.1) to the data are listed.

<b>Mass</b> (GeV/c <sup>2</sup> )	<b>cos<math>\theta^*</math></b> (bin center)	<b>H<sup>-</sup> H<sup>-</sup></b>	<b>H<sup>+</sup> H<sup>-</sup></b>	<b>H<sup>+</sup> H<sup>+</sup></b>
7.0 < M < 7.5	0.025	1.01 ± 0.17	1.23 ± 0.07	1.30 ± 0.12
	0.075	1.41 ± 0.20	1.33 ± 0.08	1.32 ± 0.12
	0.125	1.43 ± 0.20	1.24 ± 0.07	1.17 ± 0.12
	0.175	1.45 ± 0.21	1.35 ± 0.08	1.38 ± 0.13
	0.225	1.64 ± 0.23	1.49 ± 0.08	1.47 ± 0.13
	0.275	1.79 ± 0.24	1.62 ± 0.09	1.78 ± 0.15
	0.325	1.99 ± 0.26	1.94 ± 0.10	2.04 ± 0.17
	0.375	2.70 ± 0.32	2.44 ± 0.13	2.19 ± 0.18
	0.425	2.86 ± 0.39	3.31 ± 0.18	3.56 ± 0.30
	0.475	3.71 ± 0.57	4.05 ± 0.24	3.79 ± 0.36
<b>a</b>		<b>2.72 ± 0.22</b>	<b>2.90 ± 0.09</b>	<b>2.83 ± 0.14</b>
7.5 < M	0.025	0.86 ± 0.26	1.13 ± 0.12	0.79 ± 0.16
	0.075	0.89 ± 0.27	1.25 ± 0.13	0.96 ± 0.17
	0.125	1.48 ± 0.35	1.29 ± 0.13	1.33 ± 0.21
	0.175	1.28 ± 0.33	1.13 ± 0.12	1.10 ± 0.19
	0.225	1.30 ± 0.33	1.37 ± 0.14	1.29 ± 0.20
	0.275	1.63 ± 0.38	1.79 ± 0.16	1.94 ± 0.26
	0.325	2.17 ± 0.43	1.92 ± 0.16	2.03 ± 0.26
	0.375	2.69 ± 0.51	2.29 ± 0.19	2.53 ± 0.32
	0.425	3.38 ± 0.69	3.70 ± 0.27	2.80 ± 0.35
	0.475	4.32 ± 0.92	4.14 ± 0.35	5.24 ± 0.67
<b>a</b>		<b>3.42 ± 0.34</b>	<b>3.15 ± 0.14</b>	<b>3.50 ± 0.22</b>

# TABLE 8.4

## Tungsten Target Angular Distributions

The cross section numerical values have been normalized by the total integrated cross section over the range of  $\cos\theta^*$  for  $p_T < 2.0$  GeV/c for the three charge states, and the two mass ranges. Values of the parameter  $a$  obtained from fits of the form (eq. 8.1) to the data are listed.

Mass (GeV/c <sup>2</sup> )	$\cos\theta^*$ (bin center)	$H^- H^-$	$H^+ H^-$	$H^+ H^+$
$7.0 < M < 7.5$	0.025	$0.91 \pm 0.28$	$1.30 \pm 0.13$	$1.04 \pm 0.19$
	0.075	$0.62 \pm 0.24$	$1.42 \pm 0.14$	$1.25 \pm 0.21$
	0.125	$1.34 \pm 0.35$	$1.51 \pm 0.15$	$0.95 \pm 0.18$
	0.175	$1.02 \pm 0.31$	$1.38 \pm 0.14$	$1.67 \pm 0.25$
	0.225	$1.30 \pm 0.34$	$1.39 \pm 0.14$	$1.44 \pm 0.23$
	0.275	$2.10 \pm 0.46$	$1.74 \pm 0.16$	$1.79 \pm 0.26$
	0.325	$2.31 \pm 0.50$	$1.71 \pm 0.17$	$1.93 \pm 0.28$
	0.375	$2.78 \pm 0.55$	$2.86 \pm 0.27$	$2.61 \pm 0.37$
	0.425	$3.60 \pm 0.85$	$3.40 \pm 0.31$	$3.01 \pm 0.47$
	0.475	$4.01 \pm 0.87$	$3.31 \pm 0.37$	$4.31 \pm 0.67$
<b>a</b>		<b><math>3.64 \pm 0.34</math></b>	<b><math>2.63 \pm 0.16</math></b>	<b><math>3.12 \pm 0.24</math></b>
$7.5 < M$	0.025	$0.51 \pm 0.36$	$1.38 \pm 0.24$	$1.33 \pm 0.37$
	0.075	$0.60 \pm 0.43$	$0.79 \pm 0.18$	$0.89 \pm 0.30$
	0.125	$0.42 \pm 0.30$	$1.31 \pm 0.23$	$0.83 \pm 0.30$
	0.175	$0.34 \pm 0.34$	$1.29 \pm 0.23$	$1.17 \pm 0.37$
	0.225	$0.59 \pm 0.42$	$0.99 \pm 0.20$	$0.83 \pm 0.29$
	0.275	$2.79 \pm 0.88$	$1.66 \pm 0.26$	$1.45 \pm 0.40$
	0.325	$1.22 \pm 0.61$	$2.14 \pm 0.32$	$1.76 \pm 0.44$
	0.375	$3.80 \pm 1.10$	$2.58 \pm 0.37$	$2.68 \pm 0.61$
	0.425	$2.05 \pm 0.92$	$3.00 \pm 0.44$	$3.71 \pm 0.76$
	0.475	$7.67 \pm 2.05$	$4.86 \pm 0.72$	$5.36 \pm 1.12$
<b>a</b>		<b><math>5.54 \pm 0.70</math></b>	<b><math>3.46 \pm 0.26</math></b>	<b><math>4.04 \pm 0.42</math></b>

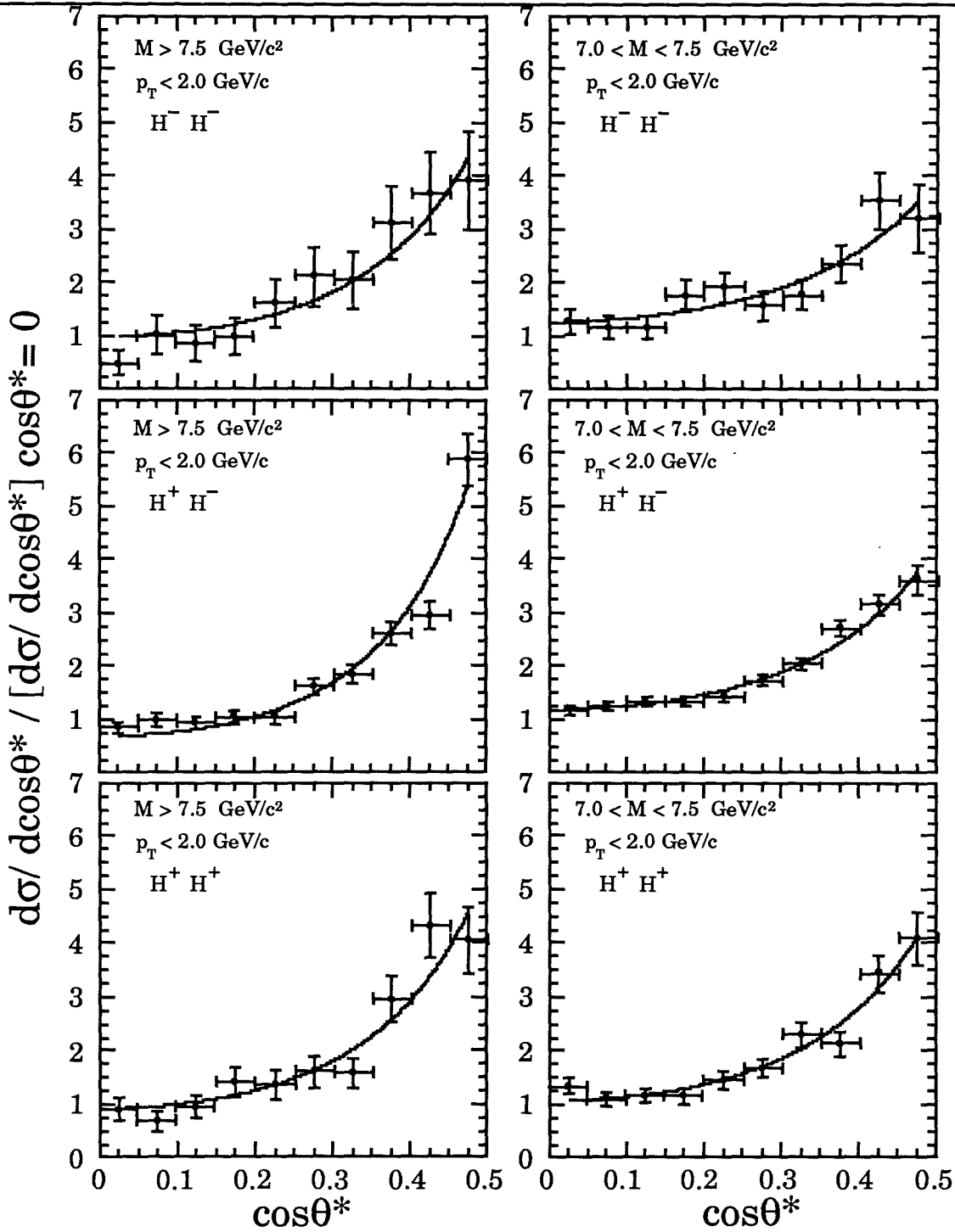


FIGURE 8.1

The **beryllium** target data dihadron angular distributions as a function of  $\cos\theta^*$  for fixed mass bins. The curves shown are a functional fit to the normalized data. The errors indicated are statistical errors only.

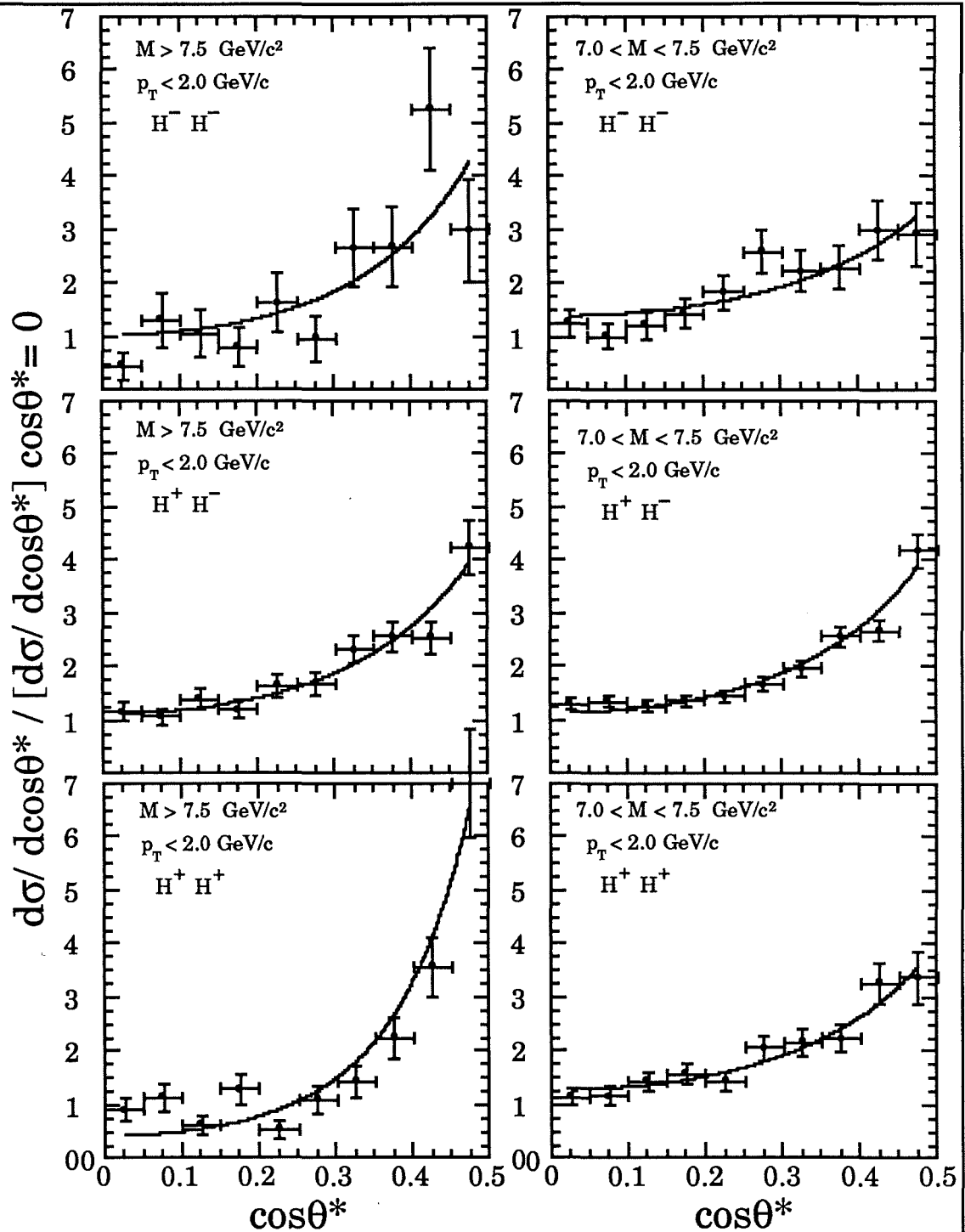


FIGURE 8.2

The **aluminum** target data dihadron angular distributions as a function of  $\cos\theta^*$  for fixed mass bins. The curves shown are a functional fit to the normalized data. The errors indicated are statistical errors only.

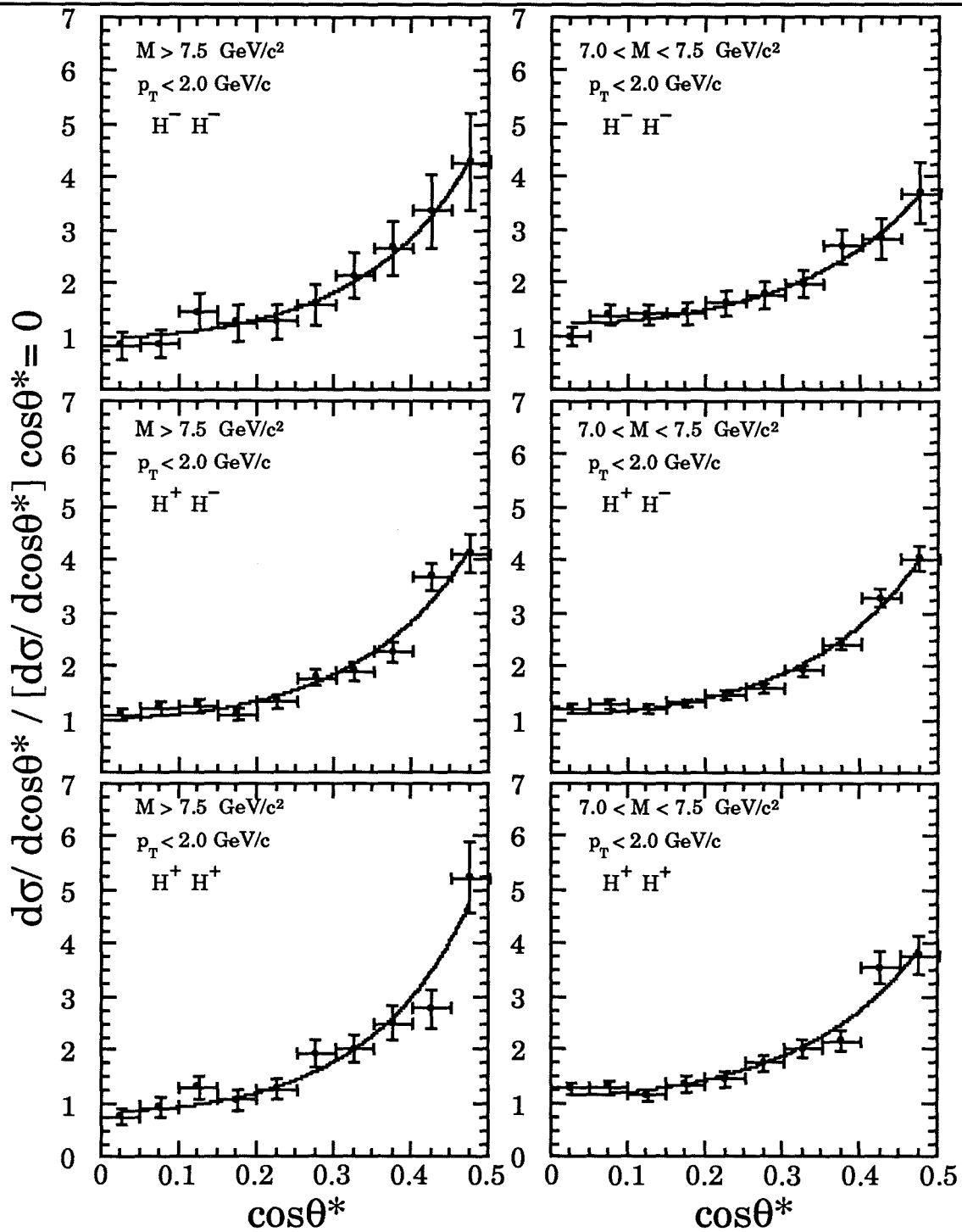


FIGURE 8.3

The **iron** target data dihadron angular distributions as a function of  $\cos\theta^*$  for fixed mass bins. The curves shown are a functional fit to the normalized data. The errors indicated are statistical errors only.



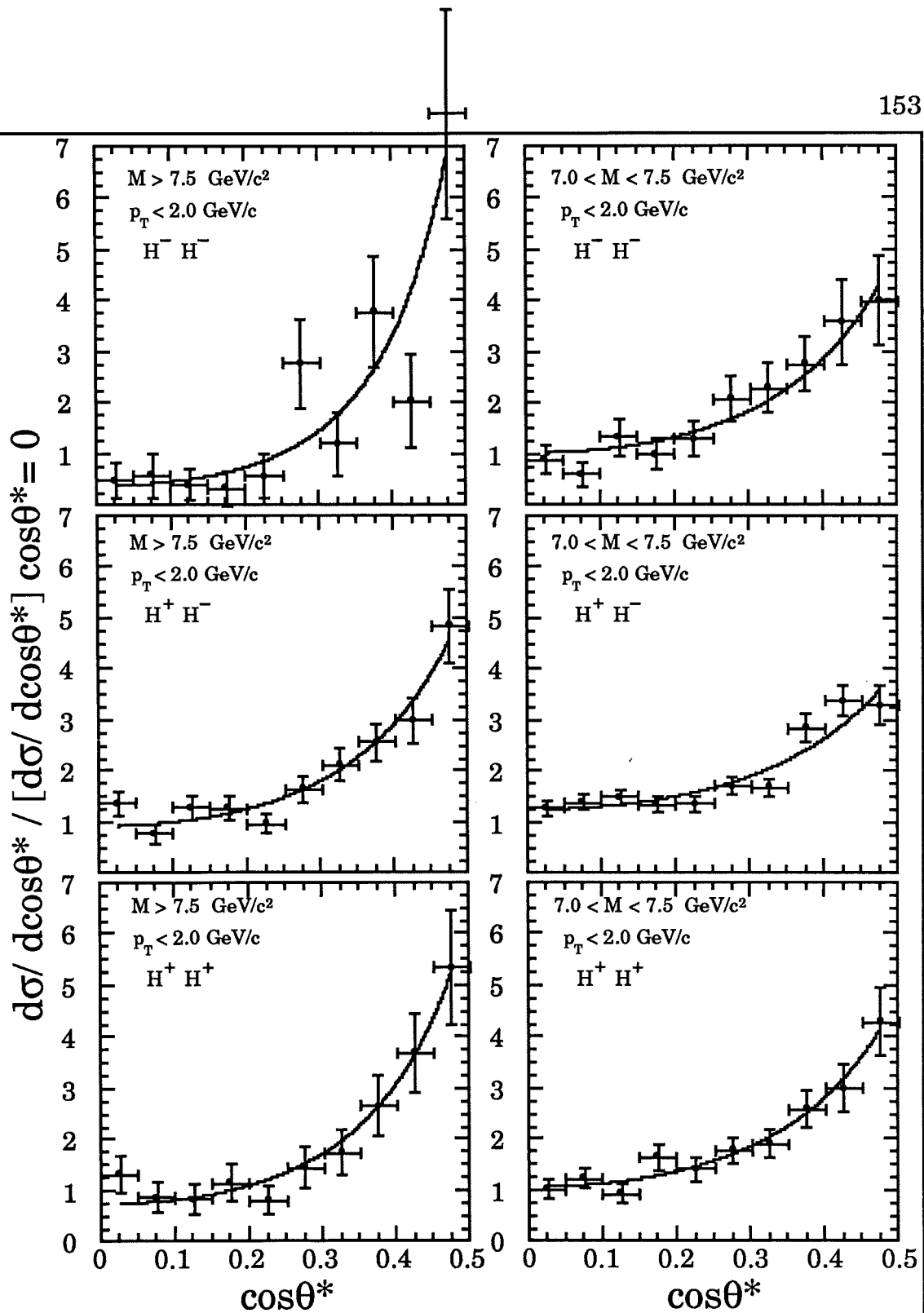


FIGURE 8.4

The **tungsten** target data dihadron angular distributions as a function of  $\cos\theta^*$  for fixed mass bins. The curves shown are a functional fit to the normalized data. The errors indicated are statistical errors only.

# TABLE 8.5

## Integrated Target Data Angular Distributions

The cross section numerical values have been normalized by the total integrated cross section over the range of  $\cos\theta^*$  for  $p_T < 2.0$  GeV/c for the three charge states, and the two mass ranges. Values of the parameter  $a$  obtained from fits of the form (eq. 8.1) to the data are listed.

Mass (GeV/c <sup>2</sup> )	$\cos\theta^*$ (bin center)	$H^- H^-$	$H^+ H^-$	$H^+ H^+$
$7.0 < M < 7.5$	0.025	$1.13 \pm 0.11$	$1.25 \pm 0.04$	$1.24 \pm 0.08$
	0.075	$1.17 \pm 0.11$	$1.33 \pm 0.05$	$1.23 \pm 0.08$
	0.125	$1.32 \pm 0.12$	$1.32 \pm 0.05$	$1.21 \pm 0.08$
	0.175	$1.50 \pm 0.13$	$1.36 \pm 0.05$	$1.41 \pm 0.08$
	0.225	$1.73 \pm 0.14$	$1.47 \pm 0.05$	$1.46 \pm 0.08$
	0.275	$1.95 \pm 0.16$	$1.69 \pm 0.05$	$1.83 \pm 0.10$
	0.325	$2.03 \pm 0.16$	$1.96 \pm 0.06$	$2.12 \pm 0.11$
	0.375	$2.54 \pm 0.19$	$2.60 \pm 0.08$	$2.25 \pm 0.12$
	0.425	$3.18 \pm 0.26$	$3.15 \pm 0.10$	$3.40 \pm 0.18$
	0.475	$3.45 \pm 0.32$	$3.88 \pm 0.15$	$3.85 \pm 0.23$
<b>a</b>		<b><math>2.73 \pm 0.13</math></b>	<b><math>2.82 \pm 0.05</math></b>	<b><math>2.87 \pm 0.09</math></b>
$7.5 < M$	0.025	$0.64 \pm 0.14$	$1.09 \pm 0.07$	$0.92 \pm 0.11$
	0.075	$0.98 \pm 0.19$	$1.09 \pm 0.07$	$0.94 \pm 0.11$
	0.125	$1.12 \pm 0.19$	$1.22 \pm 0.08$	$1.02 \pm 0.11$
	0.175	$1.00 \pm 0.18$	$1.15 \pm 0.07$	$1.23 \pm 0.13$
	0.225	$1.38 \pm 0.22$	$1.29 \pm 0.08$	$1.07 \pm 0.12$
	0.275	$1.77 \pm 0.26$	$1.71 \pm 0.09$	$1.61 \pm 0.15$
	0.325	$2.14 \pm 0.28$	$2.01 \pm 0.10$	$1.75 \pm 0.15$
	0.375	$2.94 \pm 0.34$	$2.48 \pm 0.12$	$2.58 \pm 0.20$
	0.425	$3.69 \pm 0.43$	$3.17 \pm 0.15$	$3.46 \pm 0.26$
	0.475	$4.34 \pm 0.54$	$4.79 \pm 0.24$	$5.42 \pm 0.41$
<b>a</b>		<b><math>3.76 \pm 0.21</math></b>	<b><math>3.33 \pm 0.09</math></b>	<b><math>3.81 \pm 0.14</math></b>

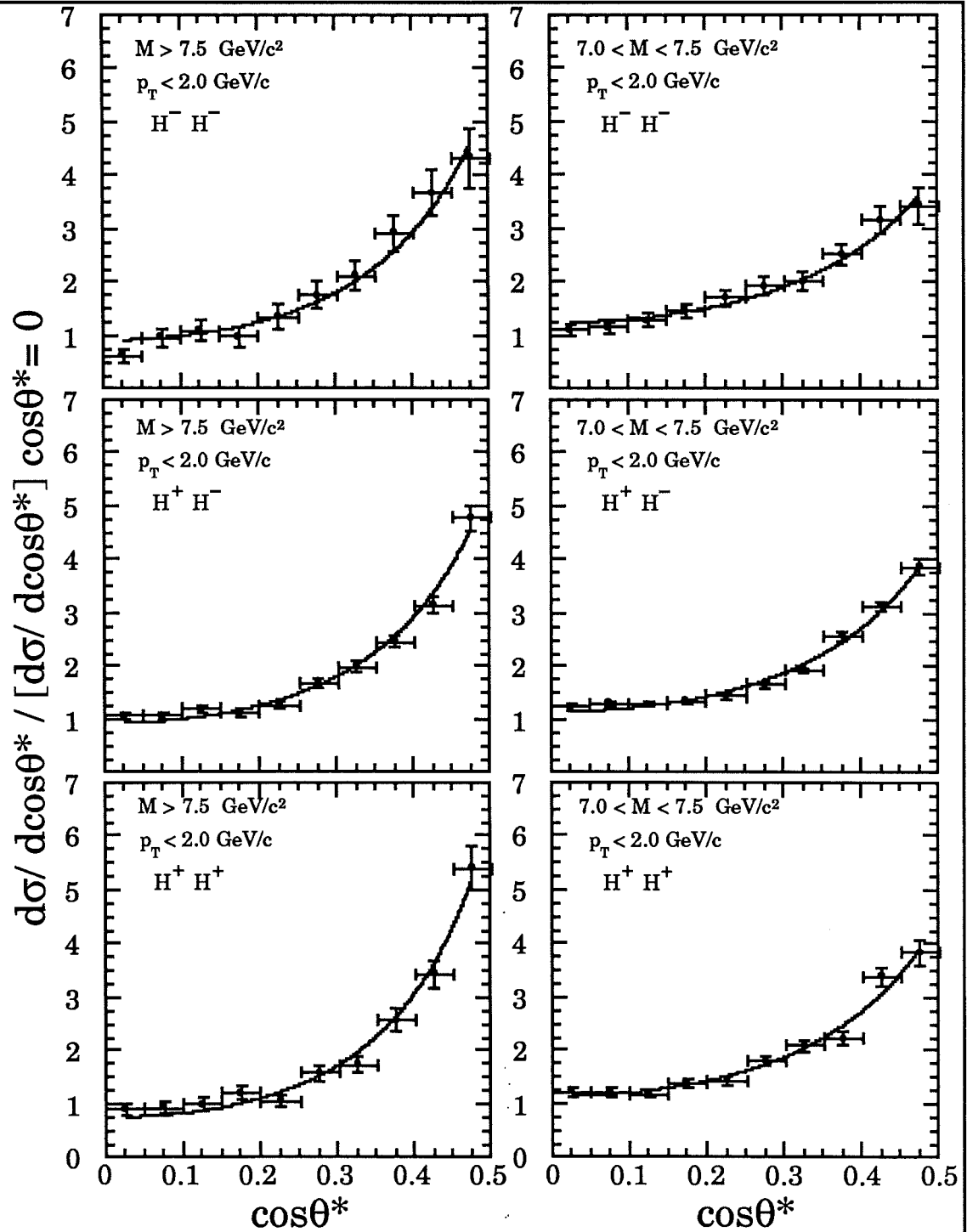


FIGURE 8.5

The dihadron angular distributions as a function of  $\cos\theta^*$  for fixed mass bins using the combined data of the four targets. The curves shown are a functional fit to the normalized data. The errors indicated are statistical errors only.

The major uncertainties in the shape of the  $\cos\theta^*$  distributions arise from the uncertainty in the acceptance correction and nonuniformity of the magnetic field. The combination of the nonuniform field and corrections due to various missing chamber wires causes a momentum scale error that varies with position. While the field irregularities introduces an error less than 1%, the steep cross section amplifies this relative error for varying  $\cos\theta^*$ , such that at the largest value of  $\cos\theta^*$  the acceptance uncertainty is 10%. With the uncertainties due to the calibration of the calorimeters (2%), and the luminosity counters (2%), as well as the uncertainty in the ion chamber (2%), the total systematic error is stated as 16% in the relative normalization over the variation in  $\cos\theta^*$ .

It has been asserted that evidence of nuclear dependence in deep inelastic scattering may be caused by hard scattering of partons.<sup>67</sup> Where single parton scattering may depend on the nucleon momentum fraction ( $x_b$ ) and the momentum transfer ( $q$ ), it is thought that double hard scattering may occur and depend on the radius of the nucleus. The double scattering would be one hard scattering interaction followed by another hard scattering (where the typical energy transfer is greater than a few GeV), or a hard scattering followed by a soft scattering all within the nuclear radius. Evidence for this phenomena would be a shift in the  $p_T$  spectrum for more dense targets (thus larger nuclear sizes). Interpreting data from single high  $p_T$  hadron production as well as isolating the above effect would be difficult due to the intrinsic motion of the partons. Our experiment uses a symmetric trigger to measure the cross sections from two particle inclusive reactions, which are thought to be insensitive to

initial state motions of the partons. Thus any shift in the  $p_T$  spectrum for larger values of target densities might be indicated by a change in the shape of the angular distribution as a function of target type. For this purpose different functional fits to the data would indicate that fragmentation occurred inside the nucleus. A summary of the functional fits to the data are listed in Table 8.6, including fits of the same form to the QCD Monte Carlo results. The fit to the normalized distributions are listed for each charge state and the two mass ranges. The fit to the QCD Monte Carlo generated results are indicated for each target. Although some target to target statistical fluctuations are shown in the data, differences in the QCD calculations from target to target are due to statistics. (The QCD Monte Carlo will be discussed in a later section). The data are summed over charge states and mass bins to yield the fits for the 6 integrated data sets. A plot of the fit parameter "a" verses the target atomic number relative to the charge state and the mass ranges is shown in Figure 8.6. Taking into account the errors in the fitting and low statistics, no appreciable change in the fitting parameter is observed as a function of mass, for this range of targets. The shaded area, indicated for reference in the plot shows the range of the fit parameter for values of 3.0 - 4.0 which covers the average values for fits to the data. A linear fit of the values of "a" for one charge state and mass bin as a function of the atomic number yields a slope of  $0.002 \pm 0.001$  in all cases except the low mass (- -) state, where the slope is  $0.011 \pm 0.004$ . Although this may not be a conclusive test for refuting double hard scattering, it does however add further justification for summing the data from all of the different targets to improve the statistics for further studies on charge dependence.

**TABLE 8.6****Summary of the Functional Fits**

Values of the parameter **a** obtained from fits of the form (eq. 8.1) to the QCD Monte Carlo calculations, and fits to the experimental data are listed.

Target Type	$H^- H^-$	$H^+ H^-$	$H^+ H^+$	
	<b>Mass Range <math>7.0 &lt; M &lt; 7.5</math> (GeV/c<sup>2</sup>)</b>			
<b>Beryllium</b>	<b><math>2.61 \pm 0.26</math></b>	<b><math>2.83 \pm 0.10</math></b>	<b><math>3.06 \pm 0.17</math></b>	
	$2.88 \pm 0.03$	$2.87 \pm 0.03$	$2.89 \pm 0.03$	$\leftarrow$ QCD
<b>Aluminum</b>	<b><math>2.52 \pm 0.28</math></b>	<b><math>2.72 \pm 0.12</math></b>	<b><math>2.67 \pm 0.19</math></b>	
	$2.88 \pm 0.03$	$2.87 \pm 0.03$	$2.89 \pm 0.03$	$\leftarrow$ QCD
<b>Iron</b>	<b><math>2.72 \pm 0.22</math></b>	<b><math>2.90 \pm 0.09</math></b>	<b><math>2.83 \pm 0.14</math></b>	
	$2.85 \pm 0.03$	$2.88 \pm 0.03$	$2.89 \pm 0.03$	$\leftarrow$ QCD
<b>Tungsten</b>	<b><math>3.64 \pm 0.34</math></b>	<b><math>2.63 \pm 0.16</math></b>	<b><math>3.12 \pm 0.24</math></b>	
	$2.85 \pm 0.03$	$2.83 \pm 0.03$	$2.85 \pm 0.03$	$\leftarrow$ QCD
<b>Integrated</b>				
<b>Target data</b>	<b><math>2.73 \pm 0.13</math></b>	<b><math>2.82 \pm 0.05</math></b>	<b><math>2.87 \pm 0.09</math></b>	
	<b>Mass Range <math>7.5 &lt; M</math> (GeV/c<sup>2</sup>)</b>			
<b>Beryllium</b>	<b><math>3.83 \pm 0.37</math></b>	<b><math>3.82 \pm 0.16</math></b>	<b><math>3.69 \pm 0.26</math></b>	
	$2.73 \pm 0.03$	$2.76 \pm 0.03$	$2.75 \pm 0.03$	$\leftarrow$ QCD
<b>Aluminum</b>	<b><math>3.79 \pm 0.42</math></b>	<b><math>2.87 \pm 0.20</math></b>	<b><math>4.87 \pm 0.36</math></b>	
	$2.74 \pm 0.03$	$2.76 \pm 0.03$	$2.75 \pm 0.03$	$\leftarrow$ QCD
<b>Iron</b>	<b><math>3.42 \pm 0.34</math></b>	<b><math>3.15 \pm 0.14</math></b>	<b><math>3.50 \pm 0.22</math></b>	
	$2.88 \pm 0.03$	$2.88 \pm 0.03$	$2.75 \pm 0.03$	$\leftarrow$ QCD
<b>Tungsten</b>	<b><math>5.54 \pm 0.70</math></b>	<b><math>3.46 \pm 0.26</math></b>	<b><math>4.04 \pm 0.42</math></b>	
	$2.88 \pm 0.03$	$2.87 \pm 0.03$	$2.89 \pm 0.03$	$\leftarrow$ QCD
<b>Integrated</b>				
<b>Target data</b>	<b><math>3.76 \pm 0.21</math></b>	<b><math>3.33 \pm 0.09</math></b>	<b><math>3.81 \pm 0.14</math></b>	

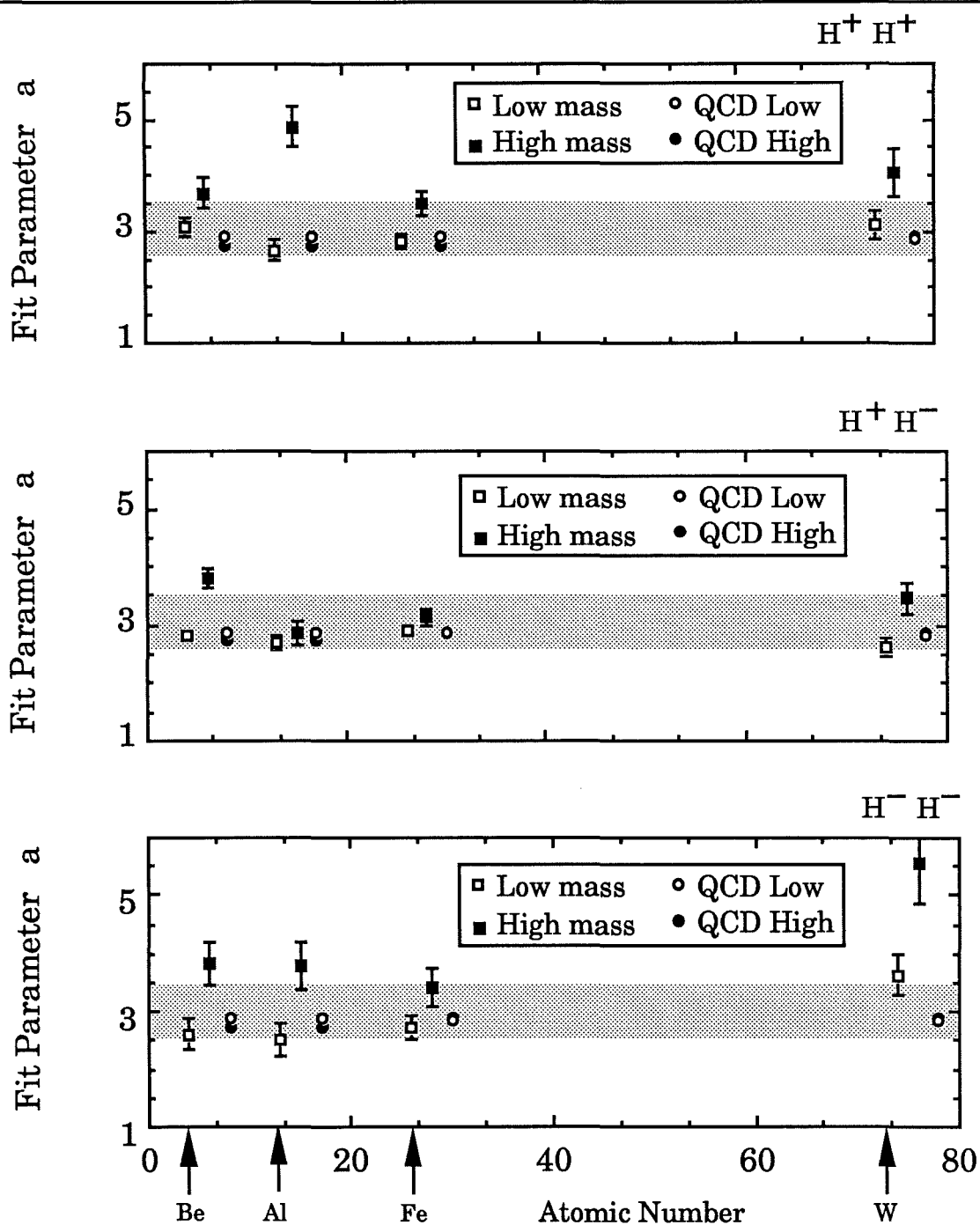


FIGURE 8.6

The functional fit to the data, parameter  $a$  is plotted versus the target atomic number. The higher mass state data and the same functional fit to the QCD monte carlo results have been shifted to the right for clarity.

## §8.2 The Atomic Weight Dependence

Experiments have reported large nuclear effects in the analysis of dijet production from nuclei. Eliminating the possible collective effects due to intrinsic motion of the partons and interaction of scattered partons with nuclear matter by choosing a symmetric dihadron state allows the present experiment to test for the nuclear effects in unlike-sign charge states as well as here to fore unmeasured like-sign charged states. The A-dependence has been measured relative to the charge state and with respect to a wide mass range of the dihadron state, but within a limited range of the center of mass scattering angle.<sup>68</sup> This analysis continues the A-dependence studies with respect to the parton-parton scattering angle.

The dependence of the event yield per unit luminosity on the atomic weight has been parametrized in the linear form:

$$\ln[\sigma(A)] = \alpha \ln(A) + \ln \sigma_0 \quad (8.2)$$

for each bin of the parton-parton scattering angle, with  $p_T < 2.0$  GeV/c in the two dihadron mass bins and the three charge states. The value of  $\alpha$  is determined by fitting the above form which also can be written  $\sigma(A) = \sigma_0 A^\alpha$  where  $\alpha$  is the slope of the linear equation 8.2. A representative example of 10 of these 60 fits is shown in Figure 8.7, for data corresponding to the  $7.0 < M < 7.5$  GeV/c<sup>2</sup> mass range and the ( + + ) charge state. The upper plot shows four fits for the bins in  $\cos\theta^* < 0.2$ , while the lower part of the figure has  $\cos\theta^* > 0.2$ .



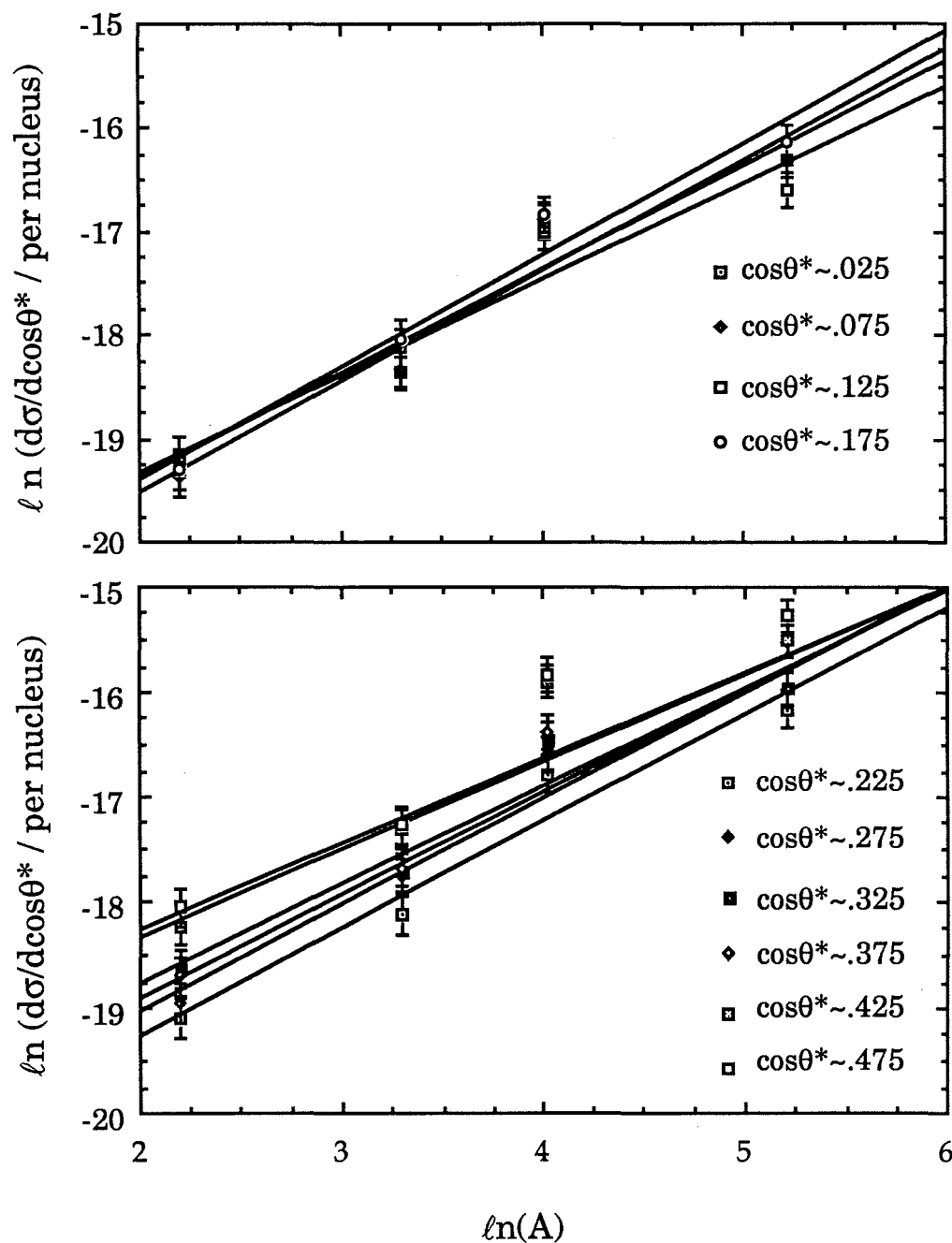


FIGURE 8.7

A representative example of the atomic weight dependence parameter  $\alpha$  determined from a linear fit to the scattering cross section as a function of the atomic weight. The data above corresponds to the (+ +) charge state in the mass range  $7.0 < M < 7.5$   $\text{GeV}/c^2$ . The value of all the slopes are listed in Table 8.7.

The data for  $\cos\theta^* < 0.2$  is examined to confirm consistency of the results with previously published results on the A-dependence from this experiment wherein the data was fitted as a function of the dihadron mass and charge state. The value of  $\alpha$  was reported as  $1.049 \pm 0.007$  in the range of  $p_T < 2.0 \text{ GeV}/c$ ,  $|\cos\theta^*| < 0.2$ , and over the mass range of  $6.0 < M < 15.0 \text{ GeV}/c^2$ , for the three charge states. In this analysis the value of  $\alpha$  in the same angular range and charge states, but over the slightly different mass range is  $1.043 \pm 0.013$ . The numerical values and their statistical errors for  $\alpha$  are presented in Table 8.7. The average value of  $\alpha$  for this measurement over the full  $\cos\theta^*$  range is  $1.018 \pm 0.009$ . With a total systematic error in the  $\cos\theta^*$  distribution (as stated earlier) of 16%, the corresponding error in  $\alpha$  is then  $\pm 0.035$ . The results for  $\alpha$  vs  $\cos\theta^*$  are also shown for the three charge states in Figure 8.7 (for low mass) and in Figure 8.8 (for the high mass). For reference, a shaded area is centered on  $\alpha = 1.0$  with a width equal to the error in the global average of all the data values.

**TABLE 8.7**

**Atomic Weight Dependence**

The dependence of the cross section on the atomic weight as a function of parton-parton scattering angle for  $p_T < 2.0$  GeV/c for the three charge states, and the two mass ranges are summarized. Values of the parameter  $\alpha$  are listed.

Mass (GeV/c <sup>2</sup> )	cos $\theta^*$ (bin center)	H <sup>-</sup> H <sup>-</sup>	H <sup>+</sup> H <sup>-</sup>	H <sup>+</sup> H <sup>+</sup>
7.0 < M < 7.5	0.025	0.77 $\pm$ 0.02	0.97 $\pm$ 0.01	1.01 $\pm$ 0.01
	0.075	0.97 $\pm$ 0.03	0.98 $\pm$ 0.02	1.06 $\pm$ 0.02
	0.125	0.99 $\pm$ 0.04	0.98 $\pm$ 0.02	0.93 $\pm$ 0.02
	0.175	0.87 $\pm$ 0.04	0.96 $\pm$ 0.03	1.08 $\pm$ 0.03
	0.225	0.85 $\pm$ 0.05	0.94 $\pm$ 0.03	1.02 $\pm$ 0.03
	0.275	1.04 $\pm$ 0.08	0.97 $\pm$ 0.04	1.02 $\pm$ 0.03
	0.325	1.09 $\pm$ 0.09	0.89 $\pm$ 0.04	0.93 $\pm$ 0.03
	0.375	1.08 $\pm$ 0.09	0.96 $\pm$ 0.03	1.09 $\pm$ 0.05
	0.425	1.01 $\pm$ 0.10	0.95 $\pm$ 0.04	0.96 $\pm$ 0.04
	0.475	0.99 $\pm$ 0.09	0.88 $\pm$ 0.04	0.98 $\pm$ 0.04
7.5 < M	0.025	1.35 $\pm$ 0.06	1.17 $\pm$ 0.03	1.14 $\pm$ 0.03
	0.075	1.03 $\pm$ 0.11	1.05 $\pm$ 0.04	1.20 $\pm$ 0.03
	0.125	1.11 $\pm$ 0.10	1.07 $\pm$ 0.05	1.07 $\pm$ 0.05
	0.175	1.15 $\pm$ 0.16	1.07 $\pm$ 0.05	1.06 $\pm$ 0.05
	0.225	0.91 $\pm$ 0.17	1.06 $\pm$ 0.06	1.13 $\pm$ 0.08
	0.275	1.03 $\pm$ 0.25	1.00 $\pm$ 0.08	1.07 $\pm$ 0.09
	0.325	0.99 $\pm$ 0.24	1.03 $\pm$ 0.08	1.19 $\pm$ 0.08
	0.375	1.04 $\pm$ 0.28	0.93 $\pm$ 0.08	1.02 $\pm$ 0.14
	0.425	0.91 $\pm$ 0.27	1.01 $\pm$ 0.09	0.98 $\pm$ 0.10
	0.475	1.17 $\pm$ 0.26	0.89 $\pm$ 0.07	1.02 $\pm$ 0.10

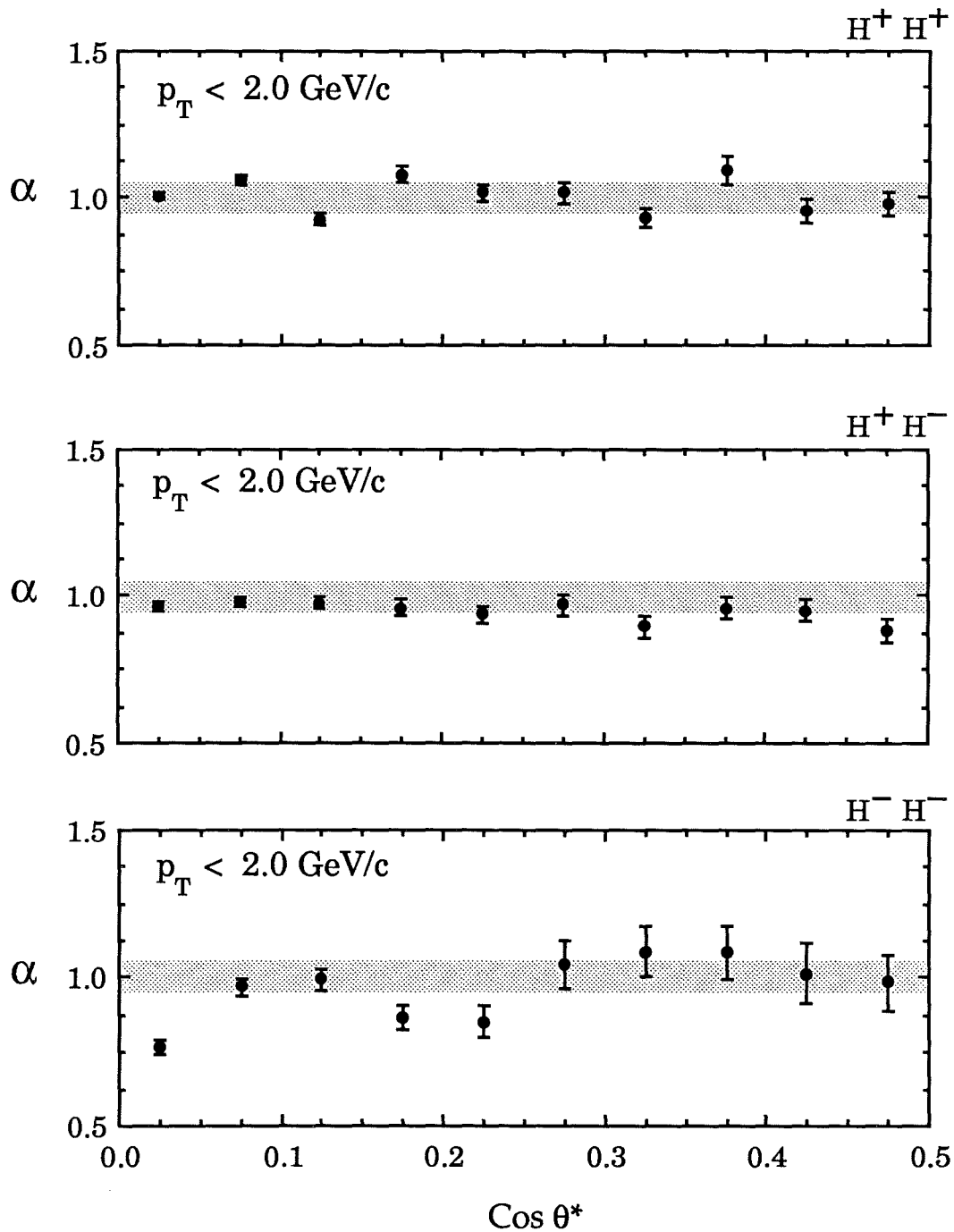


FIGURE 8.8

The atomic weight dependence parameter  $\alpha$  is plotted versus the parton-parton scattering angle for the three charge states in the mass range  $7.0 < M < 7.5 \text{ GeV}/c^2$ . For reference, the value of  $\alpha = 1.0$  is indicated by the shaded area with a width equal to the error in the global average of all the data values.

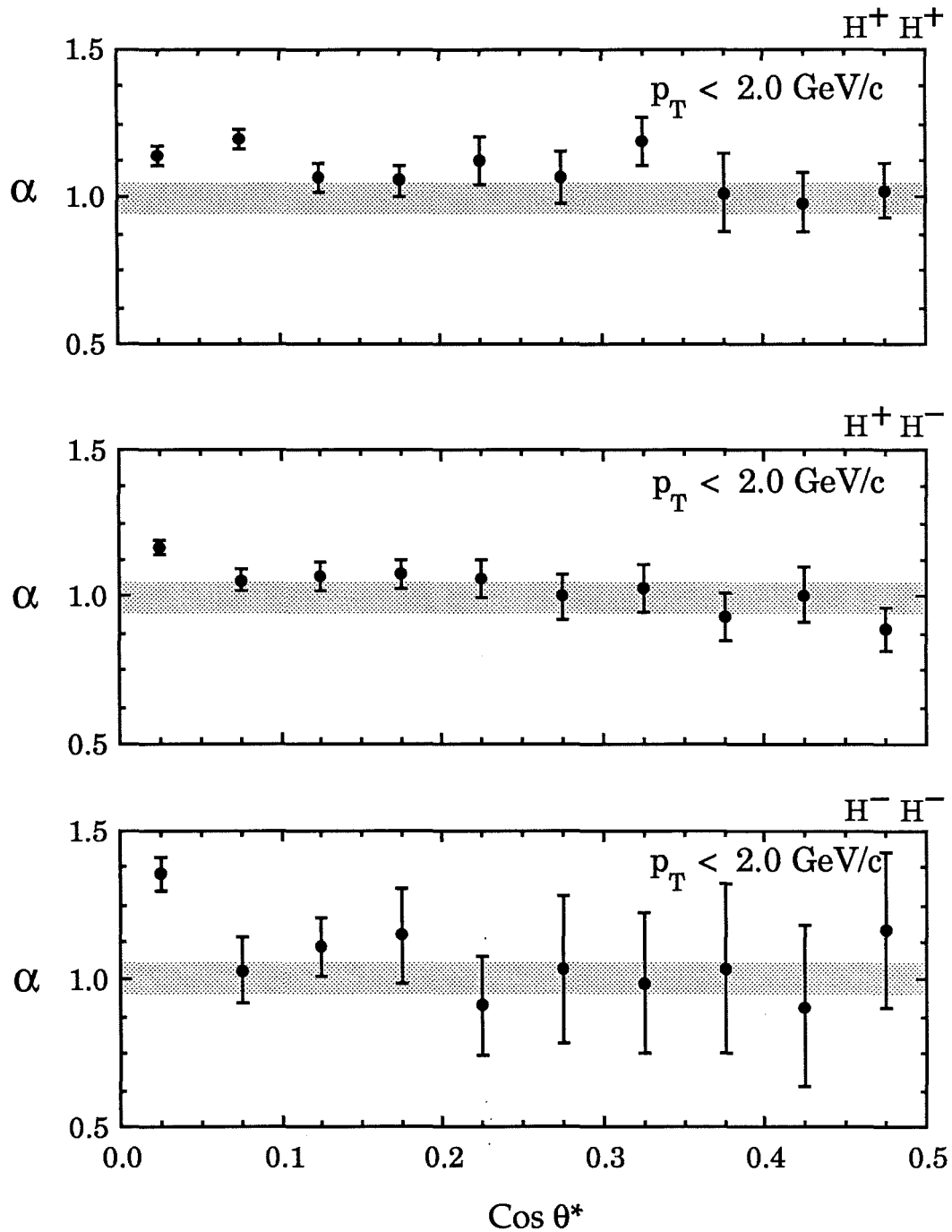


FIGURE 8.9

The atomic weight dependence parameter  $\alpha$  is plotted versus the parton-parton scattering angle for the three charge states in the mass range  $7.5 < M \text{ GeV}/c^2$ . For reference, the value of  $\alpha = 1.0$  is indicated by the shaded area with a width equal to the error in the global average of all the data values.

### **§8.3 The Charge State Dependence and QCD**

In the previous discussion, it has been shown that the distributions are independent of the target type and vary linearly with the value of the atomic weight. To compare the data with QCD Monte Carlo calculations, a functional fit in the power "a" was performed for each set of Monte Carlo results, listed also in Table 8.6. The leading logarithm QCD calculation uses a Monte Carlo routine which incorporates quark and gluon distribution function in nucleons.<sup>69</sup> The  $Q^2$  dependent parton distributions are determined from a variety of data, including deep inelastic structure functions, dimuon mass distributions and  $J/\Psi$   $x_F$  distributions. The results are parametrized for valence quark distributions, sea quark distributions, charm quark distributions and gluon distributions. The parametrizations are written in terms of polynomials which depend on:

$$s = \left[ \frac{\ln(Q^2 / \Lambda^2)}{\ln(Q_0^2 / \Lambda^2)} \right] \quad (8.3)$$

where  $\Lambda$  is the QCD scale parameter set to 200 MeV/c and  $Q^2$  is the factorization scale in the distribution and fragmentation functions. Two particles per event are generated with the capability of specifying various particle types, charge states,  $k_T$  smearing in both the fragmentation and distribution functions, and other processes. The results of the calculations are then treated with the same cuts and limitations as the experimental data, discussed in Chapter 7.

It is observed that the difference in shape (as characterized by the fitting function) between the distributions is small within the limits of the statistical errors. To be able to compare the present data with Monte Carlo results as well as other experimental results in a different quantitative manner, the Kolmogorov-Smirnoff test (K-S) was also applied. One can always modify continuous data by grouping the data in specified bins. This has been done for both the experimental measurement and the Monte Carlo. The accepted test for the difference between binned distributions is the Chi-squared test. For two different data sets  $R_i$  and  $S_i$  binned exactly the same, the Chi-square can be defined as :

$$\chi^2 = \sum_i \frac{(R_i - S_i)^2}{R_i + S_i} \quad (8.4)$$

where each term in the Chi-square is supposed to approximate the square of a normally distributed quantity. A probability function is calculated that depends on the number of degrees of freedom and the Chi-square such that a small probability indicates a significant difference between the distributions. The calculation of the Chi-square for a functional fit to the data would be interpreted as the comparison of the data to a known distribution. In contrast, the K-S test is applicable to unbinned data distributions that can be considered functions of the same independent variable. The assumption is that these data sets are drawn from the same (probability) distribution, so that each of the data points become unbiased estimators of the cumulative distribution functions.<sup>70</sup> However, since the cumulative distribution functions agree at the smallest and largest

allowable value of the independent variable, the behaviour between these limits then distinguishes the distributions. For two different cumulative distribution functions  $S_{N1}(\theta)$  and  $S_{N2}(\theta)$ , the K-S statistic  $D$  can be calculated such that:

$$D = \max_{|\theta|} \left| S_{N1}(\theta) - S_{N2}(\theta) \right| \quad (8.5)$$

where  $D$  is the max value of the absolute difference between the two cumulative distribution functions. Thus in the present data, the K-S test estimates the difference between the two distributions, knowing only that they are functions of the center of mass scattering angle. The results for the comparisons of the data in Figure 8.10 and Figure 8.11 are presented as values of a monotonic function (the significance level probability):

$$Q_{ks}(\lambda) = 2 \sum_{j=1}^{\infty} (-1)^{j-1} e^{-2j^2 \lambda^2} \quad (8.6)$$

which has limits at 0 and 1, where  $\lambda$  is defined for two different distributions of  $(N_1, N_2)$  data points as:

$$\lambda = \sqrt{\frac{N_1 \cdot N_2}{N_1 + N_2}} D \quad (8.7)$$

The function gives the significance level of an observed non-zero value of  $D$  as disproof of the hypothesis that the distributions are the same. Thus small values for this probability indicates a significant difference between the two distributions. This test is meant to compliment other quantitative comparisons.



Figure 8.10 presents a comparison of experimental results from dijet data and E-711 in the range of  $\cos\theta^*$  for the E-711 measurement. Functional fits to the data for UA-1 and UA-2 are nearly identical yielding fit values of "a" of 2.15 and 2.12 respectively. Comparing these two data sets gives a significance level probability of 0.812 (highly correlated). To gauge the sensitivity of the K-S test in this analysis, this value can be compared to the results for the E-711 (+ -) and UA-2 distributions which is 0.656. In fact the data from E-711 and UA-2 should not agree because of the scale variation and the increase of both the running coupling and parton distribution at a fixed x value which cause a steepening of the angular distribution especially for lower energies<sup>42</sup>. This is clearly seen in Figure 8.10. The results of this study are tabulated in Table 8.8 and Table 8.9.

## TABLE 8.8

### Dijet Distribution Comparisons

The comparison of various data showing the difference in the functional fit parameter "a" of eq (8.1) and the significance level probability results from application of the Kolmogorov- Smirnoff test illustrated in Figure 8.10.

Experiment → ↓	UA-1	UA-2	CDF	E711 (+ -)
UA-1	1	0.81	0.27	0.58
UA-2	$\Delta a = 0.03$	1	0.18	0.66
CDF	$\Delta a = 0.08$	$\Delta a = 0.11$	1	0.18
E711 (+ -)	$\Delta a = 0.67$	$\Delta a = 0.70$	$\Delta a = 0.59$	1
"a"	$2.15 \pm 0.04$	$2.12 \pm 0.02$	$2.23 \pm 0.17$	$2.82 \pm 0.05$

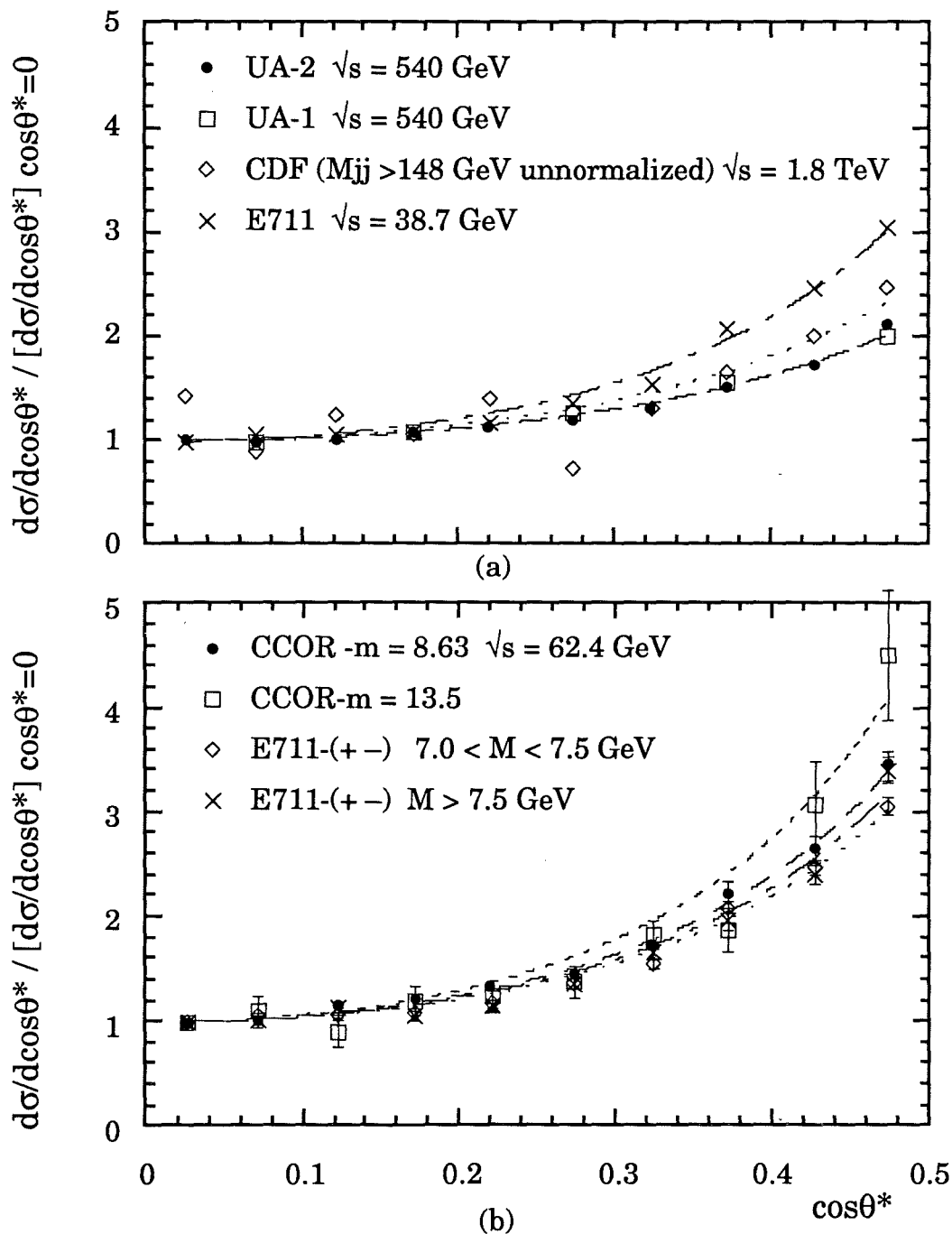


FIGURE 8.10

A comparison of the E711 data to dijet data from: (a) UA-1 ; UA-2 and CDF experiments and (b) CCOR neutral di-pion experiment. The E711 data in (a) corresponds to the (+ -) charge state in the mass range  $7.0 < M < 7.5$  GeV/c<sup>2</sup>. The curves correspond to a functional fit to the normalized cross sections of the form (8.1) in the range of the scattering angle shown.

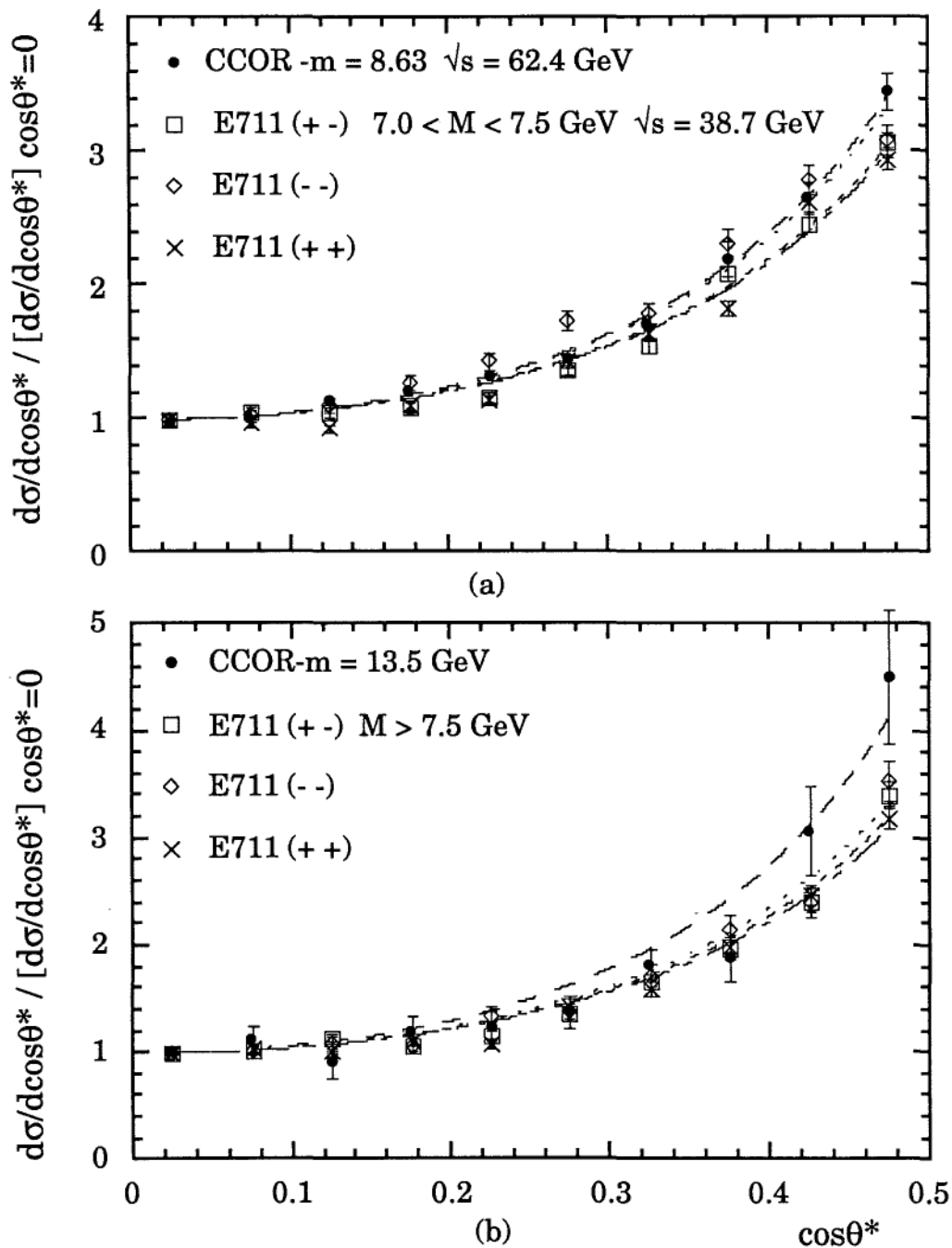


FIGURE 8.11

The dihadron angular distributions as a function of the charge state for E711, and the neutral dipion data from the CCOR experiment. The curves correspond to a functional fit to the normalized cross sections of the form (8.1).

**TABLE 8.9****Charge Dependence Chart**

The comparison the data showing the difference in the functional fit parameter "a" of eq (8.1) and the significance level probability results from application of the Kolmogorov - Smirnov test to the parton-parton distributions based upon the charge state. The data is also compared to a data set of CCOR  $\pi^0$ - $\pi^0$  angular distributions.

		CCOR ( $\sqrt{s}$ = 62.4 GeV)		E711 M < 7.5 GeV		E711 M > 7.5 GeV			
		M=8.63 GeV	M=13.5 GeV	(+ -)	(- -)	(+ +)	(+ -)	(- -)	(+ +)
CCOR	M=8.63 GeV	1	0.76	0.99	0.76	0.99	0.76	0.99	0.76
	M=13.5 GeV	$\Delta a = 0.31$	1	0.99	0.99	0.76	0.99	0.99	0.76
E711 M<7.5 GeV	(+ -)	$\Delta a = 0.07$	$\Delta a = 0.38$	1	0.40	0.76	0.76	0.76	0.76
	(- -)	$\Delta a = 0.16$	$\Delta a = 0.47$	$\Delta a = 0.09$	1	0.40	0.99	0.99	0.40
	(+ +)	$\Delta a = 0.02$	$\Delta a = 0.33$	$\Delta a = 0.05$	$\Delta a = 0.14$	1	0.40	0.40	0.76
E711 M>7.5 GeV	(+ -)	$\Delta a = 0.44$	$\Delta a = 0.13$	$\Delta a = 0.51$	$\Delta a = 0.60$	$\Delta a = 0.46$	1	0.99	0.99
	(- -)	$\Delta a = 0.87$	$\Delta a = 0.56$	$\Delta a = 0.94$	$\Delta a = 1.03$	$\Delta a = 0.89$	$\Delta a = 0.43$	1	0.76
	(+ +)	$\Delta a = 0.92$	$\Delta a = 0.61$	$\Delta a = 0.99$	$\Delta a = 1.08$	$\Delta a = 0.94$	$\Delta a = 0.48$	$\Delta a = 0.05$	1
"a"		2.89 $\pm 0.11$	3.20 $\pm 0.13$	2.82 $\pm 0.05$	2.73 $\pm 0.13$	2.87 $\pm 0.09$	3.33 $\pm 0.09$	3.76 $\pm 0.21$	3.81 $\pm 0.14$

A particular charged meson is preferentially produced from a particular type (or flavor) of fragmenting parton (u-quark into positive hadrons and d-quarks into negative hadrons), and it is predicted from QCD calculations that the quark scattering is charge independent. Even though this result shows some difference in the charge state dependence of the angular distribution from two similar tests, absolute distinction between the distributions for the charged state as well as from the neutral state can not be established. The small changes in the distributions might be explained by contributions to the valence quark-valence quark ( $qq - qq$ ) scattering, from other parton subprocesses. Then changes in the shape of the angular distribution may be a direct result of these other processes, such as different amount of gluon contributions. In fact the measured angular distributions are a weighted average over the angular distributions of these subprocesses, such as gluon-valence quark ( $gq - gq$ ), and gluon-gluon ( $gg-gg, gg-qq$ ) scattering. The distributions from these processes have nearly the same shape, and therefore their contributions can not be separately measured, but a linear combination of the various charge states in the present data would emphasize the major contribution to the cross section from ( $qq$ ) scattering.

For the proton composed of (uud) valence quarks and the neutron composed of (udd) valence quarks, and assuming that the dominant contribution to the cross section comes from qq interactions, estimates of the contribution to the cross section from various parton pair interactions can be made. Subprocess ratios are shown in Table 8.10 for meson charge states from parton scattering in hadron collisions. It is clear that the valence only approximation does not include all the parton contributions to the scattering, but just the value of these three subprocesses can be appropriately compared to the data. These calculations are derived from the QCD monte Carlo previously mentioned.

**TABLE 8.10**

**Subprocess Charge Ratios**

The parton contribution ratios for the production of two charged mesons from pn scattering on an aluminum target.

Dihadron Mass	Charge State	qq $\rightarrow$ qq	qg $\rightarrow$ qg	gg $\rightarrow$ gg
7.0 GeV/c <sup>2</sup>	+ + / + -	1.14	1.00	0.85
	+ + / - -	1.35	0.95	0.66
14.0 GeV/c <sup>2</sup>	+ + / + -	1.04	0.88	0.68
	+ + / - -	1.12	0.63	0.35

Figure 8.12 shows the ratio of the angular distributions as a function of the scattering angle and charge state. In both mass ranges the ratio of the like-signed charged states differ by a factor of  $\approx 2$  from the ratio of the same sign to opposite sign cross sections. In the case of the high mass range of the data, the average values are  $h^+h^+ / h^-h^- = 2.30 \pm 0.18$  and  $h^+h^+ / h^+h^- = 1.17 \pm 0.06$ , and in the low mass bins the average values are  $h^+h^+ / h^-h^- = 2.00 \pm 0.16$  and  $h^+h^+ / h^+h^- = 0.90 \pm 0.06$ . The p-p collisions will predominantly produce  $\pi^+$  over  $\pi^-$  because there are twice as many u quarks as d quarks in the initial state collisions. In the p-n collisions the initial state is symmetric in u and d quarks, and also pure gluonic interactions and charge symmetric processes would contribute equally to the charge production of the hadrons. Thus the production rate should be the same, which of course leads to a value near 1.0 for unlike-sign to like-sign ratios as seen. The unlike-sign to like-sign ratio higher value can be due to the higher momentum fraction that the u quark carries relative to the d quark in the proton, resulting in a larger momentum transfer to the leading  $\pi^+$  after the scattering. Although the data ratios differ from the QCD results for specific processes, how they should combine requires further study. Contributions to the cross section from other processes would cause deviations to this ratio from the expected values resulting from just valence quark scattering.

It is thought that the t-channel exchange of gluons may predict a distribution that varies approximately as the Rutherford cross section,  $dN/d\cos\theta^* \sim \sin^{-4} \theta^*/2$ . The Mandelstam variables can be expressed in terms of  $\theta^*$ . Namely :

$$\hat{t} = \frac{\hat{s}}{2}(1 - \cos\theta^*) \qquad \hat{u} = \frac{\hat{s}}{2}(1 + \cos\theta^*)$$

When expressed in terms of the variable  $\chi = (1 + \cos\theta^*)/(1 - \cos\theta^*)$ , leading order QCD also is consistent with the distribution at small  $\chi$  and predicts an approximate constant result at large  $\chi$ . To further investigate the dependence on the charge state as well as to test this comparison, the data are plotted as this type of distribution and shown in Figure 8.13. The features at small values of  $\chi$  are consistent with the expectations of QCD, for the charge states that have at least one positive hadron component. The negative like-sign data is inconclusive in this distribution comparison. The curves shown are generated from the QCD Monte Carlo results and expressed also in term of the variable  $\chi$ .



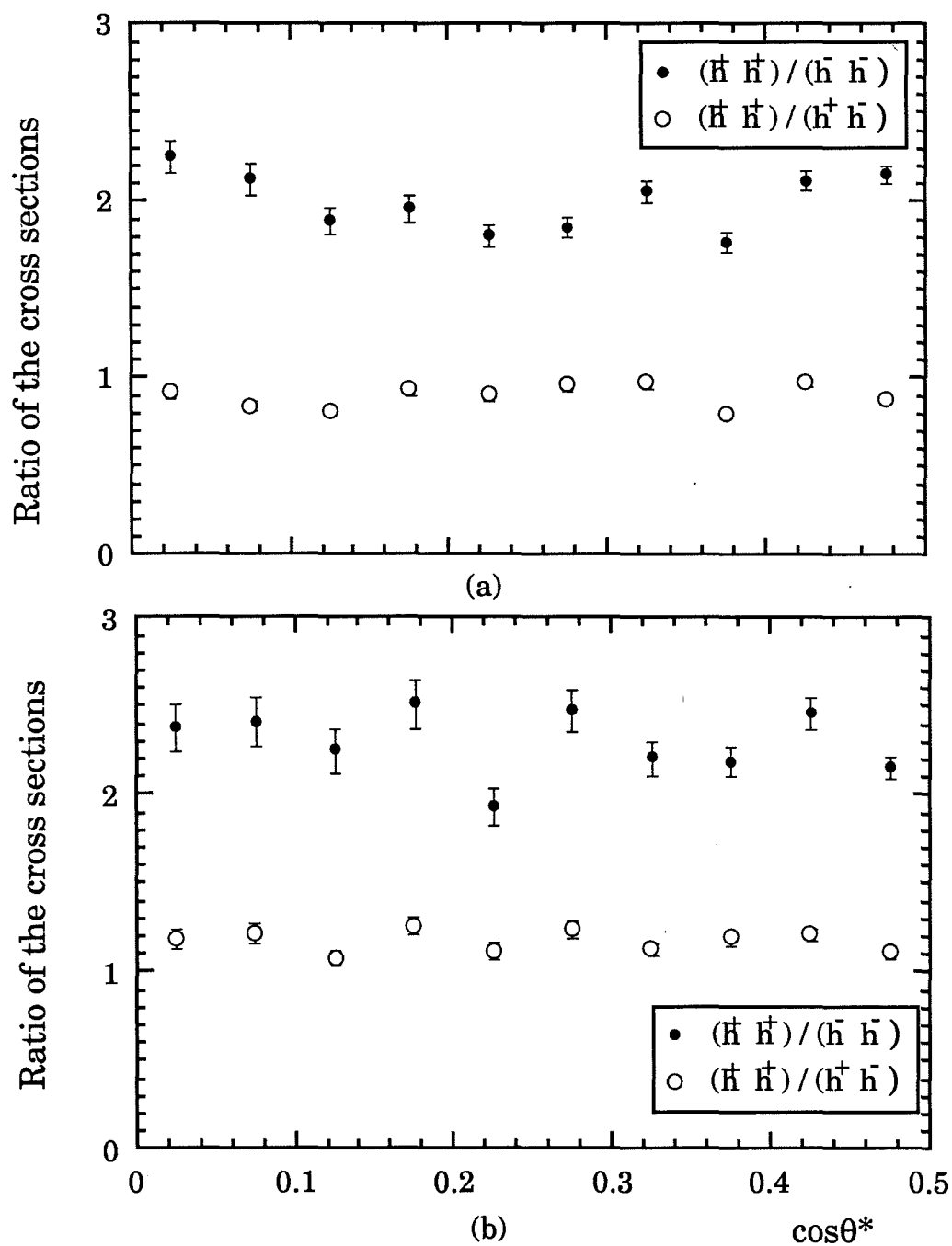


FIGURE 8.12

The ratio of the angular distributions as a function of the parton-parton scattering angle, and charge state. Figure (a) corresponds to the mass range  $7.0 < M < 7.5 \text{ GeV}/c^2$ , while (b) covers the mass range data  $M > 7.5 \text{ GeV}/c^2$ .

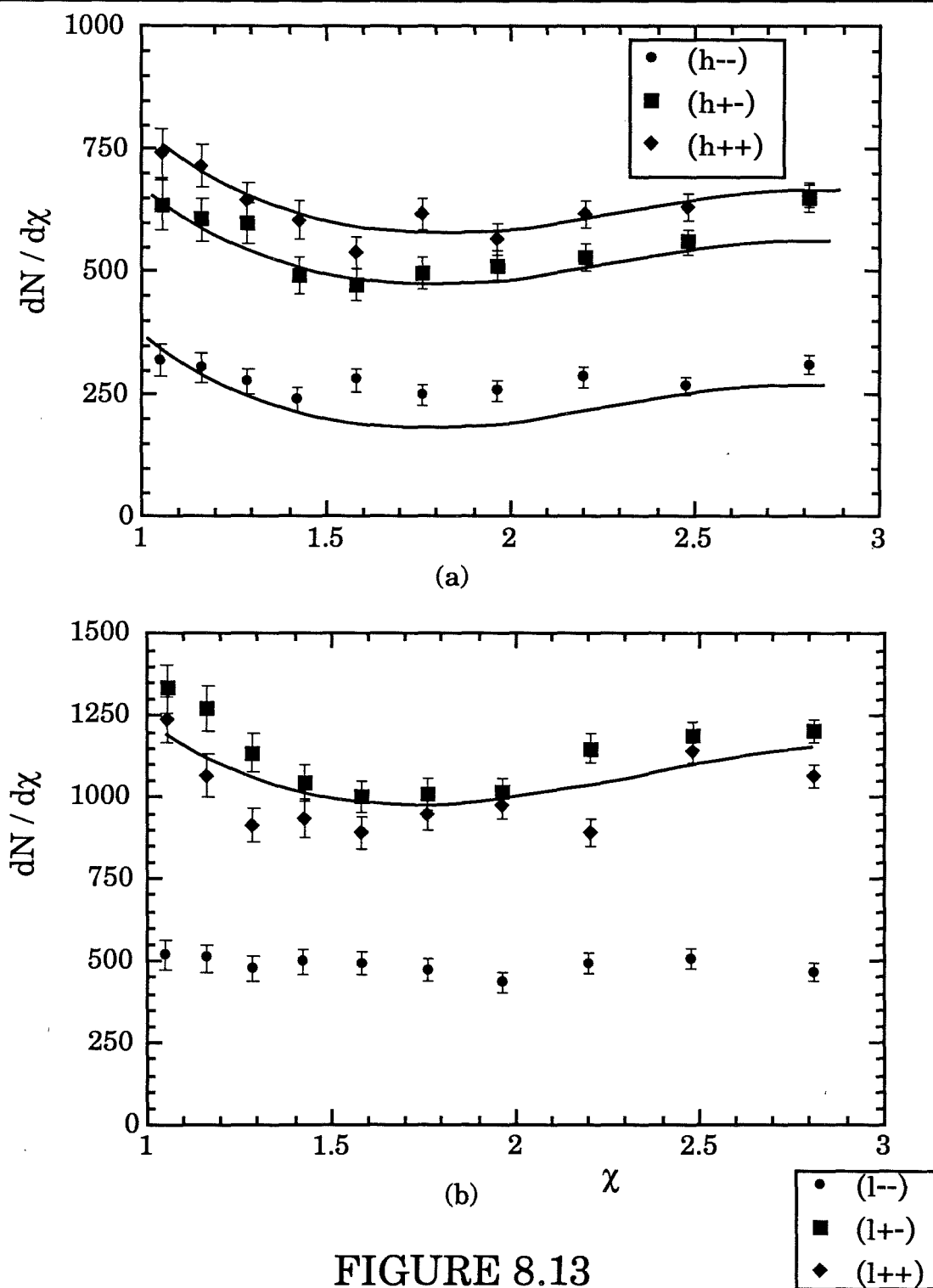


FIGURE 8.13

The angular distributions plotted as a function of the variable  $\chi$  and charge state. Figure (a) corresponds to the mass range  $7.0 < M < 7.5 \text{ GeV}/c^2$ , while (b) covers the mass range data  $M > 7.5 \text{ GeV}/c^2$ .

## CHAPTER 9

### CONCLUSIONS

The angular distribution of hadron pairs produced in the interaction of 800 GeV/c protons on targets of aluminium, beryllium, iron and tungsten have been measured, inferring the underlying dynamics of parton-parton scattering in these interactions. The transverse momentum hadrons with  $p_T < 2.0$  GeV/c are studied in three charge states,  $(++)$ ,  $(+-)$ ,  $(--)$  covering the dihadron mass range of 7 to 15 GeV/c<sup>2</sup> and scattering angles up to  $\cos \theta^* = 0.50$ . To compare the data internally and with other experiments, functional fits to the data were performed, and differences in the fitting parameter for each set of data was examined. Each set of the data was normalized by the total integrated cross section over the range of  $\cos \theta^*$ , and into mass bins of  $7.0 < M < 7.5$  GeV/c<sup>2</sup> (low) and  $7.5 < M$  GeV/c<sup>2</sup> (high). Double hard scattering within the nucleon might be detected by a shift in the transverse momentum spectrum and a change in the angular distribution as a function of the target mass. Within our limited  $p_T$  region the parton-parton angular distributions are found to be independent of the target type based upon the same fitting form to each distribution. Although the relative value of the results differ for the two mass bins, within errors little deviation was seen across target types within mass bins.

The cross section as a function of the parton-parton scattering angle for the three charge states is shown to vary linearly with the value of the atomic weight when the cross section is parametrized as  $\sigma(A) = \sigma_0 A^\alpha$ . The value of  $\alpha$  is measured to be  $1.018 \pm 0.009$  for a global fit to the data over the full  $\cos\theta^*$  range of the analysis.

Being independent of the target type and the atomic mass, the data was integrated to produce results that were distinguished by mass state and charge state. Using the Kolmogorov - Smirnov test, as well as functional fits to the normalized data, the (+ -) distributions were compared to other low  $x$  dijet results in the range of  $\cos\theta^*$  for this experiment and found to deviate significantly by more than 0.5 in the value of the fitting parameter  $a$ , as expected. This also corresponded to values ranging from 0.18 to not more than 0.65 in the significance level probability from the K-S test for any of the data comparisons with this experiment, where 1.0 is considered highly correlated. The dihadron angular distributions for these data and with regards to the neutral dipion state angular distributions from the CCOR results, shows only a small dependence on the charge state within the statistical significance of the data.

The ratio of the cross sections for different charge states as a function of the parton-parton scattering angle is found to be uniform and generally agree with the predictions of leading log QCD calculations for the subprocesses thought to be dominant in the hard scattering for individual processes. The average value for the unlike sign ratios (2.30 at

the higher mass, and 2.0 at the lower mass range) are found to deviate from the expected values. For the like-sign to unlike-sign ratios, the average values are generally consistent with expectations, based purely on the valence quark content of the nucleons. These results are generally consistent with the assumption that the contribution to the cross section from parton-parton scattering at these energies and  $p_T$  region will come primarily from a variety of subparticle contributions to the interaction and that the individual processes compared here would not alone account for the charge ratios observed.

Without particle identification in the final state, it is not possible to distinguish between certain hard processes (such as  $uu \rightarrow uu$ ,  $ug \rightarrow ug$ , etc.) that are correlated with  $\pi^\pm$  and  $K^\pm$ . However since the t-channel exchange of gluons dominates the small angle scattering, and corresponds approximately to the Rutherford scattering shape of the distributions, some information may be gained by observing any deviation in the shapes as a function of the charge state. In both mass ranges, the  $(+ -)$  and the  $(+ +)$  charge states show consistent shapes. Possibly due to the depleted number of events, the  $(- -)$  charge state indicates less consistency with the expected shape especially in the low mass data.

## APPENDIX A

### DI-HADRON SCATTERING FORMALISM

This appendix presents the details of some formalism that relates the dynamics that are measured at the hadron-hadron level with the underlying dynamics that can be inferred from hadronic constituent interactions. In the following notation hadrons will be designated by uppercase letters and lowercase letters will designate particle constituents at the parton level.

#### §A.1 The Di-Hadron Process

In the symmetric di-hadron production process, one starts with two incident hadrons A and B, which collide and produce two outgoing hadrons  $H_1$  and  $H_2$ , due to the parton interaction within the incident particles (see Figure 2.3). The outgoing hadrons will have a longitudinal momentum component ( $P_\ell$ ), and an expected large transverse momentum component ( $p_T$ ), with respect to the beam direction. It is possible therefore to define the rapidity of the hadron particle is defined as:

$$Y = \frac{1}{2} \ln \left( \frac{E + P_\ell}{E - P_\ell} \right), \quad (\text{A.1})$$

where  $E$  is the total energy, and the scaled momentum fractions are:

$$x_T = 2 p_T / \sqrt{s} \quad .$$

If the center of mass energy is  $\sqrt{s} = P_A + P_B$  then, in the hadron-hadron center of mass, the four momentum can be written:

$$\begin{aligned} P_A &= \frac{\sqrt{s}}{2} (1, 0, 0, 1) \\ P_B &= \frac{\sqrt{s}}{2} (1, 0, 0, -1) \quad , \end{aligned} \quad (A.2)$$

and at the parton level, similar equations for the momentum are:

$$\begin{aligned} p_a &= x_a \frac{\sqrt{s}}{2} (1, 0, 0, 1) \\ p_b &= x_b \frac{\sqrt{s}}{2} (1, 0, 0, -1) \\ p_c &= p_{t_c} (\cosh y_1, 1, 0, \sinh y_1) \\ p_d &= p_{t_d} (\cosh y_2, -1, 0, \sinh y_2) \quad . \end{aligned} \quad (A.3)$$

The Mandelstam variables at the parton level can then be written as:

$$\begin{aligned} \hat{s} &= x_a x_b s \\ \hat{t} &= -x_a p_t \sqrt{s} e^{-y_1} \\ \hat{u} &= -x_b p_t \sqrt{s} e^{+y_1} \end{aligned} \quad (A.4)$$

where for example the rapidity for the outgoing particle  $c$  is  $y_1$ .

The differential cross section for the collision of two particles ( $i=1,2$ ) with relative collinear velocity  $v_{rel}$  and producing  $N$  final state particles ( $f=1,2,...,N$ ) is given by :<sup>71</sup>

$$d\sigma = (2\pi)^4 \delta^{(4)} \left( \sum p'_f - \sum p_i \right) \frac{1}{4E_1 E_2 v_{\text{rel}}} \left( \prod_{\ell} (2m_{\ell}) \right) \left( \prod_f \frac{d^3 \mathbf{P}'_f}{(2p)^3 2E_f} \right) |\mathcal{M}|^2. \quad (\text{A.5})$$

Therefore the invariant cross section for producing two large transverse momentum hadrons can be formulated with the following approach.<sup>2</sup>

Starting at the parton level:

$$d\sigma(A+B \rightarrow c+d) = \frac{1}{2\hat{s}} \sum_{ab} G_{a/A}(x_a) G_{b/B}(x_b) dx_a dx_b \sum |\mathcal{M}(a+b \rightarrow c+d)|^2 (2\pi)^4 \delta^4(p_a + p_b - p_c - p_d) \frac{d^3 p_c}{(2\pi)^3 2E_c} \frac{d^3 p_d}{(2\pi)^3 2E_d} \quad (\text{A.6})$$

If the cross section for the two body parton scattering process is denoted by:

$$\frac{d\sigma}{d\hat{t}}(a+b \rightarrow c+d) = \frac{1}{16\pi \hat{s}^2} \sum |\mathcal{M}(ab \rightarrow cd)|^2$$

with  $\frac{d^3 p_c}{2E_c} = \frac{1}{z_1^2} \frac{d^3 P_{H_1}}{2E_1}$  and  $\frac{d^3 p_d}{2E_d} = \frac{1}{z_2^2} \frac{d^3 P_{H_2}}{2E_2}$

where  $\mathbf{z}$  specifies the fraction of the outgoing momentum carried by the hadron  $\mathbf{H}$ , then the form of the di-hadron production can be written:



$$\begin{aligned}
& E_C E_D \frac{d^6 \sigma}{dp_c^3 dp_d^3} (A+B \rightarrow C+D+X) = \\
& \sum_{abcd} \int dx_a dx_b G_{a/A}(x_a, Q^2) G_{b/B}(x_b, Q^2) D_{C/c}(z_c, Q^2) D_{D/d}(z_d, Q^2) dz_c dz_d \\
& \frac{1}{z_c^2 z_d^2} \frac{\hat{s}}{2\pi} \frac{d\sigma}{d\hat{t}} (a+b \rightarrow c+d) \delta^4(p_a + p_b - p_c - p_d) \quad . \quad (A.7)
\end{aligned}$$

The fragmentation function  $D_{H/q}$  when multiplied by  $dz_q$  gives the probability for obtaining a hadron  $H_q$  from parton  $q$  with the hadron carrying a  $z_q$  fraction of the parton's momentum. The leading outgoing hadron also determines the direction of the associated collinear particles which defines a jet.

## §A.2 The Angular Distribution

If  $M$  and  $Y$  are the invariant mass and the rapidity of the di-hadron system at the hadron level respectively, and  $\eta$  is the transverse momentum imbalance between the two outgoing hadrons, then one can relate the di-hadron system and the di-jet system to extract parton angular distributions. Consider the relations:<sup>72</sup>

$$M^2 = z_1 z_2 M_J^2$$

$$\eta = (P_{H1} - P_{H2}) = p_{TJ} (z_1 - z_2)$$

$$Y_J = Y + \ln \frac{M_T}{M} - \ln \left[ \sqrt{\frac{z_1}{z_2} \frac{1 + \cos \theta^*}{2}} + \sqrt{\frac{z_2}{z_1} \frac{1 - \cos \theta^*}{2}} \right]$$

with  $M_T = \sqrt{M^2 + \eta^2}$  (A.8)

where the subscript **J** denotes the di-jet system and  $\theta^*$  is the parton-parton center-of-mass scattering angle.

If the two jets have balancing transverse momentum, then :

$$p_{TJ}^2 = \frac{M_J^2}{4} (1 - \cos^2 \theta^*)$$

or equivalently  $\frac{2}{\sin \theta^*} = \frac{M_J}{p_{TJ}}$  . (A.9)

This leads to the following differential cross section:

$$\frac{d^4 \sigma}{dM^2 dY d\eta d\cos \theta^*} = \int \frac{d^4 \sigma}{dM_J^2 dY_J d\eta d\cos \theta^*} dM_J^2 dY_J dz_1 dz_2$$

$$D_{H_{1/j1}}(z_1) D_{H_{2/j2}}(z_2) \delta \left( M^2 - z_1 z_2 M_J^2 \right) \delta \left[ \eta - (z_1 - z_2) p_{TJ} \right]$$

$$\delta \left[ Y_J - Y - \ln \frac{M_T}{M} + \ln \left( \sqrt{\frac{z_1}{z_2} \frac{1 + \cos \theta^*}{2}} + \sqrt{\frac{z_2}{z_1} \frac{1 - \cos \theta^*}{2}} \right) \right] \quad .(A.10)$$

Integrating over the three delta functions results in a simpler correlation between the di-hadron cross section and the di-jet cross section. Namely:

$$\frac{d^4\sigma}{dM^2 dY d\eta d\cos\theta^*} = \int \frac{2}{z_1 P_{tJ}(z_1 + z_2)} dz_1 D_{H_{1/c}}(z_1) D_{H_{2/d}}(z_2) \frac{d^3\sigma}{dM_J^2 dY_J d\cos\theta^*} , \quad (A.11)$$

where the jet cross section is given by :

$$\frac{d^3\sigma}{dM_J^2 dY_J d\cos\theta^*} = \frac{x_a x_b}{2} \sum_{abcd} G_{a/A}(x_a, Q^2) G_{b/B}(x_b, Q^2) \frac{d\sigma}{d\hat{t}}(a + b \rightarrow c + d)$$

with  $x_a = \frac{M_J}{\sqrt{s}} e^{+Y_J}$  ,  $x_b = \frac{M_J}{\sqrt{s}} e^{-Y_J}$  . (A.12)

A general relation therefore can be written:

$$\frac{d^4\sigma}{dM^2 dY d\eta d\cos\theta^*} = \sum_{abcd} \int \frac{2}{\sin\theta^*} dx_a dx_b \frac{1}{s} \frac{1}{z_1(z_1 + z_2)} G_{a/A}(x_a) G_{b/B}(x_b) \frac{d\sigma}{d\hat{t}} D_{H_{1/c}}(z_1) D_{H_{2/d}}(z_2) . \quad (A.13)$$

In a region where the rapidity and momentum imbalance are held constant, one can directly relate the angular distribution over particular mass bins with the parton-parton scattering cross section.

The treatment presented assumes collinear kinematics. To include the effects due to  $k_T$  smearing, one redefines the scaled momentum fractions and the parton four vectors as:

$$x_a = (E_a + p_{a\ell}) / \sqrt{s} \quad .$$

$$\text{and} \quad p_a = (E_a, \vec{k}_{Ta}, p_{a\ell})$$

$$\text{where} \quad E_a = \frac{1}{2} \left( x_a \sqrt{s} + \frac{k_{Ta}^2}{x_a \sqrt{s}} \right)$$

$$p_{a\ell} = \frac{1}{2} \left( x_a \sqrt{s} - \frac{k_{Ta}^2}{x_a \sqrt{s}} \right)$$

There are similar expressions for partons b, c and d. Using the average transverse momentum,  $\langle k_T \rangle$  and making allowances for the proper direction of the longitudinal momentum, a cross section can be evaluated with the  $k_T$  effects included. In Eq. (A.7) the modified distribution functions for partons a and b to include the  $k_T$  smearing function can be written :

$$E_C E_D \frac{d^6 \sigma}{dp_c^3 dp_d^3} (A+B \rightarrow C+D+X) =$$

$$\sum_{abcd} \int dx_a d^2 k_{Ta} f(\vec{k}_{Ta}) G_{a/A} dx_b d^2 k_{Tb} f(\vec{k}_{Tb}) G_{b/B} D_{C/c} D_{D/d} dz_c dz_d$$

$$\frac{1}{z_c^2 z_d^2} \frac{\hat{s}}{2\pi} \frac{d\sigma}{d\hat{t}} (a+b \rightarrow c+d) \delta^4(p_a + p_b - p_c - p_d) \quad .$$

where the distribution and the fragmentation functions depend on the momentum fraction and  $Q^2$ . The eight dimensional integral is usually carried out by Monte Carlo techniques.

## APPENDIX B

### BEAM AND TARGET DIMENSIONS

This appendix presents the details of the beam monitoring calculations for the horizontal beam size and the vertical range of the beam at the experimental target.

#### **§B.1 The Horizontal Beam Focus**

The horizontal beam focus and the maximum targeting intensity was attained by successively adjusting the quadrupole strengths of the NECQ quadrupole magnets, thereby adjusting the focus and then sweeping the beam across the target using the NECH dipole magnet, until the luminosity was maximized. The target scans of Figure 3.7, the calibration of the sweeping magnet NECH (6.29 amp/mm) and the horizontal width of the target which were manufactured to be  $\approx 1$  mm, are the parameters used to calculate an operational width of the beam. The tungsten target was used for this scan and the distribution for any of the luminosity monitors can be used for this calculation. The east edge of the beam strikes the west edge of the target at the values of the lower edge of the distribution (at NECH = 2.0 amps). The values of the upper edge of the distribution corresponds to the west edge of the beam striking the east target edge (NECH = 20 amps). Subtracting the target width and converting the units therefore yields a beam width as follows:

$$\text{beam width} = \left[ \frac{(20.0 - 2.0) \text{ amps}}{6.29 \text{ amps/mm}} - 1 \text{ mm} \right] * \frac{1}{2} = 0.93 \pm 0.02 \text{ mm} \quad (\text{B.1})$$

## **§B.2 The Vertical Beam Range**

The following calculation was done to verify that the interactions that were observed, were produced by the target and not by additional materials upstream of the experimental hall. The analysis of this measurement also established the range of the beam in the vertical plane. Unlike the horizontal magnet, vertical magnet calibrations for these scans could not be done in the same way since quadrupole magnets were situated between the vertical sweeping magnet (NEBV) and the target station. However, using the excitation formulae<sup>73</sup> for the dipole and the quadrupole magnets, and knowing the position of these magnets, allows one to do a geometric calculation of the vertical target height that can be compared to the manufactured height of the target (5.72cm  $\pm$  .02 cm).

In a bending magnet with a constant magnetic field **B**, the total angle of bend between the entrance and exit angles on an ideal orbit can be approximated as:

$$\alpha \equiv \frac{\int \mathbf{B} \, d\mathbf{l}}{3.33\mathbf{p}} \quad (\text{B.2})$$

where **p** is the momentum in GeV/c, **B** is the magnetic field in Tesla, and **l** the magnetic length in meters, giving the total angle  $\alpha$  in radians. The relational formulae for the NEBV dipole (field gap is 4 in x 4in x 30in long) are given below:

$$\begin{aligned}
B_T &= 0.4377 P_{\text{GeV/c}} \theta_{\text{mr}} \\
\theta_{\text{mr}} &= 2.284 B_T / P_{\text{GeV/c}} \\
I_A &= 4.0 B_T
\end{aligned} \tag{B.3}$$

where  $I_A$  is the current in the magnet in amps.

The relational formula for the NECQ quadrupoles ( with a  $7.62 \pm 0.02$  cm circular radius and a combined magnetic length of  $3.45 \pm 0.05$  meters) are as follows:

$$I_A = 185.20 \text{ G (Tesla/meters)} \tag{B.4}$$

where  $G$  is the field gradient.

Figure B.1 shows the geometry of the beam trajectory from the vertical plane bending point at NEBV through the NECQ quadrupoles to the vertical plane at the target station. From Figure 3.8 the magnet current range of the NEBV dipole is shown to be approximately 225 amps. This current is converted to a magnetic field strength and then an angular deflection for an 800 GeV/c proton beam. Since the beam does not pass through the vertical defocusing quadrupoles (NECQ) on axis, an additional deflection is experienced due to the quadrupoles. The angle  $\theta_B$  in milliradians is the angular deflection due to the NEBV magnet.

$$\theta_B = \frac{1}{2} \left[ 2.284 \left( \frac{I_A}{4.0} \right) / P_{\text{GeV/c}} \right] = 0.080 \text{ mr} \tag{B.5}$$

This implies that the beam is deflected  $\pm 1.049$  cm away from the symmetry axis at the NECQ quadrupoles. The magnets NECQ, were energized at a current of 2786 amps, which produces a field gradient of 15.04 T/m, and an



off axis field of 0.158 T. The additional angular deflection using the equation B2 above is calculated to be  $\theta_C = 0.204$  mr. Therefore the sum of these two angular deflections will displace the beam vertically a range of 5.81 cm, whereas the actual target is 5.72 cm. This calculation over estimates the target size by 1.6% over a distance of 196 meters between the vertical magnet and the target.

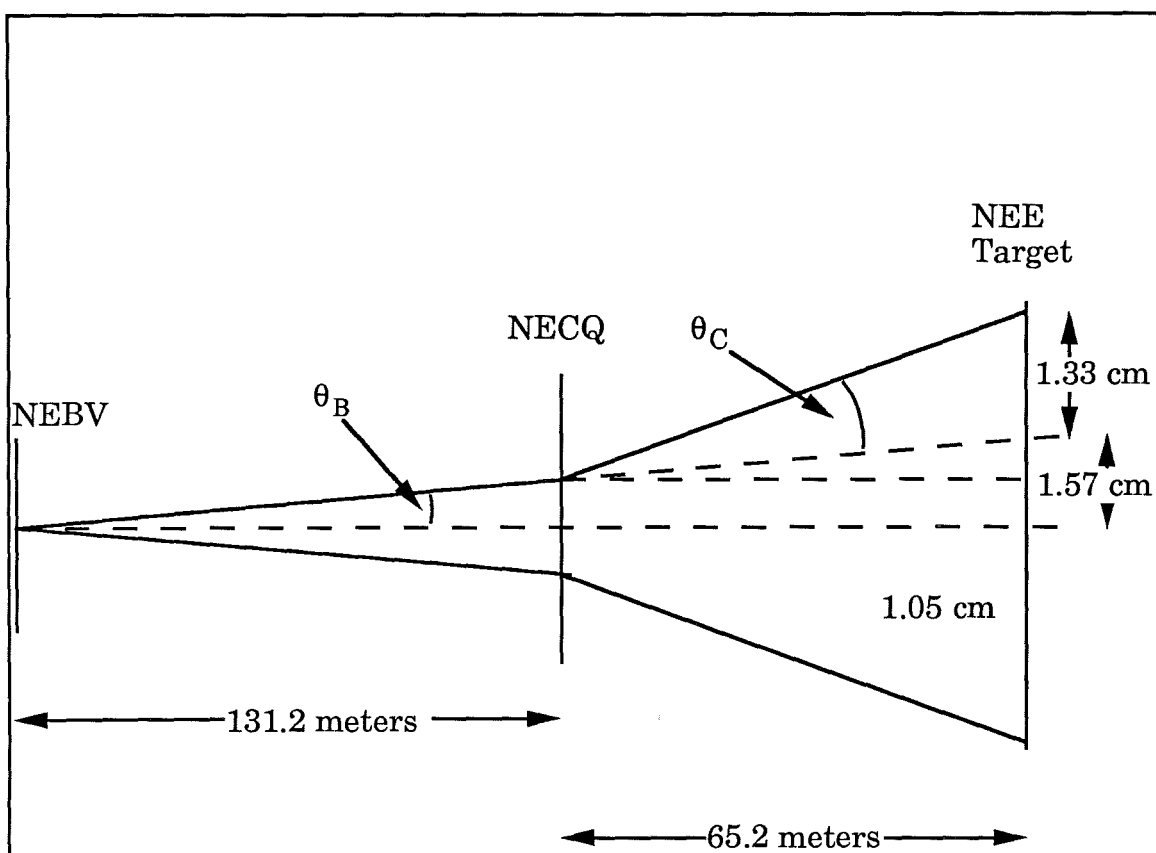


FIGURE B.1

Vertical Plane Beam Geometry for the angular  
deflection from the Vertical bending Magnet  
NEBV to the E-711 target

## APPENDIX C

### SELECTED DETECTOR ELECTRONIC CIRCUITS

This appendix catalogues some details of the electronic circuits for the drift chamber operation and the calorimeter operation.

Figure C.1 shows the circuit diagram for a single channel for the pre-amplifier circuit and associated circuit for testing.<sup>74</sup> These circuits were successfully used to amplify the signal from the drift chamber sense wire by a factor of 20, before further amplification was performed by a 16 channel amplifier shown in Figure C.2. To reduce the noise in the pre-amplifier, each physical system was shrouded in copper tape (effectively a Faraday cage) to shield the circuits from the local electronic noise of the laboratory.

The schematic diagrams for the photo multiplier bases used in the hodoscope and the calorimeter are shown in Figure C.3. The calorimeter used the ten stage, gain adjusted R2154 base shown in part (a) of the figure, while the hodoscope used the 12 stage base shown in part (b).

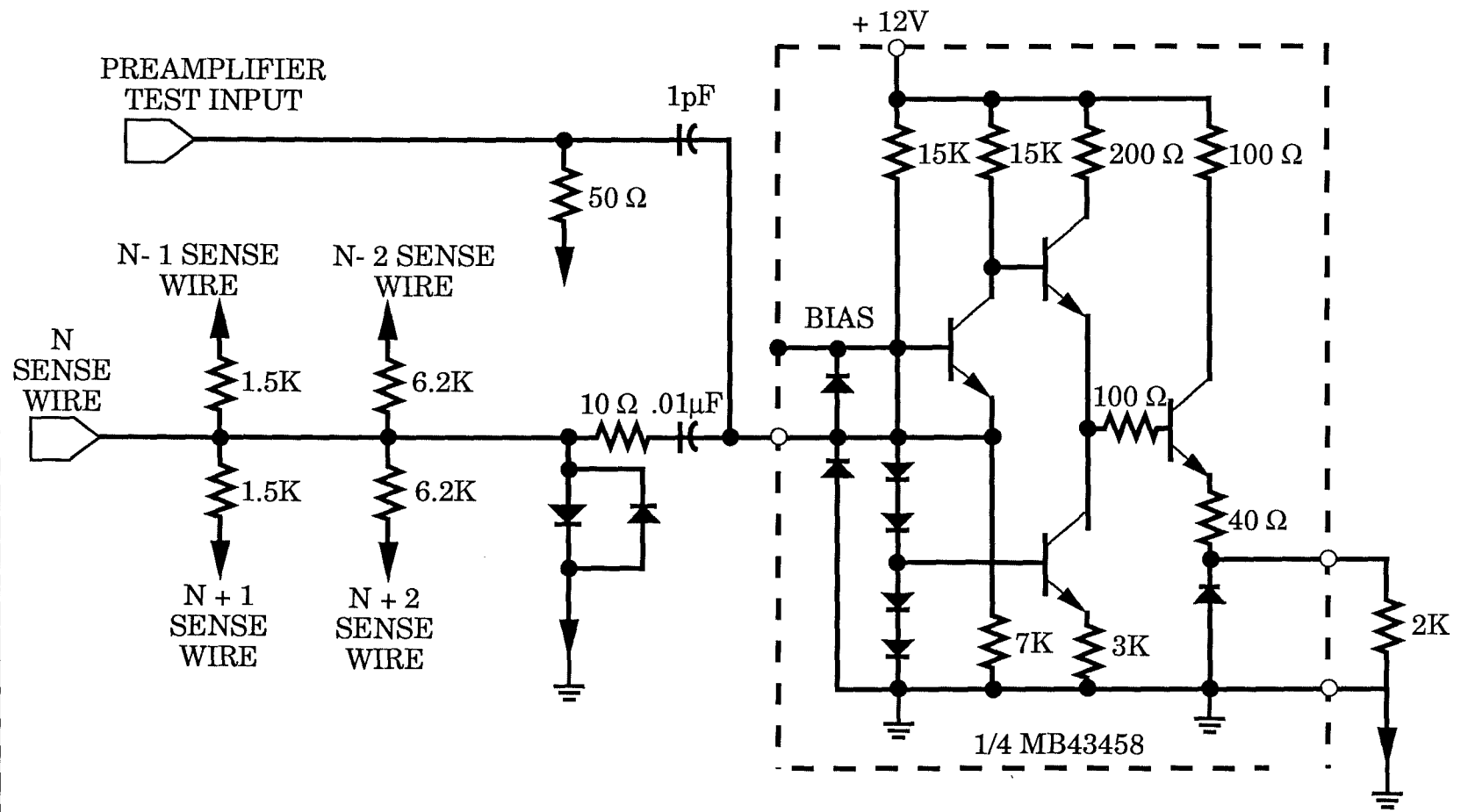
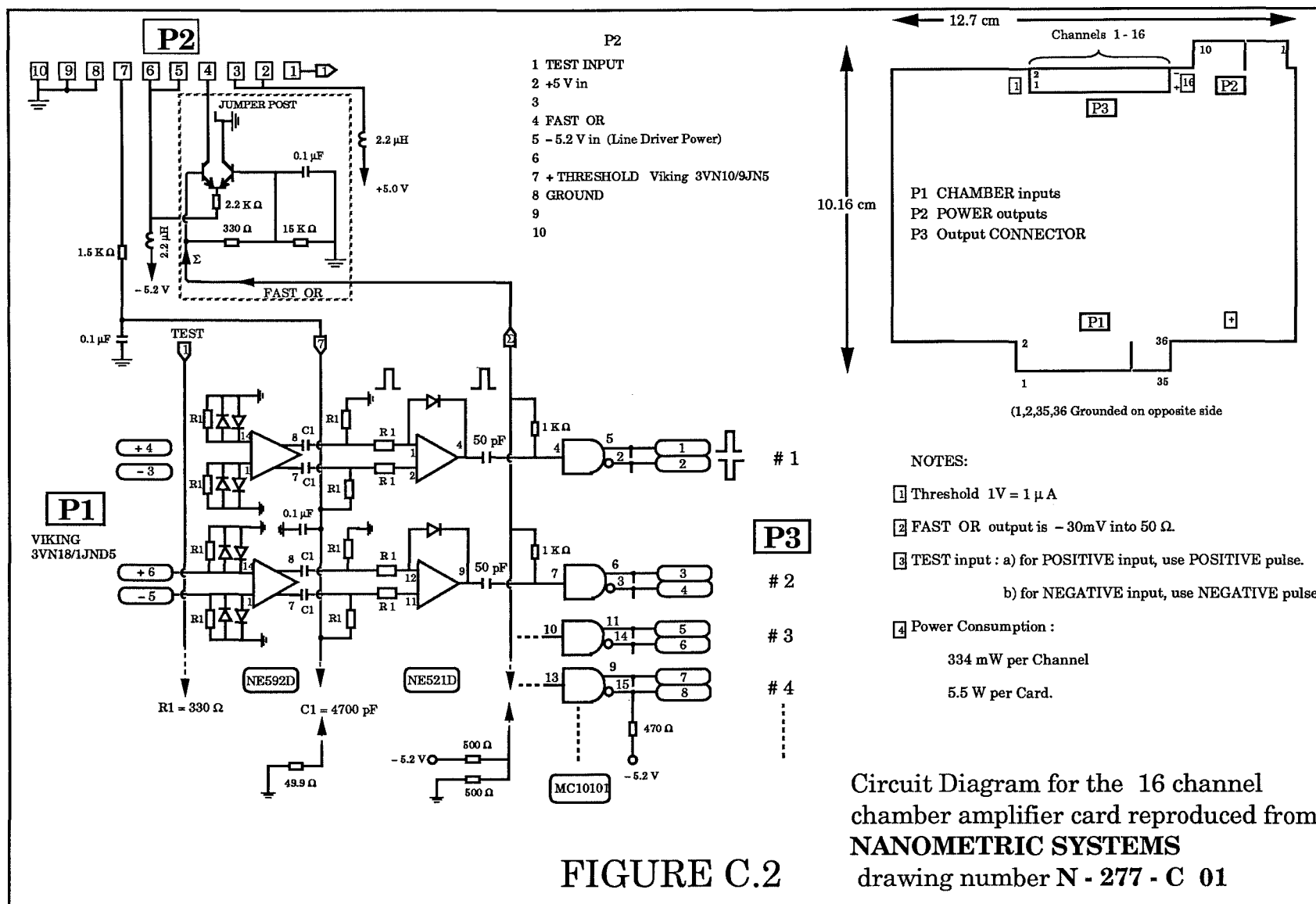
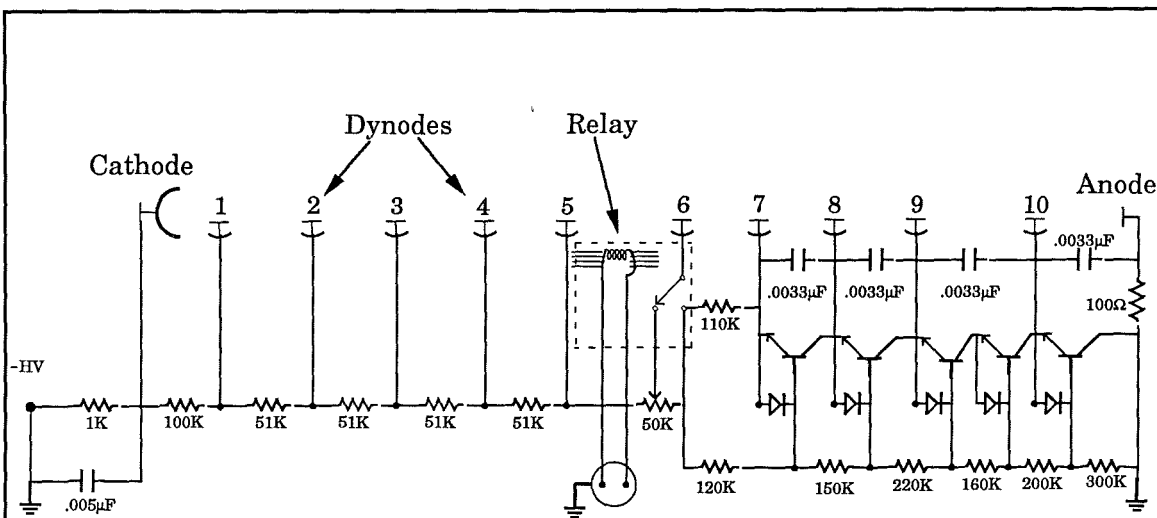


FIGURE C.1

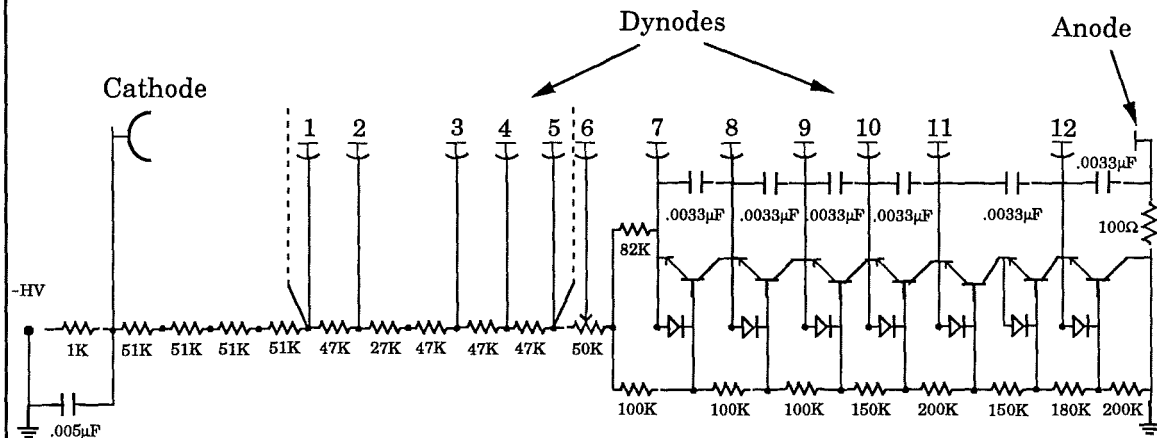
A single channel for the preamplifier circuit and associated testing circuitry.

Ref: 74





(a)



(b)

FIGURE C.3

Schematic of the Phototube Bases. The R2154 base is shown in (a) and the R329 base is shown in (b)  
 Transistors are: MPS-U10; Diodes are: IN914B;  
 Resistors are: 1/2 W 5% carbon composition

## References

- 1 J. J. Thomson, Camb. Lit. and Phil. Soc **XV**, pt. 5 (1910).
- 2 H. Geiger and E. Marsden, Proc. Roy. Soc. (London) **82**, 495 (1909).
- 3 E. Rutherford, Phil. Mag. **21**,669 (1911).
- 4 *Proceeding of the International Conference on Nucleon Structure*  
Stanford University, Stanford (1963).
- 5 A.L.S. Angelis et al., Physica Scripta **19**, 116 (1979)  
D. A. Levinthal, Ph.D. Thesis, Columbia University (1980).
- 6 M. Breidenbach et al., Phys. Rev. Lett. **23**, 935 (1963)  
J. D. Bjorken, Phys. Rev. **179**,1547 (1969).
- 7 R. P. Feynman, Phys. Rev. Lett. **23**, 1415 (1969).
- 8 M. Gell-Mann, Phys. Lett. **8**, 214 (1964).
- 9 G. Zweig, CERN Report **8182/TH**, 401 (1964).
- 10 O.W. Greenburg, Phys. Rev. Lett. **13**, 598 (1964).
- 11 F. W. Busser et al., Phys. Lett. **46B**, 471 (1973).
- 12 S. D. Ellis, *Proceedings of the 7th International Conference on High Energy Physics*, London, England, **V-23** (1974).
- 13 R. Blankenbecler, S. J. Brodsky, and J. F. Guion, Phys. Lett. **39B**, 649 (1972).
- 14 H. J. Frisch et al., Phys. Rev. Lett. **44**, 511 (1980).
- 15 S.L. Glashow, J. Iliopolus, and L. Maiani, Phys. Rev. **D2**,1285 (1970).
- 16 S. Berman, J. D. Bjorken, and J. Kogut, Phys. Rev. **D4**, 3388 (1971).
- 17 R. P. Feynman, R. D. Field, G. C. Fox, Phys. Rev. **D18**, 3320 (1978).

- 18 J. D. Bjorken, Phys. Rev. **179**, 1547 (1969).
- 19 R. P. Feynman, *Photon Hadron Interactions*, Benjamin Press, New York, (1972).
- 20 D. W. Duke and J. F. Owens, Phys. Rev. **D30** , 49 (1984).
- 21 R. Cutler and D. Sivers, Phys. Rev. **D16** , 679 (1977).
- 22 B. L. Combridge, J. Kripfganz, and J. Ranft, Phys. Lett. **70B**, 234 (1977).
- 23 R. Cutler and D. Sivers, Phys. Rev. **D17** , 196 (1977).
- 24 G. Hanson et al., Phys. Rev. Lett. **35** ,1609 (1977).
- 25 J. Ellis, M.K. Gaillard and G. G. Ross, Nucl. Phys. **B111**, 253 (1976).
- 26 R. Brandelik et al. (TASSO Collaboration), Phys. Lett. **86B**,243 (1979).
- 27 D. P. Barber et al. (MARK J Collaboration),Phys. Rev. Lett. **43**, 830 (1979).
- 28 Ch. Berger et al. (PLUTO Collaboration), Phys. Lett. **86b**, 418 (1979).
- 29 W. Bartel et al. (JADE Collaboration), Phys. Lett. **91B**, 142 (1980).
- 30 J. F. Owens, Rev. Mod. Phys. **59**, 465 (1987) .
- 31 E. Leader and E. Predazzi, *An Introduction to Gauge Theories and the New Physics*, Cambridge University Press, Cambridge,(1982).
- 32 R. P. Feynman, R. D. Field, and G. C. Fox, Phys. Rev. **D18**, 3320 (1978).
- 33 J.F. Owens, E. Reya, and M. Glück, Phys. Rev. **D18**, 1501 (1978).
- 34 R. P. Feynman, R. D. Field, G. C. Fox, Phys. Rev. **D18**, 3320 (1978).
- 35 R. D. Field, Phys. Rev. Lett. **40**, 997 (1978).
- 36 R. Baier et al., Zeitschrift für Physik **C 2**, 265 (1979).
- 37 J. F. Owens, Florida State University, (private communication) (1989).
- 38 R. J. Fisk, et al., Phys. Rev. Lett. **40**, 984 (1978).



- 39 H. Jöstlein, et al., Phys. Rev. **D20**, 53 (1979).
- 40 H. Jöstlein, et al., Phys. Rev. Lett. **42** 146 (1979).
- 41 J. A. Crittenden, et al., Phys. Rev. **D34** ,2584 (1986).
- 42 J. A. Crittenden, et al., Phys. Rev. **D34** ,2584 (1986).
- 43 D. A. Levinthal, H. B. White et al., *Expt. Proposal P-711*, Fermilab (1982).
- 44 P. Bagnaia, et al., Phys. Lett. **144B**, 283 (1984).
- 45 G. Arnison et al., **CERN-EP/86-55** (1986b).
- 46 J. F. Owens, *Proceedings of the Twentieth Rencontre De Moriond Vol. 1*, 151 (1985).
- 47 D. W. Duke and J. F. Owens, Phys. Rev. **D30** , 49 (1984).
- 48 D. A. Levinthal, Ph. D. Thesis, Columbia University 1980 [Nevis Lab Report **235** (1980)].
- 49 A.L.S. Angelis et al., Nucl. Phys. **B209** , 284 (1982).
- 50 J. F. Owens, *Proceedings of the Twentieth Rencontre De Moriond Vol. 1*, 151 (1985).
- 51 F. Abe et al., ( the CDF Collaboration) **Fermilab Pub-89/62-E** (1989).
- 52 Current Experiments in Elementary Particle Physics, Univ. of California **LBL-91** Revised ,Fermilab Beams (Source: H. B. White, Jr), 173 (September 1989).
- 53 Originated by G. Koizumi, Research Division Fermilab, 1985.
- 54 K.L. Brown, D.C. Carey, Ch. Iselin, F. Rothacker, *Transport, A computer Program for Designing Charged Particle Beam Transport Systems*, **CERN internal report 80-04**, Geneva (1980).
- 55 A. Ito, et al., ZIPTRACK manual, **Fermilab-TM-1200**, (1983).
- 56 F. Sauli, Principles of operation of multiwire proportional and drift chambers, **CERN Report 77-09**, (1977).
- 57 M. Crisler, The E711 Calorimeter Design Report, E711 Internal Memorandum, (1983).

- 58 K. R. T. Streets, Calorimeter Calibration, E711 Internal Memorandum, April (1987).
- 59 Bevington, *Data Reduction and Error Analysis for the Physical Sciences*, McGraw-Hill Co., (1969).
- 60 K. R. T. Streets, Ph.D. dissertation, Florida State University, (1989).
- 61 Richard C. Fernow, *Introduction to Experimental Particle Physics*, Cambridge University Press, Cambridge, 1989.
- 62 CAMAC system, Atomic Energy Commission report **TID - 25875**, Washington D. C.
- 63 J. F. Bartlett et al., Fermilab Multi User's Guide, **PN-97.5** (1979).
- 64 R. E. West et al., EPICS SYSTEM : System Structure and User Interface, **Fermilab-TM-1243**, (February 1984).
- 65 C. H. Georgiopoulos et al., Nucl. Instr. and Methods **A261**, 493 (1987).
- 66 D. Levinthal et al., Computer Physics Comm. **45**, 137 (1987).
- 67 Jianwei Qiu, FSU (private communication) (1990).
- 68 K. Streets et al., Phys. Rev. Lett. **66**, 864 (1991).
- 69 J. F. Owens, FSU (private communication); further description see Ref (49).
- 70 W.H. Press, B. P. Flannery, S. A. Teukolsky, W. T. Vetterling, *Numerical Recipes The Art of Scientific Computing*, Cambridge University Press (1985).
- 71 F. Mandl and G. Shaw, *Quantum Field Theory*, John Wiley & Sons, New York, (1984) p.139 .
- 72 J. F. Owens, Rev. Mod. Phys., **59**, 465 (1987) .
- 73 T. Toohig, Fermilab Magnets, Power Supplies, and Auxillary Devices: Technical Data, **Fermilab-TM-632**, (1975).
- 74 R. J. Yarema, A New Pre-amplifier for Particle Detectors, **Fermilab-TM-1284**, November, 1984.